Energy Balance in Planetary Thermospheres: A Focus on Earth and Venus

by

Brandon M. Ponder

A dissertation submitted in partial fulfillment
of the requirements for the degree of
Doctor of Philosophy
(Climate and Space Sciences and Engineering)
in the University of Michigan
2023

Doctoral Committee:

Professor Aaron J. Ridley, Chair
Professor Dennis S. Bernstein
Research Professor Stephen W. Bougher
Associate Professor Shasha Zou

Brandon M. Ponder
bponder@umich.edu
ORCID iD: 0000-0002-0451-8021

ACKNOWLEDGMENTS

I want to express my heartfelt gratitude for the guidance and support I received at the University of Michigan. While it's impossible to credit everyone who contributed to my graduate school experience, I want to specifically address three people:

- Mark Moldwin: I consider myself incredibly fortunate to have worked with you as an undergraduate. Back then I lacked direction, but you did a fantastic job of introducing me to the world of space science research. Although we did not get the opportunity to directly collaborate since then, it feels that without your guidance I wouldn't be here today.

- Steve Bougher: I asked many people for compelling reasons to pursue a career in academia. Every response left much to be desired until hearing from you. Your passion is infectious and it *almost* convinced me to pursue a post doc. Your expertise on Mars and Venus have been instrumental in helping me build V-GITM and answering the interesting questions at Venus. It is really hard to imagine our work being as compelling as it is without your help.

- Aaron Ridley: My first encounter with you involved you grilling our undergraduate CanSat team during the PDR. When I received an offer to do a Ph.D. with you as an advisor, that experience made me realize that having you as an advisor would be a rewarding challenge. I anticipated that your expectations would be high and it wouldn't be easy, but I would be better off because of it. You did set high expectations and pushed me to dig deeper to improve my coding skills and understand the fundamental physics. This approach made me a much better scientist. I must also thank you for the amount of development in the terrestrial version of GITM. Looking back, if GITM were in a more infantile state, I can only imagine how much extra work developing V-GITM would have been. Therefore, I want to express my gratitude for all the work that contributed to my starting point. The countless hours you have spent reviewing my work, offering insightful feedback, and patiently answering my questions have not gone unnoticed. Your guidance has defined the quality and success of my work, and I am forever grateful for your mentorship and the challenge it presented.

- Ankit Goel: As a significant contributor and co-author to the RCMR project, I want to thank you for your help. At the time, I was a new Ph.D. student and you helped me to integrate a

relatively complex project into simpler, bite-size pieces. We worked on these until the bigger picture was realized. Thank you for being a critical element in improving GITM.

I also want to extend thanks to Dennis Bernstein, Amanda Brecht, and Dave Pawlowski for taking the time to read and provide feedback on the papers we have collaborated on. Your insights and comments have helped to improve the quality of our work significantly and I truly appreciate the time spent. Once again, thank you for your contributions and for being such fantastic colleagues. Once again, thanks to each of you for everything. I feel privileged to have had the opportunity to work with you and learn from you. I will always be grateful for your support, guidance, and friendship.

TABLE OF CONTENTS

LIST OF FIGURES

FIGURE

LIST OF TABLES

TABLE

LIST OF ACRONYMS

CFL Courant-Friedrichs-Lewy

CHAMP Challenging Minisatellite Payload

DAVINCI Deep Atmosphere Venus Investigation of Noble gases, Chemistry, and Imaging

EDC eddy diffusion coefficient

EKF Extended Kalman Filter

EnKF Ensemble Kalman Filter

FISM Flare Irradiance Spectral Model

GCM General Circulation Model

GITM Global Ionosphere Thermosphere Model

GRACE Gravity Recovery and Climate Experiment

HHSMT Heinrich Hertz Sub-Millimeter Radio Telescope

IR infrared

JCMT James Clark Maxwell Telescope

JWST James Webb Space Telescope

LEO Low Earth Orbit

LT local time

LMD Laboratoire de Météorologie Dynamique

OETP Orbiter Electron Temperature Probe

OIMS Orbiter Ion Mass Spectrometer

ONMS Orbiter Neutral Mass Spectrometer

PVO Pioneer Venus Orbiter

RCMR Retrospective Cost Model Refinement

RSZ Retrograde Superrotating Zonal

SOIR Solar Occultation IR

SPICAV Spectroscopy for the Investigation of the Characteristics of the Atmosphere of Venus

TESS Transiting Exoplanet Survey Satellite

UV Ultraviolet

VeRa Venus Express Radio Science

VERITAS Venus Emissivity, Radio Science, InSAR, Topography, and Spectroscopy

V-GITM Venus Global Ionosphere Thermosphere Model

VIRA Venus International Reference Atmosphere

VIRTIS-H Visible and InfraRed Thermal Imaging Spectrometer, high resolution channel

ABSTRACT

The goal of this dissertation is to help understand how the energy balance at Venus, Earth and Mars create the different planetary atmospheres that are observed today. This is started by using an existing ionosphere-thermosphere model developed for Earth, the Global Ionosphere Thermosphere Model (GITM) and branching this model off to create a version for Venus. Throughout the use of GITM and development of the Venus Global Ionosphere Thermosphere Model (V-GITM), there has been an improved understanding of the physics that go into each atmosphere.

At the beginning of this thesis, it is understood that physics-based models attempt to predict densities at Earth to assist in orbit propagation. These models have a great deal of uncertainty, including model biases and model misrepresentation of the atmospheric response to energy input. These may stem from inaccurate approximations of terms in the Navier-Stokes equations, unmodeled physics, incorrect boundary conditions, or incorrect parameterizations. This work shows the effectiveness of using the retrospective cost model refinement (RCMR) technique at removing model bias caused by various sources within GITM. Numerical experiments, Challenging Minisatellite Payload (CHAMP) and Gravity Recovery and Climate Experiment (GRACE) data during real events are used to show that RCMR can compensate for model bias caused by both inaccurate parameterizations and drivers. RCMR is used to show that eliminating model bias before a storm allows for more accurate predictions throughout the storm.

Secondly, Venus Global Ionosphere Thermosphere Model (V-GITM) is introduced which incorporates the terrestrial GITM framework with Venus-specific parameters, ion-neutral chemistry, and radiative processes in order to simulate some of the observable features regarding the temperatures, composition, and dynamical structure of the Venus atmosphere from 70 km to 170 km. Atmospheric processes are included based upon formulations used in previous Venus GCMs, several augmentations exist, such as improved horizontal and vertical momentum equations and tracking exothermic chemistry. Explicitly solving the momentum equations allows for the exploration of its dynamical effects on the day-night structure. In addition, V-GITM's use of exothermic chemistry instead of a strong heating efficiency accounts for the heating due to the solar EUV while producing comparable temperatures to empirical models. V-GITM neutral temperatures and neutral-ion densities are compared to upper atmosphere measurements obtained from Pioneer Venus and Venus Express. V-GITM demonstrates asymmetric horizontal wind velocities through the cloud tops to

the middle thermosphere and explains the mechanisms for sustaining the wind structure. In addition, V-GITM produces reasonable dayside ion densities and shows that the neutral winds can carry the ions to the nightside via an experiment advecting O_2^+.

However, the results produced by V-GITM contained uncertainties stemming from the treatment of the internal physics and parameterizations. Recognizing that the model drivers have imperfections gives an opportunity to vary these terms and evaluate the response. In this study, the Venus Global Ionosphere–Thermosphere Model (V-GITM) modifies the implementations of the solar EUV, solar near IR, eddy diffusion, radiative cooling in the lower thermosphere, and thermal conduction to determine the impact on globally averaged temperatures. It is found that among these, uncertainty in the eddy diffusion coefficient and solar EUV most strongly translate to uncertainty in the temperature and density results. In addition, variations in the eddy diffusion coefficient are shown to result in significant uncertainty in the thermospheric composition and height of Venus' transition zone.

Overall, this thesis has highlighted some of the outstanding questions in Earth and Venus thermospheres and have answered them through exhaustive comparisons of GITM simulations with different remote observations and empirical models, while laying out a framework for the newly developed V-GITM model.

CHAPTER 1

Introduction

Earth's neighbors have garnered large amounts of interest for space and climate scientists for nearly 60 years. In the early 1960s, Mariner 2 performed a flyby around Venus and Venera 7 was the first satellite to land on any other planet. The early attention towards Venus was diverted once it was hypothesized that Mars had surface water. Since then, the vast majority of planetary satellite missions have been dedicated to Venus and Mars research. Aside from the close proximity, there are solid foundations for why Venus and Mars are so interesting to scientists.

Venus, Earth and Mars are all planets that fit inside of or very near the habitable zone of our very average-sized, class G star. While Earth is a habitable planet, the parameters that make it habitable are still largely uncertain to scientists. One factor to consider is the distance from the host star. The star-to-planet distance controls just how much irradiance, or radiant energy, the planet receives from the host star. This incoming energy is arguably one of the most important factors in determining a planet's surface temperature, pressure and ability to sustain water. The problem is not as simple as postulating that the Earth-Sun distance as the habitable zone though, because not all stars are created equal. As seen in Figure 1.1, stars vary in temperature and size, therefore increasing the complexity of gauging how far from a star is the right distance. In many instances, solar systems will have two stars, making this even more convoluted.

Larger and warmer stars than the Sun emit more radiation which drives warmer planetary temperatures. In order to compensate for this, Earth-like planets need to orbit its star further away than 1 AU (the current Earth-Sun distance) in order to receive the same amount of radiation. The inverse is true for smaller or colder stars. Figure 1.1 shows that Venus receives nearly double the radiation as Earth putting it outside the habitable zone. For a colder star, Venus could be a better candidate for habitability than Earth.

The most buzzworthy factor for planet habitability is water. Aside from human dependence, water is a great indicator of habitable conditions. In order to sustain liquid water, the planet must have the correct temperature, a substantial atmosphere and minimal atmospheric loss. The latter is a process that is believed to have driven climate change on Mars (Jakosky et al., 2018). At the

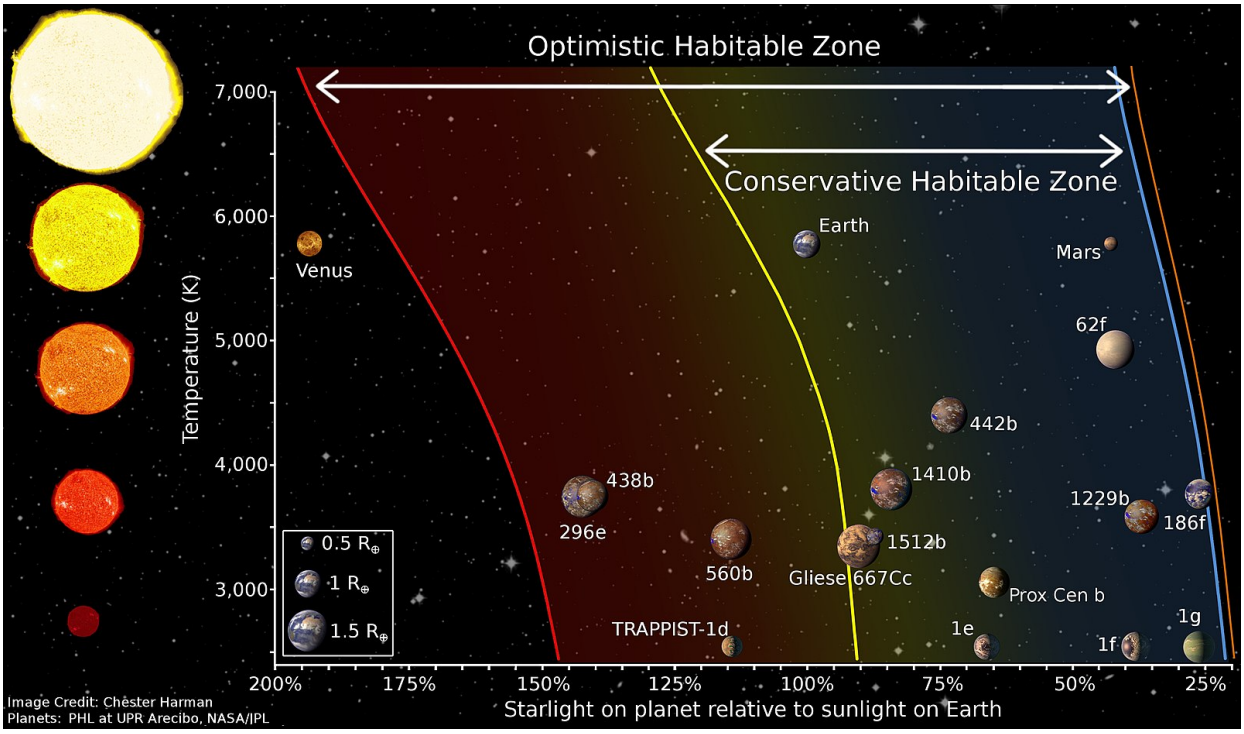

Figure 1.1: Illustrated habitable zones for varying star temperatures, planet size and relative radiation on planet compared to Earth. Adopted from (Harman, 2017).

edge of space, light chemical species like atomic hydrogen and oxygen are susceptible to being lost to space. These light particles gather at the border of a planet's atmosphere because of a process known as molecular diffusion. This process is very similar to the separation of oil and water in a glass. When left undisturbed, the water and oil separate with the heavier fluid on the bottom. The edge of space is similar to the undisturbed glass where the lower atmosphere is more like a constantly stirred mixture. In cases where the thermal energy of hydrogen, oxygen or other light elements has enough vertical velocity, they can overcome a planet's gravitational pull, which would ordinarily keep the particle tied to the atmosphere. Non-thermal escape of oxygen and Jeans escape of hydrogen are known to dominate at Mars during the present epoch (Lillis et al., 2015). Being constituents of H_2O, hydrogen and oxygen loss is a critical metric for evaluating a planet's ability to sustain water. It's already estimated that Earth will lose its surface water in roughly one billion years (the Earth is already roughly 4.5 billion years old) (Kasting, 1988) (Guinan and Ribas, 2002).

1.1 Rocky Planets

1.1.1 Mercury

Mercury is the closest planet to the Sun and has nearly no planetary atmosphere. Mercury has a radius of around 2440 km (1516 mi) with a mass that's 1/20th that of Earth. Newton's Law of Universal Gravitation explains that mass is one of the defining features of the strength of a planet's gravitation pull, which helps keep atmosphere bound to the planet. Consequently, Mercury's low surface gravity is the primary reason Mercury cannot maintain an atmosphere. Being so close to the Sun also lends itself to being a very hot planet with dayside temperatures at 700 Kelvin (800°F). Although Mercury is very hot on the sun-facing side of the planet, without an atmosphere it is difficult to prevent heat from escaping to space and consequently has cold night temperatures of 93 K (-290°F).

A liquid, electrically charged, and rotating core generates a dipole magnetic field for Mercury. The magnetic field strength is $\sim 1\%$ of Earth's magnetic field (Philpott et al., 2014). Similar to Earth, the magnetic field has an interaction with a supersonic solar wind. The balance of the magnetic pressure and solar wind dynamic pressure match near 1000-2000 km above the surface of Mercury, creating a magnetosphere (Slavin et al., 2007).

1.1.2 Venus

The second planet in the solar system, Venus, is actually the hottest with surface temperatures up to 755 K (900°F). Venus is often called Earth's twin because these planets are neighbors, the radius of the planets are within $\pm 5\%$, the masses are within $\pm 20\%$, and the surface gravity is 8.87 m/s^2 (Earth's is 9.81 m/s^2).

Twin is a very simple term because there are significant differences that contribute to outcomes in habitability. In regards to the orbital properties, Venus rotates around the Sun between 224-225 Earth days. This is noticeably different than the 365 days we experience on Earth, but more irregular is the experience of a Venus "day". Venus rotates very slowly and nearly upright with only 2.6° of obliquity. The rotation is in a clock-wise direction (Earth rotates counter-clockwise) around its axis once every 243 Earth days (compared Earth's 24 hours). Due to the slow rotation around its axis and around the Sun, Venus experiences two day/night cycles during one trip around the Sun. Unlike Earth, Venus does not have a moon orbiting around the planet nor does it have a magnetic field. Venus does maintain a thick atmosphere primarily composed of CO_2 and has a surface pressure nearly 90 times larger than Earth's surface pressure. CO_2 is an excellent greenhouse gas and is the reason Venus is the hottest planet in our solar system.

1.1.3 Mars

Mars is a cold planet with maximum surface temperatures around 293 K (68°F). It has a weak magnetic field sparsely scattered around the planet that extends just above the crust. Mars has a more recognizable rotation around its axis once every 24.6 hours. Being further from the Sun, Mars has a much longer yearly cycle of 687 Earth days.

Similar to Venus, Mars is primarily composed of CO_2. It's surface pressure is very small at roughly 0.5% that of Earth and 0.007% of Venus. This is because Mars' surface gravity is only 37% of Earth's which has lead to large amounts of its atmosphere escaping to space. Despite the atmosphere being so thin, Mars sustains water in the form of ice near the poles. Liquid water was believed to be in rivers and streams on Mars billions of years ago leading to speculation that Mars was warmer and had a more sizeable atmosphere to prevent evaporation of water.

Unlike the other rocky planets, Mars experiences dust storms capable of covering the entire planet every few years (Pang and Hord, 1973). A dust storm occurs when very fine dust particles are swept into the air by moderately fast winds. The smaller gravity and pressure on Mars allow the dust to be transported higher into the atmosphere and over longer distances before settling in a new location (Clancy et al., 2010). The dust is capable of reflecting solar radiation, which has implications for the local heating that occurs in areas with high densities of dust. This is important because the local heating effects dictate the local temperature, wind speeds, and onset of new dust storms.

1.1.4 Exoplanets

An exoplanet is any body outside of our solar system that has a few characteristics. It must (a) orbit a star; (b) have a strong enough gravitational pull to make it's shape relatively spherical; and (c) have a large enough gravitational pull that it has cleared away any other objects of a similar size near its orbit around the star. Exoplanets are important because they offer us the possibility of discovering extraterrestrial life, provide insight into planetary formation and evolution, and expand our knowledge of the Universe.

Currently, there is so much unknown about exoplanets simply due to the fact that they are so far away and that makes obtaining direct measurements impossible. For this reason, every advancement in our understanding of exoplanets is a big step forward. Major space organizations (NASA, ESA, and CSA) recognized this and funded the James Webb Space Telescope (JWST). It was launched to expand our understanding of the universe and to answer some of the most fundamental questions in astronomy and astrobiology. It was designed to be the successor to the Hubble Space Telescope and is set to be one of the most powerful space telescopes ever built. One of the key objectives of the JWST is to observe the formation of stars and planetary systems,

including the study of exoplanets and the potential for life beyond our solar system.

The Transiting Exoplanet Survey Satellite (TESS) instrument aboard JWST is able to observe transiting exoplanets. Transits occur when a body crosses through the radiation emitted from the stellar body causing a dip in the measured luminosity. Larger volume exoplanets and exoplanets that orbit closer to their star will be easiest to observe using this method. If observing transiting planets in the Milky Way, this would correspond to the inner rocky planets and Jupiter, which is a good start since this would include the one habitable planet, Earth and two very highly studied planets Venus and Mars. Earth, Venus and Mars are near or inside of the habitable zone but have some obvious, and also unexpected differences. These planets are useful to study to improve our understanding of exoplanets. Defining what atmospheric parameters determine habitability and understanding the physics that drive different atmospheric properties help us determine the habitability of exoplanets. As such, prototypes for exoplanet studies that are popular today focus on Venus, Mars and Earth. In the next section, some of the layers of the atmosphere are discussed and how they may differ from planet to planet.

1.2 Layers of the Atmosphere

Planetary atmospheres are typically partitioned into layers with differing temperature gradients. Nearest to a planet's surface is the troposphere. In this region, it is where the bulk of the atmosphere's mass is located. This is due to the impact of gravity. Atmospheric weather, like a hurricane on Earth or a dust storm on Mars, typically occurs in the troposphere. In Venus' troposphere, there is a unique wind pattern that circulates around the planet. A few kilometers above the planet's surface, the winds are faster than the planet's rotation speed around its axis. The temperature decreases with altitude up to the point where other heating processes take over, indicated by the temperature remaining relatively constant or increasing with altitude.

Above the troposphere, temperatures behave differently than before. At Earth, temperatures begin to increase with altitude and is the signature of the stratosphere. Earth's stratosphere is where the ozone layer (O_3) exists. Ozone is known for protecting humans by significantly reducing the amount of the Sun's Ultraviolet (UV) light that reaches the planet's surface. Ozone absorbs the Sun's UV radiation, heating the atmosphere layer driving an increase in temperature with altitude in Earth's stratosphere. On Venus, there is no equivalent of an ozone layer to heat the atmosphere, which explains the difference in the temperature structure shown in Figure 1.2 between 10^2 and 10^0 millibars.

Above the stratosphere, temperatures start to cool again with increasing altitudes up to a local minimum due to a lack of absorption of solar radiation. This region is known as the mesosphere and has 1000 times less air pressure than the sea level at Earth. Earth's mesosphere is difficult to

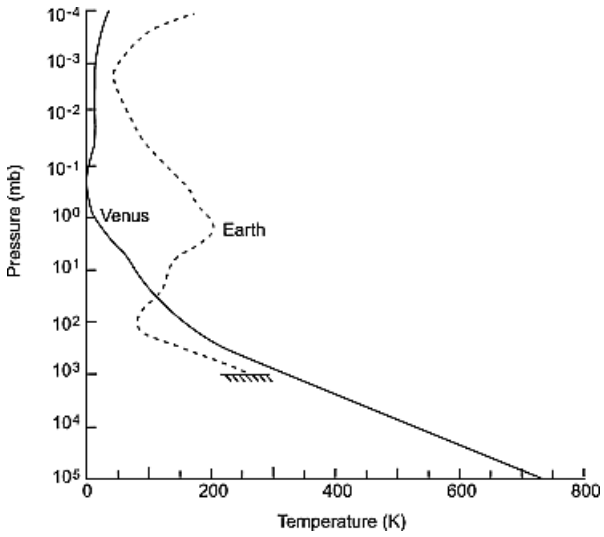

Figure 1.2: Measured temperature profiles of Earth and Venus. From Taylor and Grinspoon (2009).

study because the air pressure is low enough that aircraft cannot fly in this region, but has a large enough atmosphere that the drag effects on satellites are too large making it impossible to maintain an orbit. On the other hand, Venus' mesosphere has air pressures comparable to that of habitable regions on Earth. This could be useful for a self-powered aircraft to sustain flight for scientific measurements or a floating colony like a dirigible.

The thermosphere is further above where temperatures increase with altitude up to where the atmosphere becomes isothermal. Similar to the stratosphere, the main heating source in this region is radiation from the Sun in extreme UV. In the Earth's thermosphere, the atmosphere is thin enough that the drag effects become manageable to sustain orbital flight. Temperatures in the thermosphere vary greatly from Venus to Earth. Earth's thermosphere is very hot ($\sim$1000 K) compared to its surface temperature ($\sim$273 K). Despite being closer to the Sun and receiving much larger amounts of solar radiation, Venus' thermosphere maximum temperature (see Table 1.1) is quite cold in comparison to (1) Earth's surface temperature and (2) Venus' surface temperature. This is due to the differing heating and cooling mechanisms at each planet.

	Venus	**Earth**
Sun-Planet Distance (AU)	0.72	1.0
Surface Temperature (K)	740	273
Thermosphere Temperature (K)	300	1000
Surface Gravity (m/s^2)	8.87	9.81

Table 1.1: A comparison of some commonly asked planet-specific quantities. Max thermosphere temperatures are approximations.

Overlapping in the thermosphere is the ionosphere, where charged particles (ionized plasma) are created and sustained. The ionosphere and thermosphere typically are in the same region because both regions are created from the incoming solar EUV. Ions are primarily created when the energy of a photon is larger than the ionization threshold of a neutral particle or molecule and an electron is freed. For many of the chemical species found in our solar system's planets, this ionization threshold happens in or around the EUV part of the solar spectrum. Further above the thermosphere/ionosphere may exist a magnetosphere.

A continuous stream of charged particles, primarily composed of protons and electrons, are ejected from the upper atmosphere of the Sun to fill the interplanetary medium. This phenomena is referred to as the solar wind. The solar wind originates from the Sun's outermost layer, called the corona, which is an extremely hot and ionized region of plasma. Due to the high temperature and intense magnetic activity within the corona, particles gain enough energy to escape the Sun's gravitational pull and are propelled outward into space. The solar wind carries a variety of properties, including its speed, density and magnetic field strength. Typical speeds of the solar wind vary from around 300-800 km/s, but can be even higher during periods of increased solar activity.

The solar wind plays a crucial role in shaping and influencing the space environment in a planetary system and a around the parent star. When the stellar wind encounters a planet with a magnetic field, it interacts with it, causing a complex morphology of the solar wind's and planet's magnetic fields. This stand-off boundary is commonly referred to as the magnetopause and is the upper boundary of the magnetosphere. The interaction between the Sun (or any other stellar body) and a planet's magnetic field are the driver behind space weather. The solar wind and consequent effects are responsible for aurora, but also affect satellites, spacecraft and power grids on Earth, particularly during intense solar storms. Studying the solar wind and its behavior is essential for understanding the Sun's behavior, predicting space weather and ensuring the safety of technological systems that rely on space-based assets.

Venus does not have an intrinsic magnetic field and therefore not a traditional magnetosphere, but rather has an induced magnetosphere. An induced magnetosphere describes planetary region of space protected from the solar wind due to deflection of the solar wind because of the planet's ionospheric currents as illustrated in Figure 1.3. Instead of the intrinsic magnetic field causing the deflection of the magnetic field in the solar wind which usually extends at altitudes above an ionosphere, the induced magnetosphere is a lower altitudes because the magnetosphere extends up to the ionosphere (Spreiter et al., 1970). For reference, the Earth's magnetosphere extends up to roughly 10 Earth radii, Venus' induced magnetosphere extends up to 500 km, and Mars' magnetosphere goes up to 155-170 km (Arridge, 2020).

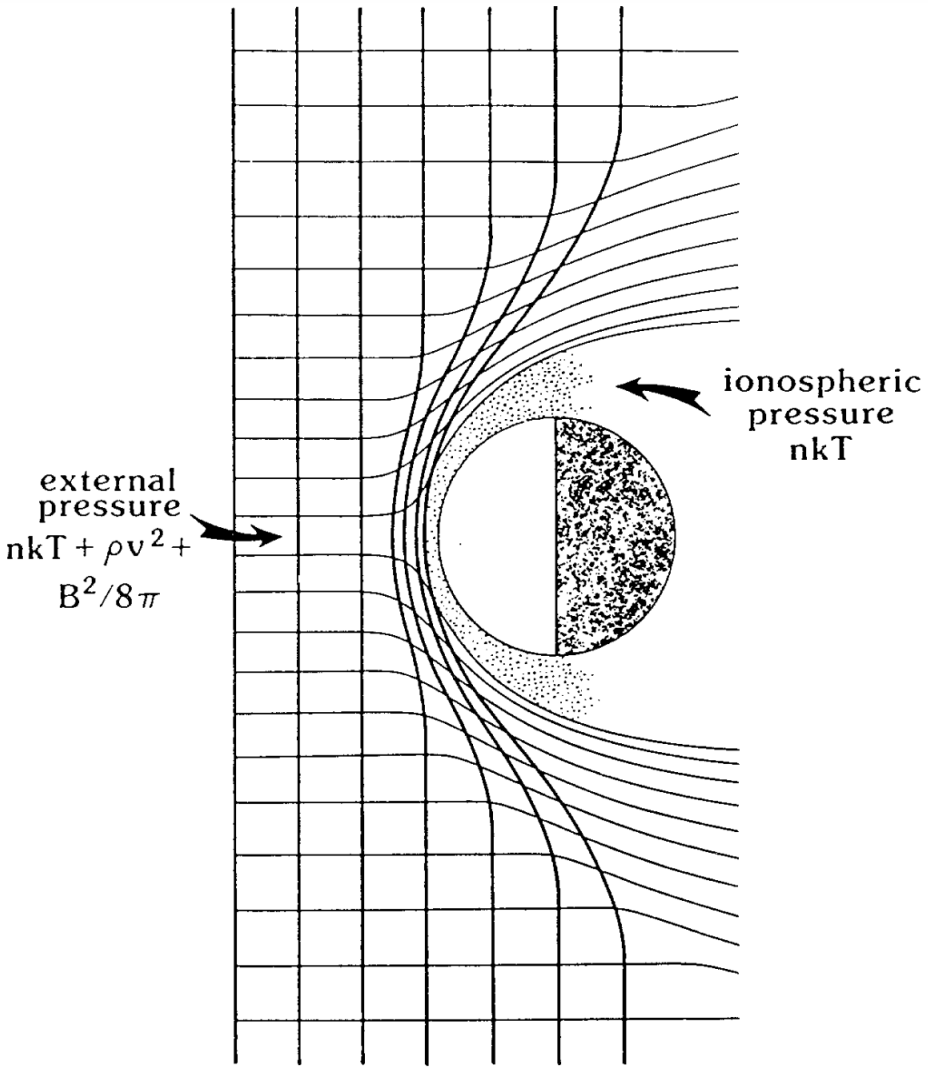

Figure 1.3: Illustration of the solar wind interaction at Venus. The thermal pressure (nkT) of the ionosphere stands off the magnetic ($B^2/8\pi$), thermal and dynamic pressure (ρv^2) of the solar wind. Figure reprinted from Luhmann (1986).

1.3 Heating and Cooling Mechanisms

Thermospheres are typically named to reflect a hot region of the upper atmosphere. At Earth, this is true because the thermosphere is a very hot compared to the ground temperatures or to the layers below. At Venus or Mars, the naming is a misnomer because the thermospheres are cold. This variance in thermosphere temperatures is due to the different physics going on at each planet. Similar to thinking of the different ways the room you're in can be heated; the Sun shining through a window, turning on the oven, running a fan, each of these control the temperature in the room

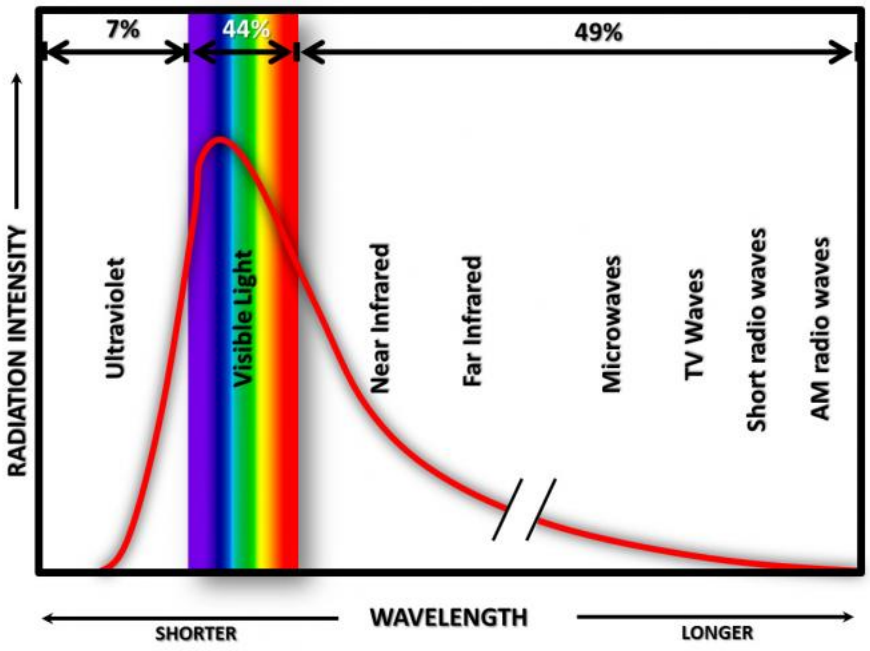

Figure 1.4: A simplified diagram of the different parts of the electromagnetic spectrum with relationship to relative intensity (Lambert and Edwards, 2019).

and so it varies spatially (near a vent/window) and temporally (day/night). The atmosphere works analogously.

The Sun is a primary heat source of thermospheres, particularly for the inner planets of the Solar System. The hot temperature of the Sun radiates energy through photons at wavelengths across the electromagnetic spectrum. Figure 1.4 shows an example curve of emitted radiation from an idealized body similar to the Sun helping identify the different categories of radiation. Due to the temperature of the Sun, Wein's displacement law shows us that primarily visible light is emitted. Earth's atmospheric layers do not absorb this radiation very well, so visible light makes it to the surface, giving us the colors we are able to see as humans.

At longer wavelengths, the solar infrared (IR) can be absorbed by CO_2 atmospheres particularly well at 2.7 μm and 4.3 μm. The efficiency of IR absorption depends on the CO_2 density, solar inclination, and intensity of the incoming radiation. When an IR photon comes into contact with the CO_2 molecule, it gets absorbed and some of it goes directly to local kinetic energy. The fraction of this kinetic energy that is thermalized as heat is considered "solar heating". The incoming radiation is also responsible for putting the molecule in an unstable, excited state. Excited CO_2 particles may collisionally de-excite, typically in lower parts of the atmosphere where densities are larger. The process of de-exciting causes some of the excess energy to be re-radiated back to space at 15 μm to which the upper atmosphere (thermosphere) is transparent. Throughout this

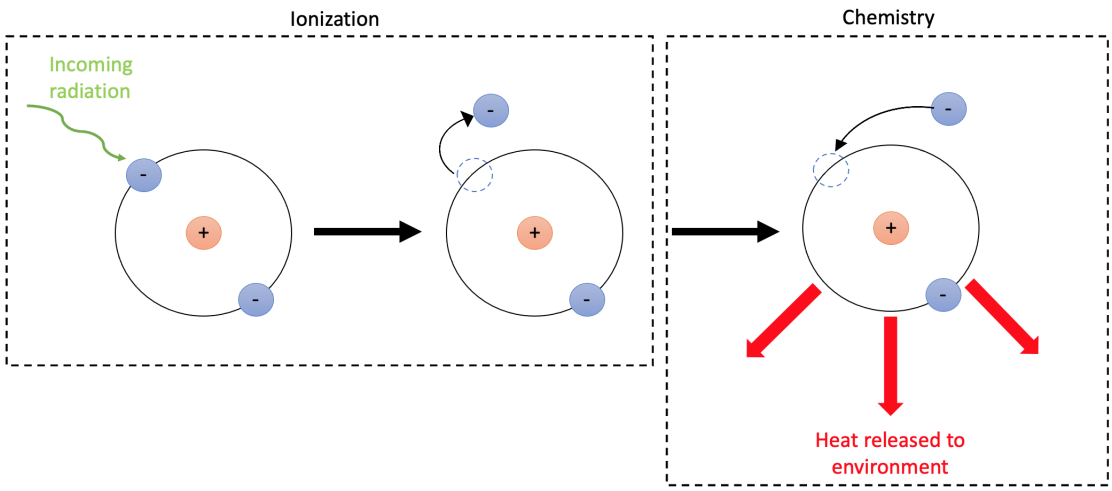

Figure 1.5: An illustration of how incoming radiation heats the atmosphere. On the left, incoming radiation ionizes a neutral particle creating a free ion and electron. A pair of charged particles undergo a chemical reaction that heat the surrounding environment.

thesis, energy that is absorbed is referred to as near IR heating and the cooling to space at 15 μm is referred to as CO_2 cooling.

EUV was briefly discussed in section 1.2 mentioning that it is a primary driver of ionization and also directly absorbed as heat in the atmosphere. A fraction of the total incident energy gets absorbed as thermal energy. EUV radiation has a large enough energy to ionize many different neutral particles. When ions chemically react to become neutral (through charge-exchange, electron recombination, etc...), these reactions are often exothermic. This means that the chemical reactions produce heat for the surrounding atmosphere. This process is illustrated in Figure 1.5.

As EUV and near IR heat different regions of an atmosphere at one time, this creates temperature differences or gradients. Thermal conduction acts to move energy from higher temperature regions to cooler temperature regions. Figure 1.6 shows a simple example of heat transport via thermal conduction. In an atmosphere, this works when different temperature particles collide from their random motion. The warmer particle cools slightly and the cooler particle warms accordingly.

As demonstrated, each of these heating and cooling mechanisms drive temperature changes in spatial locations that do not act uniformly. The summation of these individual forcings create the thermosphere system and so attempting to model each of these terms computationally gives us an opportunity to obtain a broader set of data for planetary atmospheres. Furthermore, many of these terms are fundamental parameters common to each planet despite the vast difference in their atmospheres. Getting a better understanding of each term's role in the atmosphere's thermodynamics allows improvement in our ability to model an exoplanets upper atmosphere, since Venus or

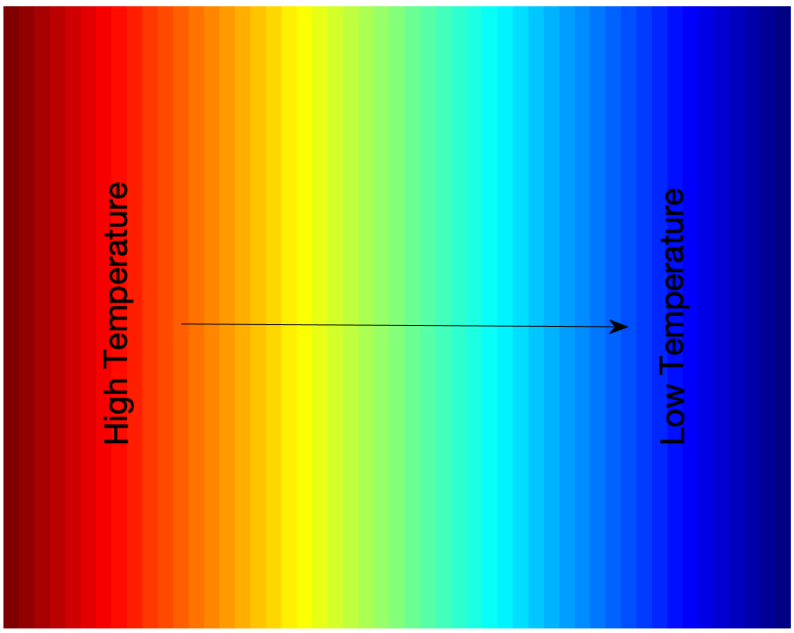

Figure 1.6: Example of energy flow due to thermal conduction.

Mars are considered as good prototypes for exoplanets. A more quantitative description of how the heating and cooling mechanisms are implemented in a modeling framework is explain in Chapter 2.

1.4 Relevance to Satellite Missions

Satellites are an essential part of modern life, providing critical services and enabling us to explore and understand the world around us in new and exciting ways. Satellites are important for a wide range of reasons, including communication, navigation, scientific research, weather forecasting, national security, and more.

Global communication via satellites enables people and organizations to connect across large distances. They are used for everything from telephone and internet service to television broadcasting, and they make it possible for people to communicate and share information across borders and around the world. Satellites are essential for accurate navigation, whether it's for shipping, aviation, or personal travel. GPS is a network of satellites that enables precise navigation and location tracking, and it has become an integral part of daily life for many people.

Satellites are used to conduct scientific research in a variety of fields, including Earth observa-

tion, astronomy, and atmospheric science. They provide a bird's-eye view of the planet, allowing scientists to study changes in weather patterns, track natural disasters, monitor the health of ecosystems, and more. Furthermore, they are used for weather forecasting. Aside from the decision to take an umbrella or wear a jacket, weather forecasting also includes space weather. This is the estimation of events such as solar flares, solar storms and coronal mass ejections. The impact of space weather is not likely to affect people's day-to-day life, but should still be watched over carefully. Council (2008) estimated that the impact of a severe solar storm could have an economic impact of more than $2 trillion which is 20x larger than one of the most recent natural disaster's, Hurricane Ian, impact on the U.S. and Cuba in 2022.

Understanding the environment that satellites fly through is also important for maximizing their lifetime and avoiding collisions. Satellite designers want to minimize mass to keep the costs of the satellite low. The amount of fuel is an important factor to consider because fuel of a satellite is useful for attitude control, preventing premature de-orbiting, and performing collision avoidance maneuvers.

From the standpoint of the spacecraft, the satellite is on the edge of space where the density is very thin, albeit significant enough to be appreciably slowed by the force of drag. The acceleration ($\underline{a}$) due to drag is given by:

$$\underline{a} = -\frac{1}{2}\frac{A}{m}c_D\rho\underline{v}^2\hat{v} \tag{1.1}$$

and is proportional to the ratio of surface area (A) to mass (m) of the spacecraft, coefficient of drag (c_D), and area (A) to mass (m) ratio, but is also directly proportional to the atmospheric density (ρ) and the velocity, relative to the spacecraft, squared (v).

The accuracy of the acceleration due to drag is a function of the accuracy for each of these parameters. While the mass, area, coefficient of drag are all quantities that can be measured before launched, the atmospheric density is highly variable at Earth and is often derived from previous satellite measurements. These observations of the atmosphere are the basis for validating models that predict future densities. Measured densities vary between the dayside, nightside, time of year and solar conditions. Estimating the thermospheric density is a difficult task, because there are no current methods to accurately measure the 3D thermosphere at all times. To overcome this, general circulation models are often used to simulate the physics and solve for the density. Uncertainties in the model physics, drivers and parameterizations have shown that the drag estimations can be inaccurate by up to 20% (Kuang et al., 2014; Marcos, 1990; Bruinsma et al., 2004). Geomagnetic storms typically make the errors in the prediction even worse largely due to poor density estimation (Pachura and Hejduk, 2016). These errors contribute to being the largest source of uncertainty in accurately forecasting orbit trajectories and the probability of a collision, P_c (Thayer et al., 2021; Storz et al., 2005; Hejduk and Snow, 2018).

Due to the issue of inaccurate density prediction (along with any other unmentioned errors), spacecraft and large debris in Low Earth Orbit (LEO) are monitored closely. The length of time ahead that orbit propagators can estimate a spacecraft's position depends on various factors, including the accuracy of the data available, the complexity of the orbit, and the computational resources available for performing the estimation. Generally, orbit propagators try to estimate a spacecraft's position as far ahead as possible while maintaining a high level of accuracy. For most spacecraft in Earth orbit, this is typically a few days to a few weeks into the future. The issue with predicting satellite positions on longer time-frames is that the atmosphere is capable of dramatically changing over the course of a few hours given an unexpected change in geomagnetic conditions and dramatically impacting the calculation behind the probability of a collision (Bussy-Virat et al., 2018). Nonetheless, the calculated orbits of all tracked objects are compared to determine if P_c exceeds 0.0001 (Morselli et al., 2012; Hejduk and Frigm, 2015). In the event of $P_c > 0.0001$, the monitoring organization will signal the affected spacecraft operators to perform an evasive maneuver costing fuel and risking utility of the spacecraft services. In order to protect satellites, identifying and correcting the source of errors in model-generated atmosphere densities should be a topic we prioritize.

1.5 Current State of Available Data

Measurements and numerical models are used to answer questions about the evolution, habitability, and the underlying physics of planetary atmospheres. Direct measurements are probably the most reliable sources of data to attempt to improve our understanding of these atmospheres, but obtaining this data is a difficult task. In addition, the data itself is limited.

In the first project, Challenging Minisatellite Payload (CHAMP) measurements via accelerometer data are used. CHAMP is a satellite orbiting Earth that was managed by GeoForschungsZentrum (GFZ) in July 2000 to gather information about Earth's gravitational and magnetic fields and perform ionosphere sounding. The STAR accelerometer onboard was useful in deriving background mass densities throughout it's orbit. Similar to the CHAMP mission, the mass densities measured from Gravity Recovery and Climate Experiment (GRACE) are of interest for the first project. GRACE was launched as a set of two satellites in March 2002 and ended it's science mission October 2017. The two satellites measured Earth's gravitational field to attempt to map the Earth's surface beyond the assumption of a constant "sea level" sphere.

The data from CHAMP and GRACE are a very small fraction of the measurements we've collected about Earth's atmosphere. Despite all the extra data, the common trend with relying on satellite observations is the constraint of a satellite's orbit lifetime and the limitation of the satellite being in one location at a particular time. This prevents obtaining a three dimensional picture at

any given time and the time-changing effects.

Despite there being many efforts to observe the Venusian atmosphere, data is scarce because the planet is difficult to access. Limaye et al. (2017)'s work put together many ground-based and satellite instrument measurements. The data from these instruments are shown in later sections to validate model results.

- Spectroscopy for the Investigation of the Characteristics of the Atmosphere of Venus (SPICAV) uses a UV spectrometer and two IR spectrometers onboard Venus Express (Bertaux et al., 2007). The UV instrument provides density and temperature profiles from approximately 60 km to 160 km. The VIS-IR instrument is one of two infrared sensors, but this is used in the $0.7-1.7\mu m$ wavelength range to gather H_2O, CO_2 and aerosol information along with $O_2(1-\Delta)$ nightglow. SOIR (solar occultation IR) is part of the SPICAV suite of spectrometers, but measures CO_2 spectral lines from 2.2-4.3 μm (Korablev et al., 2003), (Mahieux et al., 2008). Data is available at a wide variety of latitudes at the terminators between 70-170 km.

- James Clark Maxwell Telescope (JCMT) is a ground-based radio telescope in Hawaii that is capable of making sub-mm observations of CO absorption lines. Radiation emitted from the warmer, cloud-tops can be measured by the telescope and have a measurable dip in the continuum due to the absorption of the radiation by CO. Identifying that two different isotopes of carbon monoxide, ^{12}CO optically thick at 345 GHz and ^{13}CO optically thin at 330 GHz, react differently to the radiation helped retrieve densities and temperatures between 70-110 km. Due to the differences in day-night CO densities, the observation range may vary.

- Heinrich Hertz Sub-Millimeter Radio Telescope (HHSMT) is located at the Arizona Radio Observatory and provides temperature profiles and CO distributions from 40-120 km on the dayside and nightside (Rengel et al., 2008) on June 9th-10th,2007 and June 14th-15th, 2007. The temperature and CO density retrieval process is similar to that of JCMT, but is performed at 230.54 GHz and 220.4 GHz modifying the observable altitude range.

- Venus Express Radio Science (VeRa) used radio signals to sound Venus' atmosphere and ionosphere at all longitudes and latitudes during Venus atmospheric occultation (i.e., the signal is occulted by Venus's atmosphere). During the occultations, Venus' atmosphere lies between satellites radio transmitter and the ground station receivers or on Deep Space Network antennas. Measurements of the attenuated radio signals were used to derive atmospheric states. VeRa.0 and VeRa.1 provide density and temperatures from 40 km up to roughly 100 km (Häusler et al., 2006).

- Visible and InfraRed Thermal Imaging Spectrometer, high resolution channel (VIRTIS-H) observed non-LTE emissions of carbon monoxide as part of the Venus Express spacecraft. Gilli et al. (2015) presented dayside temperatures, albeit with large uncertainties, between 100-150 km at a variety of local time and latitude bins by averaging non-LTE emission measurements.

- Pioneer Venus' Orbiter Neutral Mass Spectrometer (ONMS) measured CO_2, O, CO, N_2, He, and N density variations at low latitudes in the upper thermosphere (Keating et al., 1979). The data observed from this instrument are the foundation for the VTS3 empirical model (Hedin et al., 1983).

- Pioneer Venus' Orbiter Electron Temperature Probe (OETP) used a cylindrical Langmuir probe to measure the current densities in various regions of the probe to back out electron temperature, ion and electron densities for the ionosphere of Venus (Krehbiel et al., 1980). The temperatures and densities are the basis for Theis et al. (1984); Theis and Brace (1993)'s model.

In addition to the data currently available, there have been three recently selected missions, VERITAS, DAVINCI, and EnVision which will probe the atmosphere of Venus with new instruments. Venus Emissivity, Radio Science, InSAR, Topography, and Spectroscopy (VERITAS) aims to improve upon the radar maps from the Magellan mission in the 1990s, help scientists learn about the nightside IR emissivity, and measure the gravitational field around Venus to gain insights on the planet's core. VERITAS, now delayed but optimistically scheduled to launch in 2031, will perform aerobraking maneuvers that will sample the thermosphere and provide further constraints on upper atmospheric structure. The Deep Atmosphere Venus Investigation of Noble gases, Chemistry, and Imaging (DAVINCI) mission is planned to launch as early as 2029. DAVINCI aims to deliver high precision measurements of the composition of the atmosphere as it descends through the thermosphere down to near surface altitudes (Garvin et al., 2022). EnVision, aiming to launch in the early 2030s, is set to become the first expedition to explore Venus from its innermost core all the way to its upper atmosphere, delineating the interplay amongst its distinct layers: its surface/subsurface, atmosphere, and interior. Its objective is to offer a comprehensive outlook of Venus, researching the planet's past, dynamics, and weather patterns (Widemann et al., 2020).

1.6 Outstanding Questions and Thesis Objectives

The focus of this thesis is to understand how the energy in the upper atmosphere at different planets controls temperatures, winds, densities and composition. As such, the primary goal of this work is to answer the following questions:

- What are the uncertainties in the thermodynamic source terms?
- How do uncertainties in the thermodynamics change the global and regional temperature structure?
- How do the uncertainties influence other terms like composition, density and neutral velocities?
- Due to the slow planetary rotation, how is a nightside ionosphere sustained at Venus?

These questions are addressed by using the Global Ionosphere Thermosphere Model (GITM) and altering the heating and cooling terms throughout the model to determine the impact on the rest of the domain for Earth and Venus.

1.7 Outline

The questions above are explored in the following chapters:

- Chapter 2 shares an introduction to many models (empirical and first-principles based) of Earth and Venus IT region.
- Chapter 3 discusses the inherent bias that comes with physics-based modeling. The work utilizes a technique called Retrospective Cost Model Refinement (RCMR) to significantly reduce the error in model predicted mass densities.
- Chapter 4 introduces a newly developed Venus model, the Venus Global Ionosphere Thermosphere Model (VGITM). V-GITM is used to simulate solar minimum conditions and predict the neutral and plasma densities, neutral winds and temperatures. Also, the effects of RSZ flow and the creation and structure of the nightside ionosphere of Venus are investigated.
- Chapter 5 expands on V-GITM work by simulating the solar moderate and solar maximum conditions. A sensitivity study is done on the different energy terms and a further investigation on the individual impact on the energy terms is performed.
- Chapter 6 summarizes all the findings and shares ideas for future work to improve IT modeling efforts and advance our understanding of the governing physics.
- Appendix A shows some of the chemical reaction rates included in V-GITM due to limited table space.

CHAPTER 2

Numerical Modeling and General Circulation Models

Empirical models attempt to combine available datasets with various mathematical techniques to fill in the holes of data to, in many cases, provide a three dimensional picture. These models have limitations with time-changing events like modeling a solar storm due to limited time periods of enhanced activity. Empirical models may also attempt to extrapolate data to outside of the actual domain of measurements, which can make the results unreliable. An alternative to empirical models is to use a General Circulation Model (GCM). GCMs, or physics-based models, estimate the thermosphere state variables using approximations of the Navier-Stokes equations. The idea is that correctly implemented physics could more accurately reproduce typical and highly-variable thermosphere conditions as observed during storms. Empirical models referenced in this work:

- MSIS: NRLMSISE-00 (referred to as MSIS). MSIS is an empirical model for Earth (Hedin et al., 1983; Hedin, 1987, 1991; Picone et al., 2002) that uses a spherical harmonic fitting of ground-based and satellite measurements to estimate neutral densities and temperatures of the thermosphere for any given solar conditions (F10.7) and geomagnetic activity (A_p).

- VTS-3: Similar to MSIS, VTS3 was created by Hedin et al. (1983) for Venus that used a spherical harmonic fitting of measurements from Pioneer Venus' Orbiter Neutral Mass Spectrometer (ONMS) from 1978 - 1980 to estimate measurements from 100 km to around 300 km. Sampled latitudes by ONMS (near equator) do not provide VTS-3 with useful mid-to-high latitude constraints. Also, ONMS in-situ datasets did not make measurements below about 140 km so extrapolations down to 100 km by VTS-3 are not well constrained. VTS-3 is used as a comparison tool for the model fully presented in Chapter 4.

- The empirical model from Theis et al. (1984) and Theis and Brace (1993) provide electron densities and electron temperatures for Venus extracted from Pioneer Venus' OETP using the method described in Krehbiel et al. (1980).

- Venus International Reference Atmosphere (VIRA) used both lower and upper atmosphere empirical datasets to capture reference profiles at specific locations and intervals throughout the solar cycle (Kliore et al., 1985). For instance, upper atmospheric mass densities and temperatures were based upon Pioneer Venus Orbiter (PVO) OAD datasets (Keating et al., 1985). VIRA-2 (Moroz and Zasova, 1997) updated the reference profiles based on composition, temperature and pressure measurements.

Relevant GCMs to this thesis:

- VTGCM: The Thermosphere Ionosphere General Circulation Model (TIGCM) (Dickinson et al., 1984) was modified to work at Venus (Bougher et al., 1988; Brecht et al., 2011, 2012; Parkinson et al., 2021). VTGCM is a 3D physics-based model on a pressure coordinate system. At the time, this model displayed the importance of 15 μm CO_2 cooling to balance EUV heating effects (Bougher et al., 1999). VTGCM also uses a wave-drag parameterization to reduce the horizontal wind speeds.

- GITM: Developed by Aaron Ridley, Yue Deng, and Gabor Tóth, the Global Ionosphere Thermosphere Model (GITM) (Ridley et al., 2006) is a 3D spherical model that solves the Navier Stokes equations for the ions, electrons and neutrals. Variations have been made for Mars (Bougher et al., 2015b), Titan (Bell et al., 2010; Bell et al., 2011) and Venus (this work). The Mars version, M-GITM, includes multiple models that are embedded in the code, including: (1) a model to simulate the effects of the dust in the lower atmosphere of Mars (Jain et al., 2020); (2) a modern NLTE CO_2 15 μm cooling scheme (Roeten et al., 2019) and (3) a FISM-M solar flux model, based upon MAVEN EUVM measured EUV-UV fluxes at Mars, is used to drive M-GITM solar heating, dissociation and ionization rates (Thiemann et al., 2017). A flat 20% EUV heating efficiency is used. M-GITM was the starting point when developing a Venus version of GITM which is discussed in Chapter 4.

- V-PCM: The Laboratoire de Météorologie Dynamique (LMD) team created a Venus GCM, formerly LMD-VGCM, (Gilli et al., 2017, 2021; Navarro et al., 2021; Martinez et al., 2023) now referred to as the Venus Planetary Climate Model (V-PCM). The V-PCM includes two unique parameterizations for the effects of the near IR solar heating at 4.3 μm and the radiative cooling at 15 μm. Additionally, a gravity wave parameterization is included to dampen the fast winds and improve stability of runs.

- TUGCM: Tohoku University's GCM (TUGCM) (Hoshino et al., 2012, 2013) uses an atmosphere of O, CO and CO_2 only and implements planetary scale waves (Rossby waves, diurnal and semidiurnal tides, and Kelvin waves) based on the assumption that these are driven upward from the mesosphere.

2.1 Finite Difference Approximations

The GCMs described above rely on ”solving” physics-based equations to obtain answers to a specific problem. While methods vary significantly, a visual way to understand how one model progresses over time is shown in Figure 2.1. This shows the vorticity within a box where the upper wall, at y = 1, begins moving in the positive x-direction. As seen in Figure 2.1a, a grid is created and initial values of a specific state variable are given. In this case, the variable of interest is the vorticity which is initialized to zero. The vorticity of a fluid is described as:

$$\overrightarrow{\omega} = \nabla \times \overrightarrow{v} \tag{2.1}$$

After a short amount of time, see 2.1b, the upper wall moves taking fluid with it. The non-stationary fluid at the top eventually interacts with the wall at x = 1 and begins diffusing and rotating clockwise. As time progresses to 100 seconds in 2.1c, the fluid flow is more developed and fluid in the center and lower portions of the box are now rotating too.

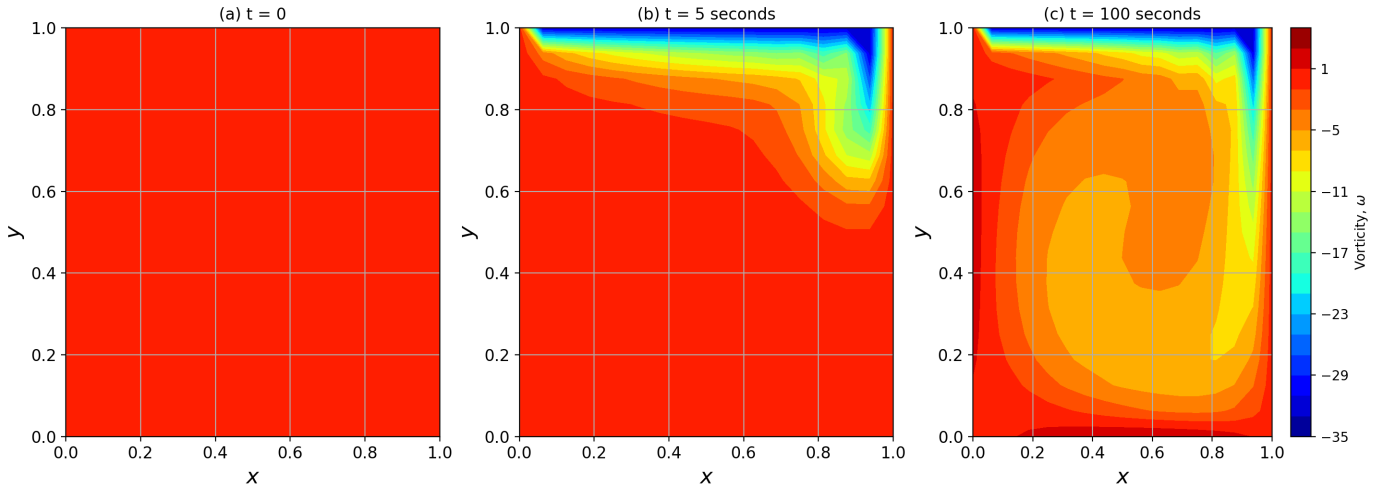

Figure 2.1: The vorticity field in a box of (a) initially stationary fluid. The upper wall then moves and the simulated vorticity is shown after (b) 5 seconds and (c) 100 seconds. Negative vorticities correspond to clockwise angular velocities of the fluid.

One particularly relevant differential equation important to upper atmospheres is the continuity equation. This equation is numerically solved in virtually every planetary GCM. The continuity equation describes the conservation of mass and can be expressed in one-dimension as:

$$\frac{\partial \rho}{\partial t} + \nabla \cdot (\rho u) = 0 \tag{2.2}$$

where the first-term is the time rate of change of the mass density ρ and the second term describes

the influence of advection on the fluid. This equation is used to look at how this (and other differential equations) can be solved. Equation (2.2) in differential form will have a spatial derivative, in the form of $\frac{\partial u}{\partial x}$, and a temporal derivative, $\frac{\partial \rho}{\partial t}$. This term can be approximated using a forward finite-difference scheme:

$$\frac{\partial u}{\partial x} \approx \frac{u_{i+1} - u_i}{\Delta x} \tag{2.3}$$

where u_i is the velocity at a specific node, i. u_{i+1} is the fluid velocity at a grid point the next node and Δx is the spacing between node i and $i + 1$. The time-derivative term can be approximated using a forward difference in time:

$$\frac{\partial \rho}{\partial t} \approx \frac{\rho^{n+1} - \rho^n}{\Delta t} \tag{2.4}$$

where ρ^n is the mass density of the fluid at a specific timestep n. Δt is the time spacing between the states of n and $n + 1$. Rewriting equation (2.2) with (2.3) and (2.4) and solving for the new mass density, ρ^{n+1}:

$$\rho_i^{n+1} = \rho_i^n - \frac{\Delta t}{\Delta x}[\rho_i^n(u_{i+1}^n - u_i^n) + u_i^n(\rho_{i+1}^n - \rho_i^n)] \tag{2.5}$$

Finally, an updated mass density can be solved for using the the existing density, velocity at the current node and one other node, a Δt and Δx. Determining the grid spacing and time steps are subject to a condition known as the Courant-Friedrichs-Lewy (CFL) stability criteria (Courant et al., 1928). The CFL number determines the maximum time step size that can be used in a numerical simulation to ensure stability. The CFL condition states that the time step size should be smaller than a certain fraction of the smallest characteristic length scale divided by the maximum wave speed in the system being modeled. The CFL condition is important because it ensures that the numerical solution remains stable and accurate, and prevents the appearance of instabilities.

Equations (2.3) and (2.4) are arguably the simplest approximations and subject to numerical errors. Many efforts in the numerical methods community have been given to come up with new ways to approximate these derivatives with the least amount of error. Variations of the Leapfrog and Runge-Kutta 4 are some of the advanced methods that are used in the solve the equations in GCMs (DeVries and Wolf, 1994). Although this has been specifically used for the continuity equation, the basic method presented here is applicable to other fluid equations.

2.2 Energetics

At a high level, the Navier-Stokes equations commonly express the concepts of the conservation of mass, momentum and energy in the form of partial differential equations. With different as-

sumptions, the Navier-Stokes are applied in fields like biomedical sciences simulating blood flow through arteries (Fojas and De Leon, 2013) or in animated movies and games where they want to immerse the viewer in realistic environments with dynamic movements of clouds, smoke and water (Stam, 2003; Teran, 2018). Applying these equations to the field of aeronomy and planetary sciences is common as well.

As the focus of this thesis is the thermal balance of atmospheres, the conservation of energy is a thermodynamic principle which affirms that energy is always conserved in any process. Energy can be transformed from one form to another, such as from potential energy to kinetic energy or from chemical energy to electrical energy, but the total amount of energy in the system remains the same. Solving the Navier-Stokes equations is difficult analytically, but can be done via discretization of the equations and using iterative numerical methods. The various versions of GITM attempt to solve the set of intertwined equations for the different thermospheric fluids (neutrals, ions and electrons). Table 2.1 shows the subset of equations for each version of GITM.

	Earth			Mars			Venus		
	Neutrals	Ions	Electrons	Neutrals	Ions	Electrons	Neutrals	Ions	Electrons
Continuity	✓	✓	$\sum n_i$	✓	✓	$\sum n_i$	✓	✓	$\sum n_i$
Momentum	✓	✓	✓	✓	✓	-	✓	✓	-
Energy	✓	✓	✓	✓	(Fox, 1993)	(Bougher et al., 2017)	✓	$T_i = T_n$	(Fox and Sung, 2001)

Table 2.1: An overview of the different sets of equations applied to the versions of GITM.

The neutral energy equation is generally described in GITM as:

$$\frac{\partial T}{\partial t} + u \cdot \nabla T + (\gamma - 1) T \nabla \cdot u = Q \tag{2.6}$$

where the first term is the time rate of change for the neutral temperature. The second term is advection with u being the fluid velocity. The third term is the change in energy from the expansion of the gas where γ is the adiabatic index. On the right-hand-side, Q is energy sources and sinks which will vary depending on the planetary atmosphere. Example source terms included in the Venus atmosphere are:

$$\begin{aligned} Q = Q_{EUV} + Q_{IR} + Q_O + Q_{CO_2} + Q_{CHEM} + Q_{DISS} + \frac{\partial}{\partial r}((\kappa_c + \kappa_{eddy})\frac{\partial T}{\partial r}) + \\ \sum_i n_i m_i \sum_n \frac{\nu_{in}[3k(T_n - T_i) + m_n(v-u)^2]}{m_i + m_n} \end{aligned} \tag{2.7}$$

where Q_{EUV} and Q_{IR} are the contribution from the Sun's extreme ultraviolet and infrared. The Q_O and Q_{CO_2} are terms detail the cooling to space from the 63 μm and $15 \mu m$ bands respectively.

Q_{CHEM} combines heat generated from exothermic reactions. Q_{DISS} is heat generated from a photon with energy greater than the dissociation threshold. The implementation of this is described more in Chapter 5. Next to the final term, κ_{eddy} is the contribution of heat conductivity due to eddy diffusion coefficient (EDC) and κ_c is the molecular heat conductivity due to thermal conduction. The final term is the Joule heating generated in the form of frictional heating and collisional heat transfer between ions and neutrals. This is a function of the ion density (n_i), mass of the ion (m_i), mass of the neutrals (m_n), the ion-neutral collision frequency (ν_{in}), the ion velocity (v_i), neutral velocity (u_n), ion temperature (T_i) and the neutral temperature (T_n).

2.2.1 Extreme Ultraviolet

GITM implements EUV energy in many different ways. At Mars and in many other planetary GCMs, a proxy model such as EUVAC (Richards et al., 1994) or Flare Irradiance Spectral Model (FISM) (Chamberlin et al., 2008) is used. EUVAC uses the 10.7 cm solar radio flux to estimate the top of atmosphere flux in 37 wavelength bins spanning 5-105 nm. On the other hand, FISM uses measurements from a spacecraft such as TIMED (Woods et al., 2005) or MAVEN (Eparvier et al., 2015) to provide the top of atmosphere flux. The wavelength range for FISM is 0.1 nm to 190 nm at a finer resolution. While more computationally expensive, a wider spectrum range and finer resolution is more accurate. Additionally, the time cadence of FISM is on the order of 1 minute compared to the F10.7-dependent, EUVAC values which are daily values. This makes FISM a more useful EUV model when studying time-changing phenomena like solar flare effects.

From the top of the atmosphere, the EUV flux may be attenuated by the fluid as it is passing through. The attenuation depends on an exponential function related to the fluid's optical depth, τ:

$$I(z,\lambda) = I_\infty(\lambda)e^{-\tau} \tag{2.8}$$

where $I(z,\lambda)$ is the radiation flux at a particular altitude, z, and I_∞ is the top of atmosphere flux described above. To compute τ:

$$\tau = \int_\infty^z \sum_s \sigma_a n_s(z) ds \tag{2.9}$$

where σ_a is the photoabsorption cross-section, n_s is the species-specific number density, and ds is the incremental path length. Venus optical depths calculated at 1.5, 175, 425, 675, and 975 angstroms are shown in Figure 2.2. Previously measured photoabsorption, photodissociation and photoionization cross-sections determine the effectiveness of the absorption of specific radiation bands. Heays, A. N. et al. (2017) has compiled more than 100 different atoms and molecular photoabsorption, dissociation and ionization cross-sections in 0.1 nm spacing. This data is stored in

the Leiden Observatory database (https://home.strw.leidenuniv.nl/ ewine/photo/). The incremental path length can be simplified based on geometry at low solar zenith angles, but as the solar zenith angles increase, such as at the terminators, this method breaks down. A Chapman function is used within GITM to account for this (Smith III and Smith, 1972).

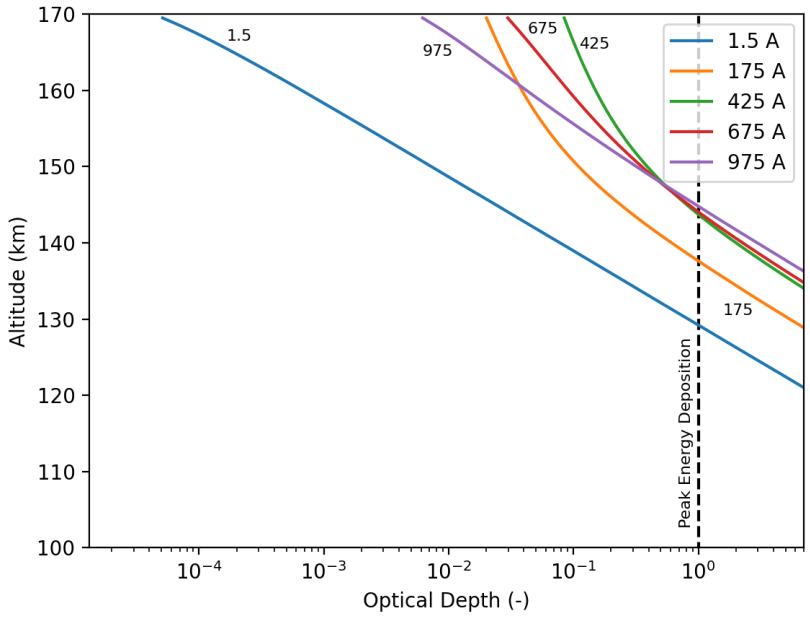

Figure 2.2: The spectral optical depths of five lines computed in V-GITM at 12 LT. The dashed black line at 10^0 indicates where the maximum absorption of radiation occurs.

As the radiation is absorbed, many models will assume a fixed percentage of the total absorbed energy is deposited into the atmosphere as heat. This fixed percentage is the heating efficiency. The EUV efficiency is an uncertain, simplifying parameter in the modeling community and is subject to much scrutiny (Torr et al., 1980; Hollenbach et al., 1985; Fox, 1988; Huestis et al., 2008; Gu et al., 2020). In some works, the heating efficiency is used to approximate direct heating due to EUV, chemical heating, photodissociation heating, photoelectron heating, or other processes. For GITM, an otherwise, commonly used value for the heating efficiency (such as 10-25%) is difficult to adopt, because the terrestrial and Venus versions of GITM self-consistently compute the heat generated from chemical reactions.

2.2.2 Photodissociation

Photodissociation is a source term recently added to energy equation (see equation 2.7). Photodissociation, also known as photolysis, is a process in which a molecule is broken down into smaller

fragments by absorbing radiation. This process occurs when a molecule absorbs a photon of sufficient energy to break one or more chemical bonds. The energy required for photodissociation is typically in the ultraviolet or visible range of the electromagnetic spectrum. When photons with energies larger than the energy required to break a chemical bond, it is understood that a fraction of the excess energy will go into translational energy for the newly dissociated molecules. The method used to model this process is:

$$Q_{diss}(z) = f_T \sum_{\lambda} (E_\lambda - E_0) P(\lambda, z) \tag{2.10}$$

where λ is the photon wavelength; E_λ is the energy of an incoming photon greater than the dissociation threshold, E_0; and f_T is the fraction of excess energy appearing as translational energy. P(λ) is the dissociation production rate at a specific wavelength and is given by:

$$P(\lambda, z) = I(\lambda, z)\sigma(\lambda)n \tag{2.11}$$

where I is the attenuated intensity, σ is the dissociation cross-section, and n is the species-specific number density.

2.2.3 Solar Near IR and NLTE 15 μm cooling

The source of near infrared heating is due to absorption of solar radiation in the CO_2 near IR wavelength bands between 2-4 μm (Dickinson and Ridley, 1977). Energy absorbed in these wavelengths may raise the CO_2 molecule into an excited state due to its many vibrational levels. Depending on the vibrational pathway, secondary processes can begin such as the emission of 15 μm that is easily lost to space. For this reason, the heating and cooling of near IR and 15 μm need to be coupled in a detailed line-by-line radiative transfer code. Models have parameterized heating and cooling rates to mimic Roldán et al. (2000)'s radiative transfer estimations (Gilli et al., 2017). The same model updated their parameterization to best-fit GCM temperatures to satellite measurements (Gilli et al., 2021). Finally, Martinez et al. (2023) has expanded the parameterization into a wavelength multi-band parameterization. Due to the complicated and expensive nature of accurately computing the full radiative transfer effects of solar IR absorption, GITM has taken a similar approach for absorbing near IR radiation to that which was performed on the EUV. Two wavelengths, 2.7 μm and 4.3 μm, were added to the wavelength spectrum. Top of atmosphere fluxes and absorption coefficients were computed to fit the computed heating rate to commonly accepted rates. A major difference between the parameterizations in Gilli et al. (2017, 2021); Martinez et al. (2023) and the method used in GITM is the handling of terminator effects. The parameterizations previously mentioned utilize a cosine of the solar zenith angle to compute the appropriate flux. Smith III and

Smith (1972) demonstrated that for large solar zenith angles, greater than 90°, radiation can be transmitted through the atmosphere at higher altitudes. For these reasons, it is not expected that the Gilli et al. (2017, 2021); Martinez et al. (2023) will have significant heating occurring at and beyond the terminators.

The 15 μm cooling is the primary mechanism for balancing the near IR heating at Venus (Bougher et al., 1986; Roldán et al., 2000). Atomic oxygen is responsible for collisionally exciting CO_2 into a 15 μm vibrational state. To return to its ground state, the radiation is emitted and lost to space due to the transparency of the atmosphere to 15 μm radiation. The cooling effects follow the M-PCM (formerly LMD-MGCM) non-LTE paramaterization (González-Galindo et al., 2013). The non-LTE parameterization simplifies the full problem into 5 rotational and vibrational levels, computes heat transfer between atmospheric layers and allows for spatially variable atomic oxygen densities to be pulled directly from the model at each time step. This code has been used in the LMD-MGCM, LMD-VGCM, and M-GITM models (Bougher et al., 2017; González-Galindo et al., 2013; Gilli et al., 2017, 2021). Due to the importance of CO_2 cooling in the LTE portion of the thermosphere and the non-LTE nature of this model, the lower thermosphere and middle atmosphere are cooled using a linear extrapolation from approximately 70-95 km.

2.2.4 O Cooling

Atomic oxygen is capable of emitting infrared radiation at 63 μm when O(^{3}P) transitions between specific states. Similar to the representation of CO_2 cooling, a full radiative transfer code is necessary to accurately represent the cooling rate but an approximation based on O(^{3}P) and the local temperature is given by (Kockarts and Peetermans, 1970). This has not been representative of LTE effects and so the non-LTE cooling rates are reduced by a factor of 2 matching the work of Roble et al. (1987).

2.2.5 Thermal Conduction and Eddy Diffusion

Thermal conduction within GITM represents the transfer of heat vertically between neutral particles. κ_c (also referred to as λ in other publications), is parameterized as:

$$\kappa_c = \sum_i [\frac{N_i}{N_{total}}] A_i T^s \tag{2.12}$$

where N_i/N_{total} is a weighting factor by number density of each neutral species, T is the thermosphere temperature, A_i and s are species specific thermal conductivity coefficients to fit the total conductivity as needed. The summation includes the three species with the largest concentrations in the thermosphere. At Earth, this includes N_2, O_2 and O, but Venus modifies this to include CO_2

as well. Unlike Venus and Earth, the M-GITM followed the method used in Banks and Kockarts (1973).

Eddy diffusion, κ_{eddy}, approximates efficiency of turbulent mixing of the atmosphere. Many efforts have been done at Venus, Earth and Mars to estimate this term and it is still highly uncertain (von Zahn et al., 1980; Pilinski and Crowley, 2015; Malhotra and Ridley, 2020; Mahieux et al., 2021). Depending on the implementations, eddy diffusion can have effects on neutral and plasma densities, wind speeds and temperatures. As shown in Figure 2.3, different planets within GITM implement different eddy diffusion coefficient values and profile shapes. A sensitivity study varying this term at Venus is shown later in Chapter 5.

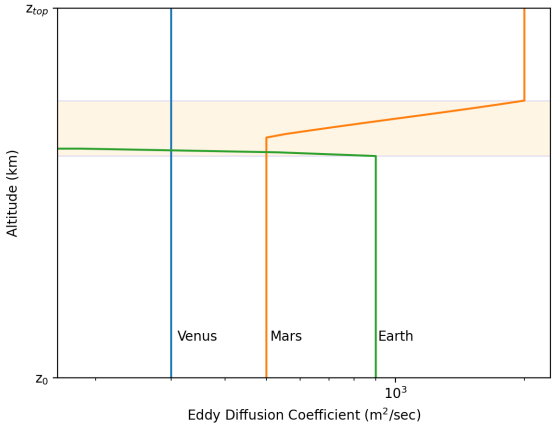

Figure 2.3: Eddy diffusion profiles for the different planets GITM models on ambiguous vertical domains. The highlighted region is shown to visualize pressure blending of different eddy diffusion regions.

2.2.6 Collisional Heating

Heat is generated in two more ways between ion-neutral interactions. Ions and neutrals that do not move together will produce frictional heating as partially described in equation (2.7). The frictional and heat transfer terms within GITM for Earth are detailed in Zhu and Ridley (2016).

Frictional heating is an important term at Earth where the ions and neutrals move differently, which can be due to electromagnetic forces generated by the intrinsic magnetic field. Due to the lack of significant, intrinsic electromagnetic fields in Venus' and Mars' thermosphere, the ions and neutrals move together making this an insignificant term at these planets. The existence of dynamo effects and the consequent collisional heating are being explored at Mars in regions of strong crustal magnetic fields (Fillingim et al., 2010).

Also in equation (2.7), contains the difference between the ion and neutral temperatures which is referred to as heat transfer. This is due to different temperature particles colliding and exchanging

heat during their interactions. Heat transfer, while important is dependent on an accurate representation of the ion energy equation. As shown in Table 2.1, only Earth self-consistently solves for the ion temperature. Mars approximates the ion temperature based on profiles published in Fox (1993). MAVEN ion temperatures were recently assembled from SupraThermal And Thermal Ion Composition (STATIC) measurements (Hanley et al., 2022). However, 3-D model usage is not yet available for M-GITM. For Venus, it is assumed that the ion and neutral temperatures are identical making the heat transfer zero.

2.3 Boundary Conditions

Boundary conditions are specifications of quantities at the boundaries of the model domain. They are supposed to act as contingent facts about a system, but due to the complexity and constantly changing space of thermosphere/ionosphere modeling, it becomes a helpful simplification. For example, one boundary condition for GITM is the specification of the atomic oxygen at $\sim$100 km (Malhotra and Ridley, 2020). The physics and chemistry models within GITM take the number density into consideration driving changes in chemical reaction rates, number densities above 100 km, temperatures, wind profiles, etc... For this reason, a correct specification of atomic oxygen (and other boundary conditions) are important. The difficulty with this is that the atomic oxygen at 100 km is not a fixed value. It may change with local time, season, or just during the course of a model simulation and any simplified handling of this boundary condition will propagate error into other, difficult to track state changes.

Within GITM, each species-specific number density is prescribed at the lower boundary. While there are multiple ways to do this, it is typically done using an empirical model such as MSIS or VTS3 (Hedin et al., 1983; Hedin, 1983). At the upper boundary, the neutral densities follow a hydrostatic decrease based on scale heights and the densities below. Regarding the ionosphere boundary conditions, GITM's lower domain typically is below the start of the ionosphere making it a less important condition to explicitly specify to. At Venus, a constant gradient is used at the lower boundary for ion densities which usually results in the densities being maintaining a value of essentially zero. Being a coupled thermosphere-ionosphere model, the upper domain of GITM extends well into the ionosphere where an exponential decrease is used at the top boundary. A more appropriate upper boundary condition would be to use in-situ plasma density measurements or an ionospheric empirical model.

The upper boundary condition for the temperature is to maintain an isothermal temperature profile. At the lower boundary, the value may be expressed, similar to the number densities, via an empirical model. The horizontal neutral winds for Earth use the Horizontal Wind Model (Drob et al., 2015). Venus-specific wind patterns and the corresponding boundary conditions are dis-

cussed more in Chapter 4.

Boundary conditions are necessary for a model to function, but are considerable sources of error due to their inherent uncertainty and variability. Consequently, the influence of many boundary conditions have been studied (Malhotra and Ridley, 2020; Liu et al., 2018; Jones Jr. et al., 2021).

2.4 State Estimation and Measurement Filtering

2.4.1 Kalman Filtering

Kalman (1960) introduced such a revolutionary filtering approach to the discrete optimal filtering problem that initially it was rejected as "cannot possibly be true". Kalman filtering has been the foundation for state estimation for more than 60 years. Kalman filters perform a weighted average of a prediction model with measurements of the state to produce a better estimate of the state. The weighting is proportional to the quality of both the prediction and the measurements. It begins by propagating the predicted state. For example, a car may be driving along a road and the state variables of interest could be the car's position. A simple prediction model for this could be:

$$x^{n+1} = x^n + v^n \Delta t \tag{2.13}$$

At this point, the initial position (x^n) and velocity (v^n) may be known and a time step (Δt) is used to predict the new position (x^{n+1}). With this prediction model, there are a variety of possible errors. The fundamental equation could be omitting important physics terms. In this case, assuming a constant velocity, ignoring the effects of drag on the car, or friction between the tires and the road would lead to the actual position of the car being inconsistent with the predicted position. For this reason, a measurement is obtained and integrated into the problem to quantify the accuracy of the prediction model. Another source of error can be found in the random noise that occurs of the measurement device. After a prediction and measurement are performed, then a parameter to quantifying the quality of the prediction model compared to the uncertainty in the measurement is computed. This is called the Kalman gain. The gain is placed on the prediction model and measurement to update the prediction model with an appropriate weighting on the prediction model or an adjustment factor to offset the error in the prediction model. Then the state is updated:

$$x^{n+1} = (1 - K_g)(x^n + v^n \Delta t) + K_g z \tag{2.14}$$

The strength of the Kalman filter lies in its ability to fuse noisy measurements with a dynamic model of the system to provide an optimal estimate of the state. It operates by minimizing the

mean squared error between the estimated state and the true state. The Kalman filter assumes linearity and Gaussian distributions for the system dynamics and measurement models, respectively. However, in practice, it can be extended to handle non-linear systems using techniques such as the extended Kalman filter or the unscented Kalman filter.

2.4.2 Extended Kalman Filter

The Extended Kalman Filter (EKF) is an extension of the standard Kalman filter that allows for estimation and prediction in nonlinear systems. While the original Kalman filter assumes linearity, the EKF handles systems with nonlinear dynamics and measurement models. The key difference between the Kalman filter and the extended Kalman filter lies in the way they handle nonlinearities. In the standard Kalman filter, the dynamics and measurement models are assumed to be linear, and the filter operates based on linear algebra. However, in the EKF, the nonlinear models are approximated by linearizing them around the current estimated state.

The EKF linearizes the nonlinear models by computing the Jacobian matrices, which are the matrices of partial derivatives of the nonlinear functions with respect to the state variables. These Jacobians capture the local linear behavior of the system at the current estimated state. Although the EKF allows for estimation in nonlinear systems, it has some limitations. The linearization process introduces errors, and if the nonlinearities are significant or the system operates far from the linearization point, the EKF may provide inaccurate results. In such cases, other nonlinear filtering techniques may be more appropriate.

2.4.3 Ensemble Kalman Filtering

The Ensemble Kalman Filter (EnKF) is a variant of the Kalman filter that addresses the limitations of the standard Kalman filter when dealing with large-scale systems or nonlinearities. The main difference between the Ensemble Kalman Filter and the standard Kalman filter lies in their approach to handling uncertainty. Instead of relying on a single estimate of the state, the EnKF maintains an ensemble of state estimates, which is expected to contain an accurate representation of the system state.

The EnKF operates by propagating the ensemble of states through the system's dynamics model and updating it based on measurements. The propagation step involves applying the dynamics model to each ensemble member to obtain a predicted ensemble of states. In the update step, the predicted ensemble is adjusted based on the available measurements. Unlike the standard Kalman filter, which uses the measurements directly to update a single state estimate, the EnKF updates the entire ensemble of states. This update is performed by computing a correction term for each ensemble member based on its deviation from the predicted measurement. The EnKF incorporates

both the ensemble spread (the variability among the ensemble members) and the measurement uncertainty to update the ensemble of states. The spread acts as a measure of uncertainty and helps to account for nonlinearities and model errors in a more robust manner than the standard Kalman filter.

By maintaining an ensemble, the EnKF captures the statistical distribution of possible system states, providing a more comprehensive representation of uncertainty. This ensemble-based approach allows the EnKF to handle nonlinearity and provide more accurate estimates in situations where the standard Kalman filter may struggle. It is worth noting that the EnKF requires generating and propagating multiple state estimates, making it computationally more demanding than the standard Kalman filter.

2.4.4 Summary

State estimation techniques are insufficient to adequately address the problem of space weather modeling and forecasting. This is because state estimation and Kalman filtering performance degrades as observational data becomes absent, such as in weather forecasting. For this reason, hybrid modeling based on physics is necessary to estimate atmosphere states. The physics included these models are uncertain, but could be estimated through a parameter estimation technique, such as retrospective cost model refinement. This is the motivation for Chapter 3.

CHAPTER 3

Improving Forecasting Ability of GITM Using Data-driven Model Refinement

This chapter is taken from Brandon M. Ponder, Aaron J. Ridley, Ankit Goel, D. S. Bernstein (2023), "Improving Forecasting Ability of GITM using Data-driven Model Refinement" [Ponder et al. (2023)].

Plain Language Summary

Physics-based models have a difficult time accurately estimating the upper atmosphere density. These densities are needed to compute satellite orbit trajectories to monitor for potential collisions. Inaccurate density estimation can be due to variety of factors and so methods of correcting the model-predicted density are needed. We are presenting a method to correct the densities using available satellite measurements from the CHAMP and GRACE satellites and the commonly used empirical model NRLMSISE-00. Upon reducing the model error, we show the improved ability of a physics-based model to capture a geomagnetic storm.

3.1 Introduction

Orbit estimation of drag along a satellite path for collision avoidance is growing in importance due to the increased risk of collisions as more objects are being launched into low Earth orbit. Satellites are expensive to build, launch and maintain (Saleh et al., 2004) and there is an increasing collision risk posed by over twenty thousand pieces of space debris larger than 10 cm^3 (Garcia, 2021). In response to the threat of collisions, the Joint Space Operations Center (JSpOC) continuously monitors orbiting objects' positions and velocities. From its database, it computes a probability of collision between two bodies and will issue a Conjunction Data Message (CDM) to the mission

operator for further action (Hejduk and Frigm, 2015), (Bussy-Virat et al., 2018). Then a collision avoidance maneuver could be performed, costing time of inactivity and fuel.

There are underlying assumptions to the advanced computing technique of predicting a collision. One assumption is the drag force estimation used to solve the kinematic equations. The acceleration ($\underline{a}$) experienced due to satellite drag is proportional to the ratio of surface area (A) to mass (m) of the spacecraft, coefficient of drag (c_D), the atmospheric density (ρ) and the velocity, relative to a rotating atmosphere, squared (v):

$$\underline{a} = -\frac{1}{2}\frac{A}{m}c_D\rho\underline{v}^2\hat{v} \tag{3.1}$$

where density is the largest uncertainty in this equation.

Attitude control is a related topic that requires properly estimating the drag-induced torques on a satellite to control its orientation. This could be important for instrumentation to function properly. Part of the attitude control problem is bounding torques to ensure systems do not get overwhelmed. Alternatively, over-engineering a powerful attitude control system costs extra money. The accuracy of torque prediction is reliant on low-error density estimation too. Moorthy et al. (2021) describes the importance of attitude control and the potential impact to expand our ability to explore extremely low Earth orbits (150-250 km). This region of Earth's atmosphere is under-explored due to the large drag force causing short expected lifetimes.

Accurately predicting the density in the thermosphere is a difficult task and atmospheric models are often called upon to make these density-driven drag estimations, but can be inaccurate by 20% ((Kuang et al., 2014), (Marcos, 1990), (Bruinsma et al., 2004)). The errors in the prediction are amplified during a geomagnetic storm, largely due to poor density estimation (Pachura and Hejduk, 2016). Drag inaccuracies can create positioning errors on the order of 10 km after just one day. In a short period of time, the satellites' trajectory can change enough such that JSpOC may need to reacquire them.

One of the models available to estimate density is NRLMSISE-00 (referred to as MSIS). MSIS is an empirical model ((Hedin et al., 1983), (Hedin, 1987), (Hedin, 1991), (Picone et al., 2002)) that uses a spherical harmonic fitting of ground-based and satellite measurements to estimate neutral densities and temperatures of the thermosphere for given solar conditions (F10.7) and geomagnetic activity (A_p). Empirical models incorporate data from remote observations so they are able to capture background neutral densities well, but do not have the same success during a solar storm due to limited time periods of enhanced activity. Wang et al. (2022) analyzed 265 storms, showed that MSIS under-predicted the density during storms, and fit coefficients to improve MSIS's peak density prediction during weak, moderate and intense storms.

The Jacchia-Bowman 2008 Empirical Thermospheric Density Model (JB2008) (Bowman et al.,

2008) is an empirical model that estimates total mass density. JB2008 is a series of improvements upon the Jacchia 70 model (Jacchia, 1970) changing the input for the geomagnetic indices (from A_p to D_{st}) and adding to the input for the solar indices using orbit-based sensor measurements of solar data in the EUV and far EUV (FUV) wavelengths. As part of the change from Jacchia 70, Bowman (2004) concluded that a Fourier time series and an altitude dependent, quadratic function could accurately replace the existing Jacchia 70 density functions used to compute the semidiurnal density variation. Bowman et al. (2006) introduced EUV and FUV solar indices into their temperature equation, replacing the standard Jacchia temperature equation. The accumulation of these changes led to lower standard deviation in errors, particularly during solar minimum conditions and during major geomagnetic storms.

There are two common issues with models: (1) bias during background conditions where mean densities from the model differ from mean measurements over a period of several days or longer and (2) enhanced errors over periods of a couple of days, driven by space weather events like storms. There are many ways people have tried to address these issues of poor density estimation.

The High Accuracy Satellite Drag Model (HASDM) (Storz et al., 2005) is an extension of JB2008 used by the US Space Force Combined Space Operations Center which uses observed drag effects from approximately 75 Earth-orbiting spheres to compute diurnal and semidiurnal variations to the thermosphere density. Doornbos et al. (2008) has done work with two-line element (TLE) data to directly create altitude-dependent multiplication factors to scale the densities of empirical models. Brandt et al. (2020) created the Multifacted Optimization Algorithm (MOA) which similarly uses TLE data to incrementally adjust the drivers for MSIS within the orbital propagator (SpOCK) (Bussy-Virat et al., 2018). MOA adjusts the drivers of MSIS when MSIS has a large bias or misrepresents a storm to bring SpOCK-predicted orbits in line with TLEs from several small satellites. Lastly, (Kalafatoglu Eyiguler et al., 2019) showed that debiasing a model's background density prior to a storm may lead to improved performance for some models and recommends a few calculations for assessing storm-time performance.

Physics-based models estimate the thermosphere state variables using approximations of the Navier-Stokes equations. The idea is that correctly implemented physics could more accurately reproduce typical and highly-variable thermosphere conditions as observed during storms. Coupled Thermosphere Ionosphere Model (CTIM) (Fuller-Rowell and Rees, 1980), Thermosphere Ionosphere Electrodynamics General Circulation Model (TIEGCM) (Richmond et al., 1992) and Global Ionosphere Thermosphere Model (GITM) (Ridley et al., 2006) are examples of Earth-based, physics models. The different numerical approximations, source terms included (or not included), and drivers in each model generates different temperatures, wind structures and densities. TIEGCM and CTIM use the hydrostatic assumption, whereas GITM does not make the same hydrostatic equilibrium assumption and solves a more complete vertical momentum and energy

equation, but takes significantly longer to run. GITM makes use of the Flare Irradiance Spectral Model (FISM) (Chamberlin et al., 2008) fluxes to better represent the solar EUV entering the atmosphere.

Matsuo et al. (2013) used an ensemble Kalman filter to assimilate CHAMP measurements in the TIEGCM and in turn back out solar forcing terms such as the F10.7 index. Their work also demonstrated that electron density profiles from COSMIC can infer neutral states better than a single satellite's measurements of in-situ neutral densities. Progressing on this work, indirect and direct measurements of electron densities were used to determine the effectiveness of orbit propagation and quantify the improvements to ionosphere-thermosphere states ((Matsuo and Hsu, 2021)(Dietrich et al., 2022)). Matsuo and Hsu (2021) also pointed out that after removing the bias, forecasting neutral densities remained reliable for the next three days in geomagnetically quiet conditions. It is important that a balance be struck when assimilating data without addressing the model drivers/parameterizations because during active time periods, the fundamental physics is needed to capture the fast changing states. Sutton (2018) points this out and developed the Iterative Reinitialization, Driver Estimation, and Assimilation (IRIDEA) technique which has demonstrated that assimilating satellite measurements in TIEGCM to modify solar and geomagnetic indices (drivers for models) improve active time period errors.

This study presents work on debiasing the background density in GITM using observational data. It also shows the impact of debiasing a model prior to a geomagnetic storm using satellite measurements and the MSIS model.

3.1.1 The Global Ionosphere Thermosphere Model (GITM)

Understanding the parameters that affect the thermosphere's neutral density are critical for improving physics-based models like GITM. GITM is a 3D spherical model that is used for Earth (Ridley et al., 2006), Mars (Bougher et al., 2015a) and Saturn's moon Titan (Bell et al., 2010). In this study, the resolution of GITM was 2° latitude and 4° in longitude.

Ridley et al. (2006) explains the capabilities of the model, including the chemistry and numerical schemes. The vertical energy equation in GITM, including source terms, is (Ridley et al., 2006):

$$\frac{\partial \mathcal{T}}{\partial t} + u_r \frac{\partial \mathcal{T}}{\partial r} + (\gamma - 1)\mathcal{T}\left(\frac{2u_r}{r} + \frac{\partial u_r}{\partial r}\right) = \frac{k}{c_v \rho \bar{m}_n} Q \tag{3.2}$$

where the first term is the time rate of change for the normalized, neutral temperature, $\mathcal{T} = kT/\bar{m}_n$. The second term is the advection of temperature gradients, while the third term is the adiabatic heating, which is a result of the divergence of the velocity. This is is only the vertical component which depends on the vertical velocity, u_r, radius of the Earth, r, and the temperature gradient. γ is the adiabatic index that is attached to the change in energy from the expansion of the gas. On the

right-hand side, c_v is the specific heat, k is Boltzmann's constant, ρ is the mass density, and $\bar{m}_n$ is the mean mass of the neutrals. The various source terms are given by:

$$Q = Q_{EUV} + Q_{NO} + Q_O + \frac{\partial}{\partial r}((\kappa_c + \kappa_{eddy})\frac{\partial T}{\partial r}) + \sum_i n_i m_i \sum_n \frac{\nu_{in}[3k(T_n - T_i) + m_n(v-u)^2]}{m_i + m_n} \tag{3.3}$$

where: Q_{EUV} is the contribution from the solar extreme ultraviolet irradiance; the Q_{NO} and Q_O terms are the cooling to space from the 5.3 μm and 63 μm bands respectively. The last term is the collisional frictional heating and heat transfer between ions and neutrals. This is a function of the ion density (n_i), mass of the ion (m_i), mass of the neutrals (m_n), the ion-neutral collision frequency (ν_{in}), the ion velocity (v_i), neutral velocity (u_n), ion temperature (T_i) and the neutral temperature (T_n). Finally, the fourth term is the thermal conductivity, where κ_{eddy} and κ_c are the conductivity coefficients due to eddy diffusion and molecular heat conductivity respectively, and is the focus of this study.

3.1.2 Thermal Conductivity in the Upper Atmosphere

Thermal conductivity uncertainty is a serious issue in physics-based models ((Banks and Kockarts, 1973), (Pawlowski and Ridley, 2009), (Schunk and Nagy, 2004)). Most of the literature describes thermal conductivity in a laboratory setting where it is expressed as a function of temperature alone for specific species (Vargaftik et al., 1993). The theoretical expression for the thermal conductivity coefficient (κ_c) are complex and so it has been useful to simplify the coefficient to be a parameterization ((Banks and Kockarts, 1973), (Schunk and Nagy, 2004)) as:

$$\kappa_c = \sum_{i=O,O_2,N_2} [\frac{N_i}{N_{total}}] A_i T^s \tag{3.4}$$

where N_i/N_{total} is a weighting factor by number density of each neutral species, T is the thermosphere temperature, A_i and s are species specific thermal conductivity coefficients to fit the total conductivity as needed. The summation includes the three species with the largest concentrations in the thermosphere. From Figure 3.1, above about 200 km, O is a dominant neutral species whereas in the lower thermosphere O_2 and N_2 densities are more prevalent and must be considered in the contribution to the heat exchange process. The temperature profile shows that above about 250 km, the atmosphere is roughly isothermal, so the conduction term can be quite small. This is the region where O is dominant. This implies that the N_2 term in the thermal conductivity is probably a more important term since N_2 is dominant below $\sim$250 km where the vertical temperature gradient is largest.

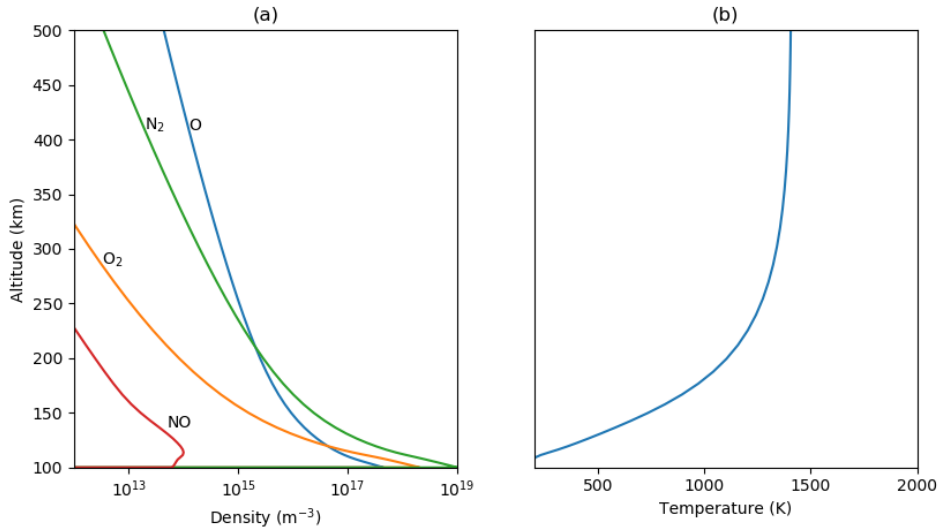

Figure 3.1: (a) Globally averaged atmosphere constituents and (b) globally averaged temperature in the thermosphere from GITM on September 26th, 2002. This time period is representative of solar max conditions ($F_{10.7} \approx 180$) and is used in some of the tests performed in later sections.

Pavlov (2017) gives approximations from tabulated values in Vargaftik et al. (1993) for thermal conduction (denoted as λ in Pavlov (2017)) experiencing pressures much less than 0.1 MPa in temperature ranges of 160 - 2500 K for N_2 and 160 - 1500 K for O_2. The full expressions a

$$\kappa_{N_2} = -3520 + 720.5T^{0.5} - 41.93T + 1.613T^{1.5} - 0.02685T^2 + 1.665 \times 10^{-4}T^{2.5} \tag{3.5}$$

$$\kappa_{O_2} = -3169 + 735.7T^{0.5} - 53.83T + 2.583T^{1.5} - 0.05325T^2 + 4.083 \times 10^{-4}T^{2.5} \tag{3.6}$$

$$\kappa_O = 46.7(1 + 2.228 \times 10^{-5}T - 5.545 \times 10^{-9}T^2)T^{0.77} \tag{3.7}$$

Figure 3.2 shows the Pavlov (2017) values of κ_{N_2}, κ_{O_2}, κ_O, as well as the corresponding Schunk and Nagy (2004) conductivities (assuming s = 0.75). In the bottom subplot, "best fit" lines are shown using the same parameterization scheme in (4). The estimation of the coefficients and exponent in the parameterization are derived from data and theoretical expressions of the thermal conductivity of individual gases from (Hilsenrath, 1960), (Reid et al., 1977), (Lide, 1997), (Barlier et al., 1969) and (Banks and Kockarts, 1973). While Vargaftik et al. (1993) describes more complex expressions that best fit to an exponent close to 0.8. Although the parameterizations of the atomic oxygen, O, and nitrogen, N_2, seem to match fairly well, there is a great deal of discrepancy for the estimation of the O_2.

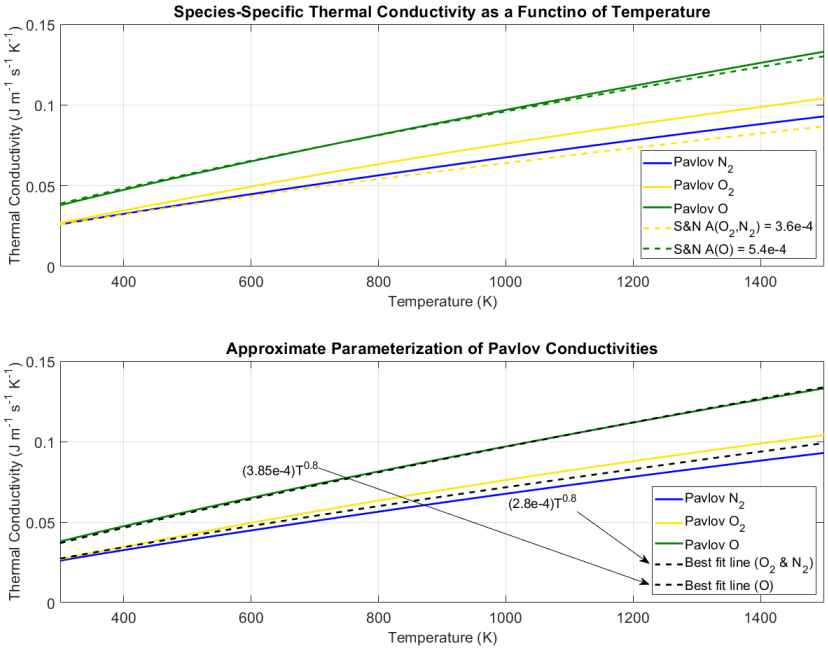

Figure 3.2: Different species-specific thermal conductivities plotted as a function of temperature with differing definitions of the suggested parameterization. Top: Pavlov and Schunk and Nagy parameterized species-specific conductivities. Bottom: Best fit lines for the Pavlov species-specific curves with the form $A_i T^s$.

As described in Pawlowski and Ridley (2009), model bias can originate from incorrectly defined parameters like the thermal conductivity, eddy diffusion, or photoelectron heating efficiencies. Certain quantities such as the eddy diffusion, and lower boundary density and temperature affect model bias such that the best modeled physics equations can still result in inaccurate mass density calculations. It is therefore quite difficult to identify the cause of data-model comparison discrepancies.

For example, Masutti et al. (2016) explored a time period in which F10.7 increased over the course of several days and showed that GITM's mass density at approximately 400 km altitude overresponded to this change. Overall, there was an underestimate of a mass density when F10.7 was low and an overestimate when F10.7 was high. Since GITM's performance was a function of the solar irradiance, improved performance could possibly be captured through thermal conductivity adjustments based on solar activity, but may be possibly masking other incorrectly modeled physics.

The thermal conductivity is the focus of this study because its parameterization is a possible deficiency in GITM and it significantly changes the density results needed for orbit prediction. This is an opportunity to settle the discrepancy of parameterizations and compensate for neutral

density model bias that may be caused by other incorrectly modeled physics, boundary conditions or drivers. For instance, inaccurate modeling of a term like the eddy diffusion coefficient could also influence neutral density results (Qian et al., 2009). Handling the eddy diffusion has been a topic of previous research in GITM ((Goel et al., 2018), (Malhotra et al., 2017)), but the eddy diffusion is a term that also controls the composition and ionospheric density due to the changed turbulent mixing and its inclusion in the continuity, vertical momentum and energy equations.

3.1.3 Manually Debiasing the Thermal Conductivity

This section outlines the need for debiasing models by describing an attempt to choose a single constant, thermal conductivity coefficient that allows GITM's mass density to better match CHAMP observations. Nine runs with varying thermal conductivity coefficients (Table 5.1) were performed. Six different contour maps are shown for the six different time periods simulated (Figure 3.3). For each run, the eddy diffusion coefficient was set to 500, and s was set to 0.69. The percent difference in mass density from CHAMP measurements and GITM calculations were examined. GITM was ran for ten days, but only the last five days of each run were used to allow GITM to reach a quasi-diurnally reproducible state before comparison. CHAMP and GITM densities were averaged over the orbital period ($\sim$ 90 minutes).

Contours of percent error for each time period are shown in Figure 3.3. The September 2002 and September 2004 time periods were selected to tune GITM, keeping the season and geomagnetic conditions similar, but allowing the solar activity to vary (see Table 3.2).

Run	$\mathbf{A(O_2, N_2)}$	$\mathbf{A(O)}$
1	3.6	4.6
2	4.6	4.6
3	5.6	4.6
4	3.6	5.6
5	4.6	5.6
6	5.6	5.6
7	3.6	6.6
8	4.6	6.6
9	5.6	6.6

Table 3.1: The variety of inputs to thermal conductivity coefficients. Multiply $A(i)$ by 10^{-4} to yield $Jm^{-1}s^{-1}K^{-1}$.

Time period	F10.7
September 2002	146-196
February 2003	107-133
September 2004	89-110
August 2005	85-110
October 2005	74-80
September 2006	70-81

Table 3.2: Range of F10.7 (solar flux units) values during the different time periods.

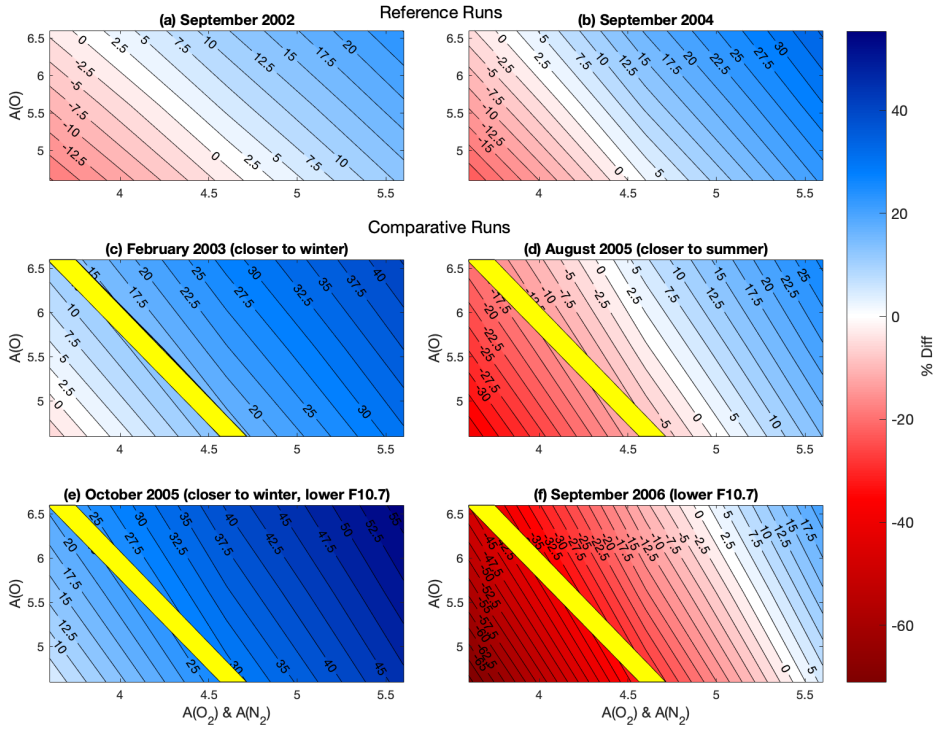

Figure 3.3: Contours of model errors as a function of thermal conductivity (molecular on x-axis, atomic on y-axis) for different time periods. The blue and red regions indicate GITM having mass densities lower and higher than CHAMP observed, respectively. Areas of white yield results similar mean densities to CHAMP. (a) and (b) are baseline runs to find suitable thermal conductivity coefficients. The yellow region in (c)-(f) are thermal conduction values that yield good results for both the reference runs to within 5%.

As the thermal conductivity is increased, the gradient in temperature in the lower thermosphere decreases. Since the lower boundary condition fixes the temperature, the temperature in the upper thermosphere must decrease. Pressure and density profiles are strongly controlled by the temper-

ature, so as the temperature decreases, the density at a fixed altitude in the upper thermosphere also decreases. This means that the neutral density in GITM decreases as the thermal conductivity increases. Figure 3.3 shows that the molecular coefficient has a stronger effect than the atomic oxygen coefficient. This is because the thermal conductivity multiplies ∇T, which is largest in the lower thermosphere ($\sim$100-200 km), where the major species O_2 and N_2 are dominant (Figure 3.1). Hence, the thermal conductivity in the lower thermosphere dictates the middle and upper thermosphere temperature and density.

The top two plots of Figure 3.3 indicate that, for these two intervals, there is a span of atomic and molecular coefficients that reduce the model bias to extremely low levels, even with different solar irradiance. However, when the study was expanded to include other seasons and other conditions, it became clear that no combination reduced the bias universally. Times outside of September 2002 and 2004 needed to be considered to see that this overlapping parameterization space does not provide unbiased results at different parts of the solar cycle. The yellow zone overlayed on each subplot is the parameter space from the September 2002 and 2004 runs where the error was within $\pm 5\%$ for both times. These yellow zones show that a debiased set of thermal conductivity parameters for one set of times do not necessarily reduce the error to zero for other time periods.

Figure 3.4 shows the sensitivity of the thermal conductivity exponent, s, for September 16-26th, 2002. The molecular and diatomic coefficients were held constant at A(O) = A(O_2, N_2) = 4.6×10^{-4} $Jm^{-1}s^{-1}K^{-1}$ while 's' varied from 0.63 - 0.75 in increments of 0.03. For the GITM conditions during this time period, an exponent of 0.68 minimized the absolute error between GITM and CHAMP. As indicated in the sensitivity study of the molecular and diatomic coefficients, this is not expected to be a universal value due to the uncertainty in other terms within GITM. These runs show that GITM is more sensitive to the exponent than the molecular and diatomic coefficients (i.e. a small percentage change in s drives a large change in GITM densities). For this reason, the work in the next sections focus on estimating the thermal conductivity exponent, s.

The causes of model bias varying from event to event in Figure 3.3 could stem from incorrect drivers (EUV, lower boundary condition, aurora, etc...) or incorrect physics (ion variability, small-scale structures, turbulent heating, etc...). This is the reason an automated debiasing mechanism is needed. The difference in performance to estimate other state variables (aside from the neutral density) between the three parameters within the thermal conductivity coefficient was not studied in this work.

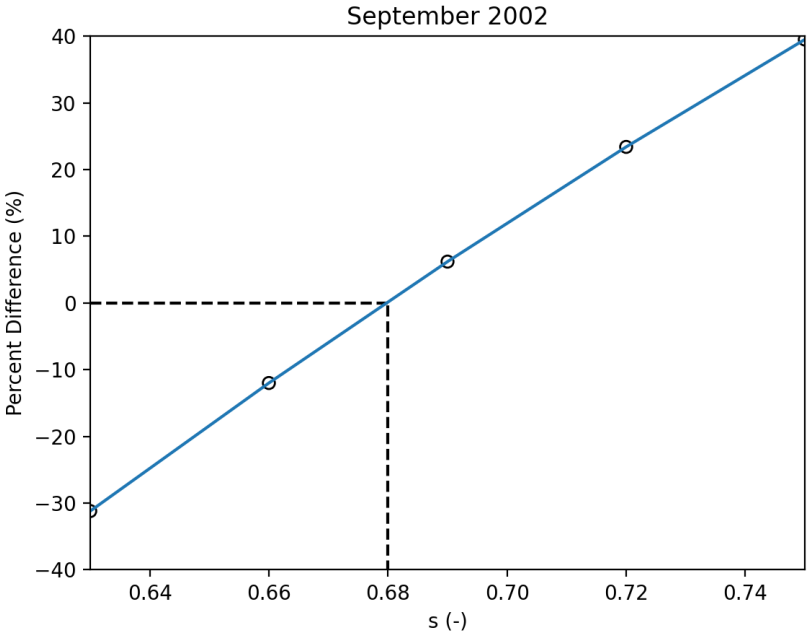

Figure 3.4: A five-run sensitivity study for the thermal conductivity exponent, s, which varied from 0.63 - 0.75. Percent differences between GITM and CHAMP are shown for each run.

3.2 Retrospective Cost Model Refinement (RCMR)

Retrospective Cost Model Refinement (RCMR) is a technique developed for parameter estimation in nonlinear systems (Morozov et al., 2011). The technique is a variation of retrospective cost adaptive control (RCAC) that was primarily developed for adaptive control applications in aerospace engineering (Santillo and Bernstein, 2010). In this work, RCMR is used to estimate thermal conductivity coefficients in a system modeled by Navier-Stokes partial differential equations. RCMR minimizes a cumulative cost function that is based on the difference between the density computed self-consistently by GITM and the density specified externally, such as that measured by a real satellite or estimated by a different model. This technique has been applied for estimation of (1) the eddy diffusion coefficient using total electron content (TEC) as the comparison variable (Goel et al., 2018), (2) NOx cooling using simulated space-based measurements (D'Amato et al., 2013), (3) the photoelectron heating coefficient based on real satellite measurements (Burrell et al., 2015) and, (4) the thermal conductivity coefficients using simulated density measurements (Goel et al., 2020). Each of these studies successfully estimated the corresponding unknown parameter using RCMR. This method is different from the other data assimilation methods talked about in the introduction because it does not use an ensemble (Matsuo et al., 2013) or run restarts (Sutton, 2018)

which saves considerably on computational time. RCMR has been applied to parameters within GITM rather than directly updating the model states or modifying the drivers. For a more complete description of RCMR, refer to Goel et al. (2020).

Figure 3.5 shows the block diagram used to estimate the unknown parameter within RCMR. As shown by the top block in Figure 3.5, the external drivers, including the solar EUV, frictional heating and auroral precipitation, force the real thermosphere's density, ρ. Thermal conductivity serves to move the energy vertically. When trying to reproduce nature's physics with a model (GITM), there are assumptions that try to emulate the true relationships. The empirical formulations, boundary conditions and other model necessities result in error accumulation. This is seen when comparing the model estimated density, $\hat{\rho}$ with in-situ measurements, as shown in Figure 3.3.

Reducing the error (z) is ideally done by correctly implementing equations that accurately and completely capture all dynamics, boundary conditions and drivers within the model. Low error could also be obtained by incorrect physics within the models that cancel each other out, inadvertently matching the measurements. This can occur when multiple incomplete physics terms compensate for each other. For example, having too low solar EUV heating along with too high frictional heating at high-latitudes could result in an orbit-averaged mass density that is more or less correct. In the case of RCMR, intentionally adjusting thermal conductivity coefficient(s) changes the error by altering the thermal balance between sources and sinks.

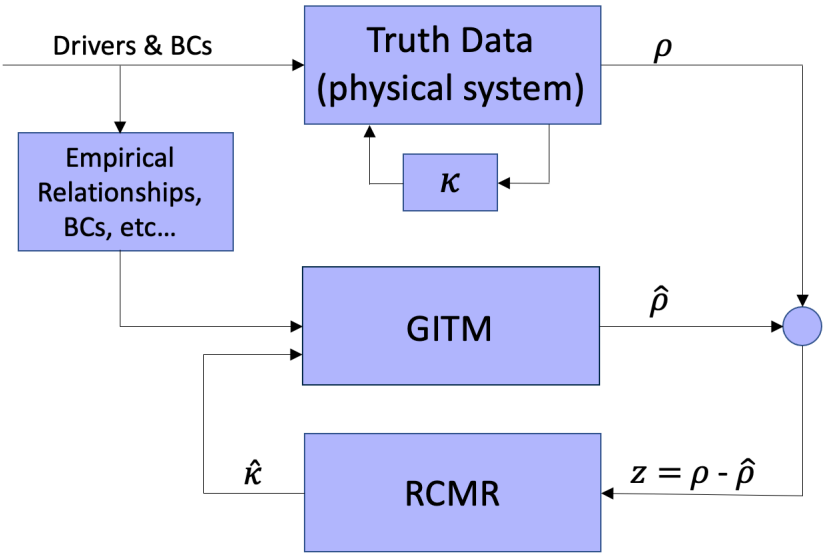

Figure 3.5: Modified block diagram from Goel et al. (2020) to illustrate the RCMR process.

In Figure 3.5, the top block represents the true physical system with real drivers and boundary

conditions. In the real system, κ is driven by the states and dynamics, making a complex, nonlinear system. GITM approximates the drivers and boundary conditions as well as approximating the dependence of κ on the system state as described above (i.e. $\kappa = \sum A_i T^s$). RCMR takes the difference between the "actual" ρ and the GITM-estimated $\hat{\rho}$, and alters the κ (through the values of A_i and/or s) to minimize the difference.

In order to validate the integration of RCMR within GITM, RCMR was used to estimate κ ($A(O_2, N_2)$) using simulated truth density data obtained from a GITM simulation with a known value of κ. The density data was recorded and serves as the satellite measurements. Next, GITM was re-run with an intentionally incorrect $A(O_2, N_2)$ and RCMR updated the estimate $A(O_2, N_2)$ using the simulated truth density data. If RCMR was implemented correctly, RCMR's estimated $A(O_2, N_2)$ would converge to the true value of $A(O_2, N_2)$ used to generate the simulated truth data, validating the technique. When this is true, it is a good indication that when actual truth data (i.e. CHAMP, GRACE, MSIS) is used, the convergence will provide the real thermosphere thermal conductivity coefficients.

3.3 Results

3.3.1 Automating the Model Debiasing Process via RCMR

RCMR estimates the thermal conductivity coefficients every 60 seconds using density measurements from the CHAMP and GRACE satellites as well as Naval Research Laboratory's (NRL) Mass Spectrometer and Incoherent Scatter Radar (MSIS) empirical model (Picone et al., 2002). In order to implement this, GITM was ran independent of RCMR to obtain global density values from September 16-26, 2002 forming a truth data set. The thermal conductivity coefficients of A(O) = 4.6×10^{-4} $\mathrm{Jm^{-1}s^{-1}K^{-1}}$, A($O_2$, N_2) = 4.6×10^{-4} $\mathrm{Jm^{-1}s^{-1}K^{-1}}$ and the exponent s = 0.69 were used. In comparison to CHAMP satellite data, this provided a low-biased mass density result (Figure 3a).

The orbit of the CHAMP satellite was used to extract densities from the GITM run ($\rho_{4.6}$) at a one minute cadence to match the update frequency of RCMR. Using GITM densities at the satellite-position as inputs for RCMR (see Figure 3.6), a GITM simulation was run again during the same time, but used RCMR to change the molecular coefficient. This work was different from Goel et al. (2020) which used the simulated global maximum, minimum and mean densities instead of the densities directly at the satellite position. The thermal conductivity coefficient $A(O_2, N_2)$ was initialized to 1.0×10^{-4} $\mathrm{Jm^{-1}s^{-1}K^{-1}}$, while the A(O) and exponent S were held constant at their previously set values above. The densities modeled by GITM with RCMR is denoted as ρ_{RCMR}. RCMR used the $\rho_{4.6}$ data and ρ_{RCMR} data to compute an error (z) to update the thermal

conductivity estimation while the simulation progressed. Figure 3.6 shows two RCMR simulations that demonstrate that the independent dynamic adjustments of $A(O_2, N_2)$ and s in RCMR debias GITM. In the left column, the error z decreased to zero, while $A(O_2, N_2)$ converged to 4.6×10^{-4} $\mathrm{Jm^{-1}s^{-1}K^{-1}}$ after around three days. The right column shows the same simulation where s was the free parameter for RCMR to estimate. It is expected that s would converge to 0.69 to match the thermal conductivity exponent used to generate the truth data. Instead, RCMR estimated a value closer to 0.72 which is due to different versions of GITM being used for the truth data run and that of the most recent RCMR run. From here forward, RCMR only updates s due to GITM's sensitivity to this parameter.

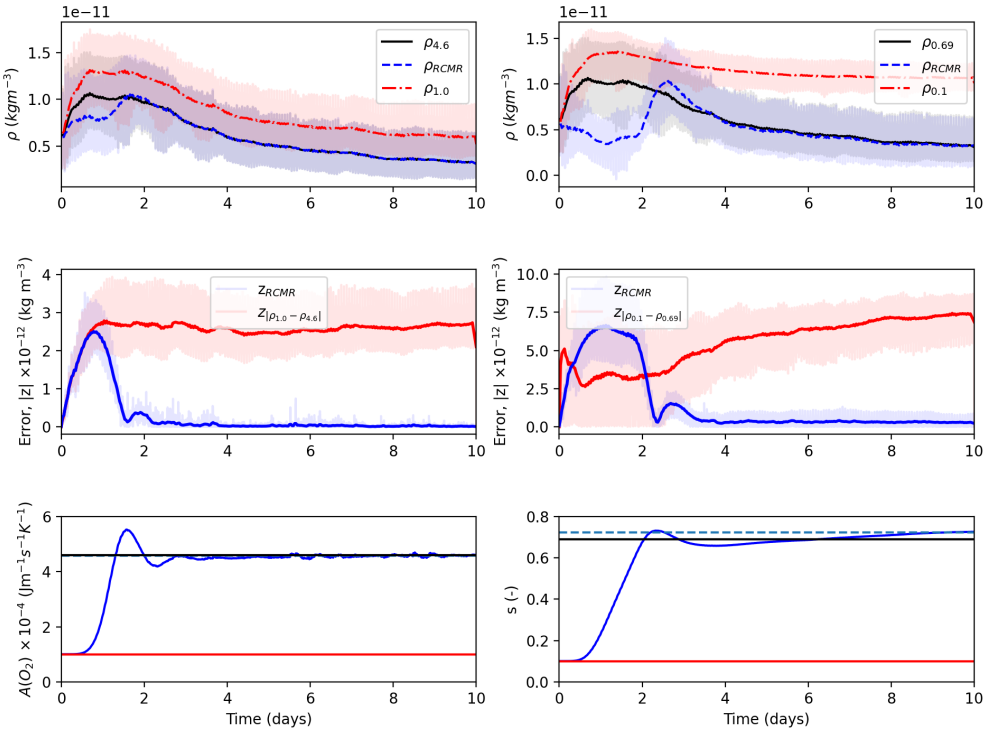

Figure 3.6: Top row: Densities along the CHAMP orbit are shown with three different values of A_{O_2} or s. Raw values are shown as transparent lines, while orbit averaged values are shown as bold. The error (middle row) and thermal conductivity coefficient (bottom row) from using simulation data at CHAMP locations at a one minute cadence is shown in blue for the RCMR assisted run, red for a constant, purposefully-biased, constant parameterization, and black for a constant parameterization matching the truth data parameters. The orbit averaged errors are shown with a thicker line of their corresponding color.

In addition to the truth data and RCMR-adjusted mass densities, the density and error is shown

when the incorrect parameterization was used and not corrected. This provides a quantification of the level of improvement that can be gained using RCMR.

This example shows that RCMR can correct for an incorrectly set thermal coefficient, but model bias can be caused by a variety of issues, as described above. For a second example of idealized RCMR runs, illustrated in Figure 3.7, GITM was run with consistent thermal conductivity parameters but incorrect drivers.

F10.7, the daily solar flux at wavelength 10.7 cm, is a proxy for solar spectra (Richards et al., 1994). An alternative to the F10.7 proxy is using FISM to describe the spectrum (Chamberlin et al., 2008). Near real time and for predictions, F10.7 is approximate and one of the only ways to describe the solar spectrum. If F10.7 is not right or does not describe the spectrum correctly, model bias could result. This second test explores whether RCMR can compensate for an incorrect specification of the F10.7. The RCMR estimated parameter for this run and future runs was the exponent s, with an initial value of s as 0.1.

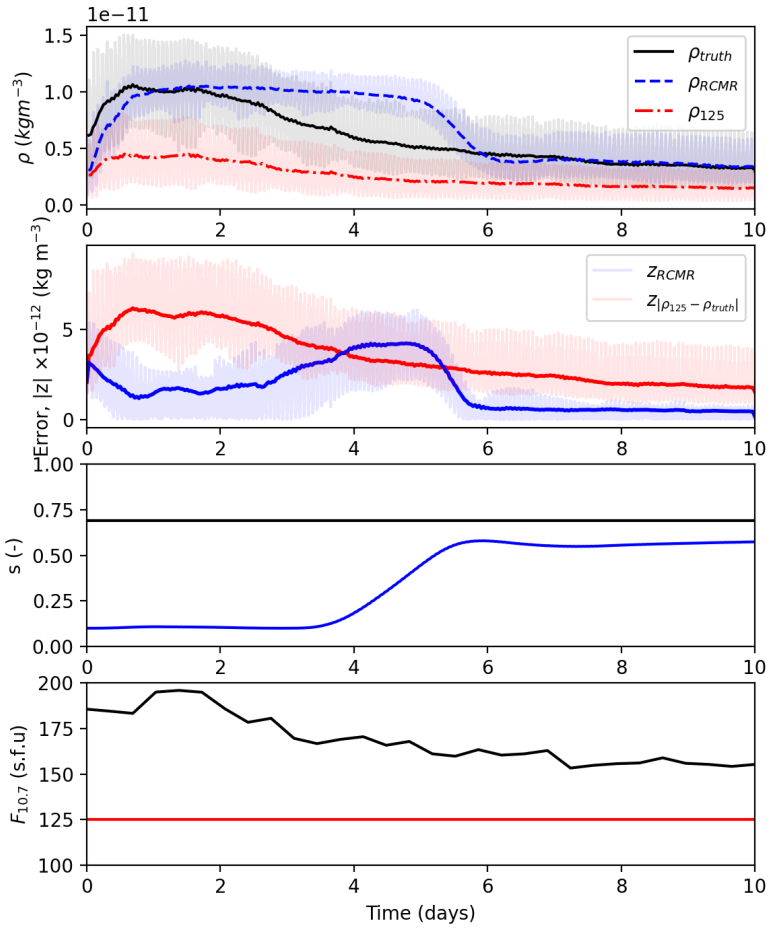

Figure 3.7: Densities and errors are shown with three different run conditions: (1) the truth data used as input for RCMR in black, (2) the RCMR run dynamically debiasing GITM with incorrect solar drivers in blue, and (3) the case where GITM has incorrect solar drivers and is not implementing RCMR in red. The orbit averaged errors are shown with a thicker line of their corresponding color. The third subplot shows the thermal conductivity exponent over time. The bottom subplot shows the corresponding F10.7 used in each run. The blue line corresponding to the F10.7 for the RCMR run is overlapping with the red line corresponding to the biased run since they were both run with the same incorrect F10.7.

Similarly to the previous run, the truth data being used was an extraction of GITM results where the F10.7 was updated based on the actual F10.7, which varied from 190 to 150 solar flux units. The RCMR run was intentionally run with an incorrect constant F10.7 of 125 solar flux units. Over time, the RCMR-debiased run converged to the truth data and the error decreased dramatically. The time it took to converge was longer than the first test by roughly two days. This was due to the

densities being similar between the two runs for the first two days despite the very different run settings. In this case, a low F10.7 incorrect driver caused a low density, having a negative bias. At the same time, a low initial value of s caused a high density since the thermal conduction would be reduced leading to a high temperature. In this case, a positive bias would result. In combination, the biases mostly cancelled and RCMR was relatively ineffective for the first two days. After this, RCMR was able to track the error and produced an 's' that adequately compensated for the incorrect specification of F10.7.

3.3.2 RCMR with CHAMP and GRACE Satellite Densities

In the previous section, the simulated densities generated from a GITM run represented the "true" thermosphere. In this section, tests of RCMR with real satellite data are described. Initial tests were done using data from September of the years 2002 and 2004 as sample months for high and moderate F10.7 fluxes, respectively, since these were used for manual debiasing earlier in the study. Both time periods had relatively low levels of activity, with $|D_{st}|$ being less than 50 nT during each time period.

Satellite	**Sept. 2002 Altitude (km)**	**Sept. 2004 Altitude (km)**	**Inclination** ($^\circ$)
CHAMP	390-450	370-410	87.3
GRACE	485-515	460-505	89.0

Table 3.3: Information on the altitude and orbit inclination during the two test periods.

The estimation of the thermal conductivity exponent s was explored using CHAMP and GRACE individually. Figures 3.8 and 3.9 show the September 16-26, 2002 period comparing the results of GITM with a constant thermal conductivity to the RCMR adjusted values against the satellite observations.

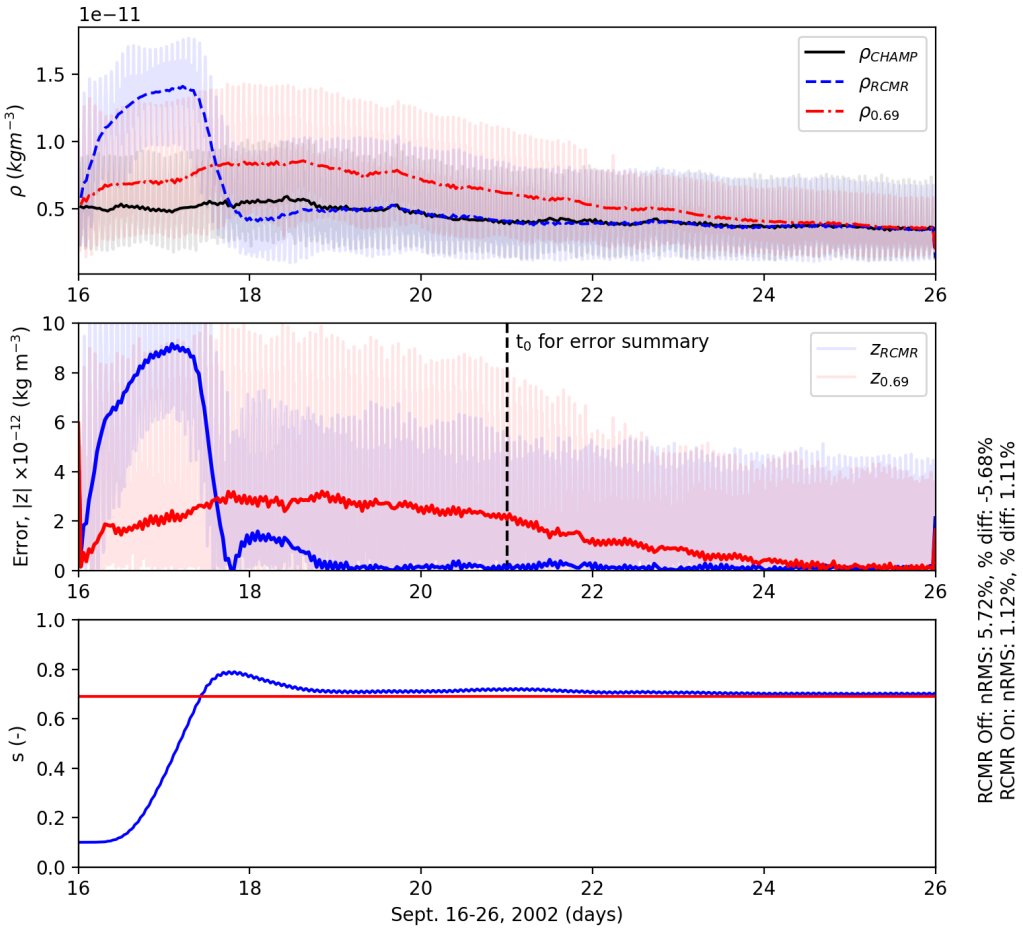

Figure 3.8: The top subplot shows the raw and orbit averaged densities are shown for GITM, CHAMP and RCMR. In the middle subplot, the errors are plotted over one another to observe how RCMR compares to a constant thermal conductivity typically used in GITM. The bottom subplot shows the consequent thermal conductivity exponent estimated in blue. In red is the constant value used when RCMR was not applied. The local time of ascending node for CHAMP was 13.4 LT.

The RCMR and non-RCMR runs both converge to the CHAMP and GRACE measurements. With RCMR, the convergence is much faster with large improvements in mass density after around two to three days. As observed in Figures 3.8 and 3.9, the free parameter s converged to 0.70 which is similar to the constant value of 0.69 used in a typical GITM run. This set of thermal conductivity coefficients (4.6e-4, 4.6e-4, 0.69) matched the results found in the manual debiasing process.

Normalized root mean square (nRMS) and percent error are shown on the bottom right of Figures 3.8 and 3.9 to quantify the improvement with RCMR. These values were computed based

on orbit-averaged densities for the final five days of the run (marked as t_0 on the figure). This gave sufficient time for RCMR to debias the model and allow GITM to reach a roughly diurnally reproducible state. In Figure 3.9, the nRMS and percent difference show improvement of $\pm 33\%$ percent error and nRMS to less than 3%.

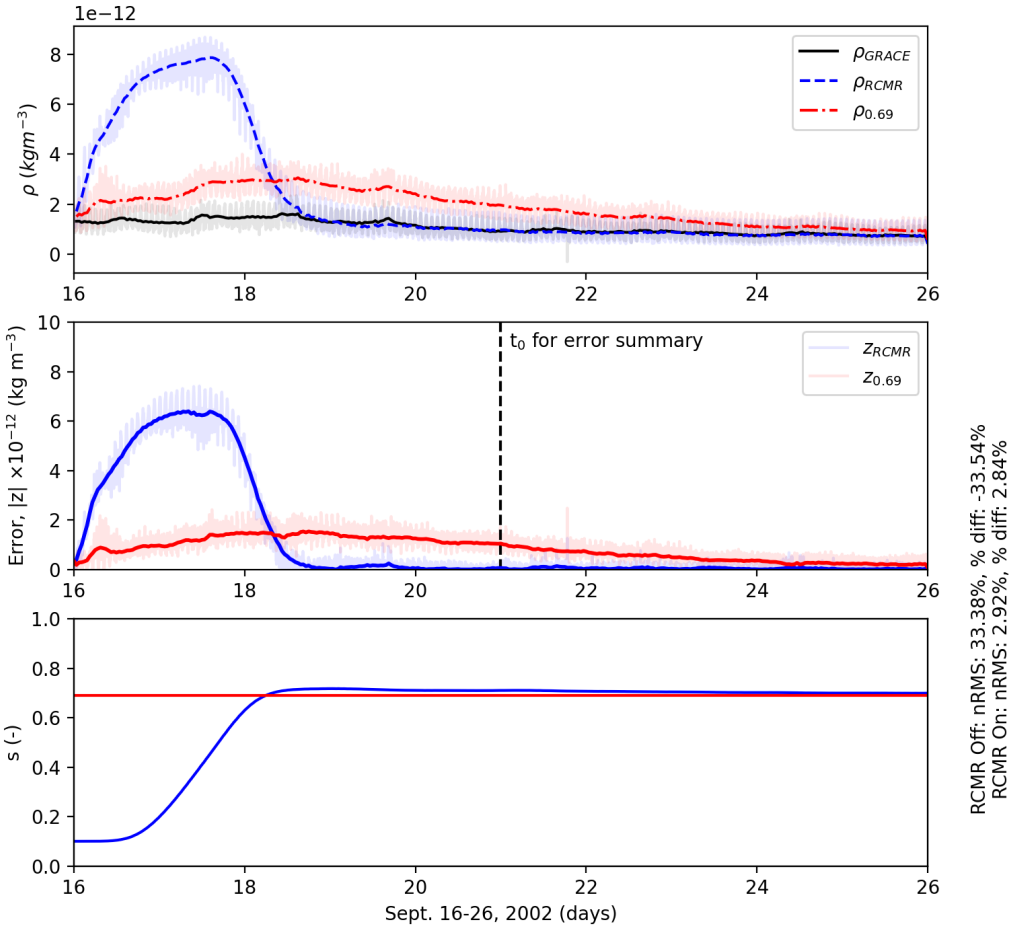

Figure 3.9: Same as Figure 3.8, except using GRACE instead of CHAMP. The local time of ascending node for GRACE was 21.7 LT.

Switching to the time period in 2004, a similar simulation was performed using CHAMP data to check the robustness of RCMR under different solar conditions. The F10.7 was considerably lower for this run mostly being between 90-110 $\mathrm{Wm^{-2}Hz^{-1}}$, while the seasonality and geomagnetic activity was similar. Recall that debiasing between September 2002 and 2004 was possible with similar thermal conductivity coefficients, and so running this time period gave RCMR the

opportunity to demonstrate this. As shown in Figure 3.10, the RCMR and non-RCMR mass densities converged to CHAMP measurements with RCMR reducing the time to converge by nearly seven days. In the bottom subplot, the estimated thermal conductivity exponent converges to right around 0.70 which is consistent with the RCMR test performed in 2002 and the manual debiased simulations. nRMS and percent error were used to quantify the improvement with RCMR. They showed a much larger improvement from a roughly -20% percent error and nRMS to less than 5%.

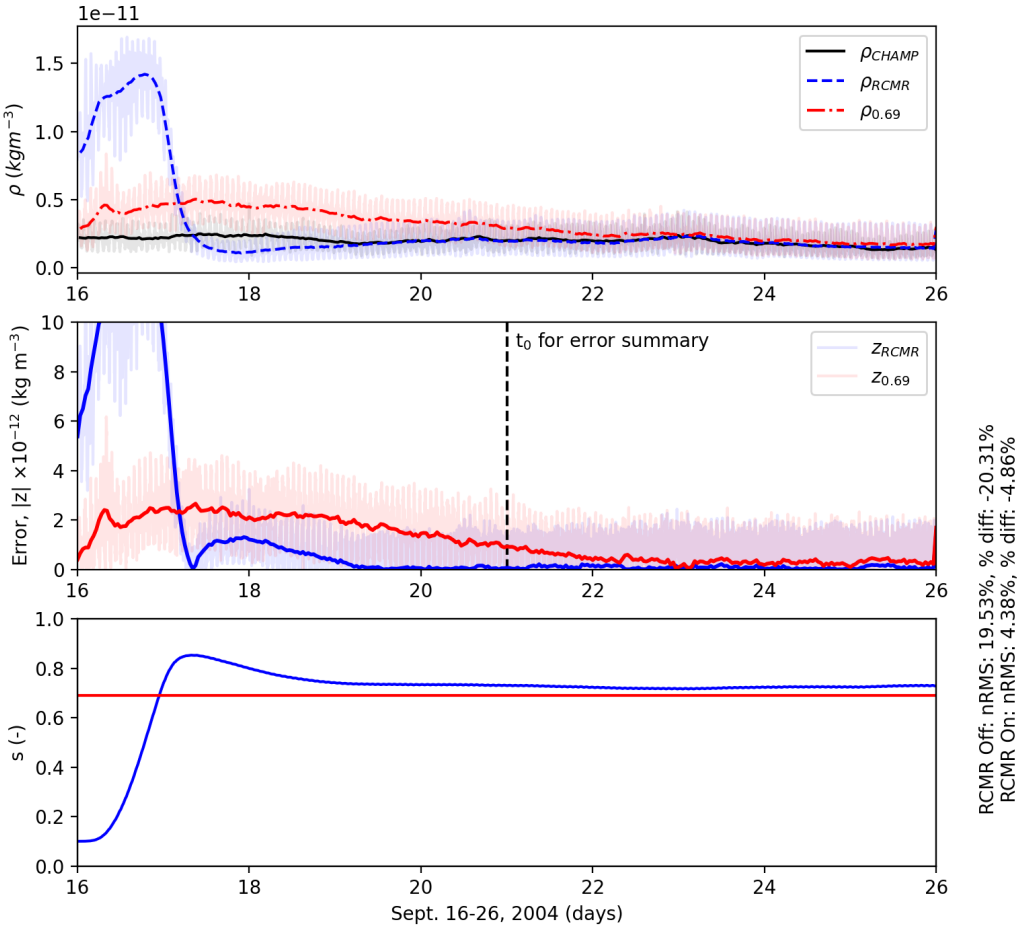

Figure 3.10: Same as Figure 3.8, except for September 2004. The local time of ascending node for CHAMP was 19.4 LT.

3.3.3 Storm-time Debiasing and Forecasting

In this section, GITM was debiased by RCMR before the storm in August 2005. The F10.7 for this time period was lower than the previous runs shown. It varied between 70-100 $Wm^{-2}Hz^{-1}$. Comparisons between the typical GITM run, a purposefully biased GITM run, an RCMR-assisted GITM run with purposefully biased F10.7, and CHAMP data were made in an effort to improve forecasting of density enhancements during and after the storm. Figure 3.11 shows the interplanetary magnetic field (IMF), solar wind velocity, hemispheric power, and Dst prior to and through the storm on August 24-25th, 2005. During the quiet time, the Dst never went below $\sim$-25 nT, while the hemispheric power was quite low most of the time. On August 24th, the IMF B_z turned negative as well as the solar wind speed increasing dramatically. This drove a large increase in the aurora and a significant development of the ring current as indicated by the nearly -200 nT Dst.

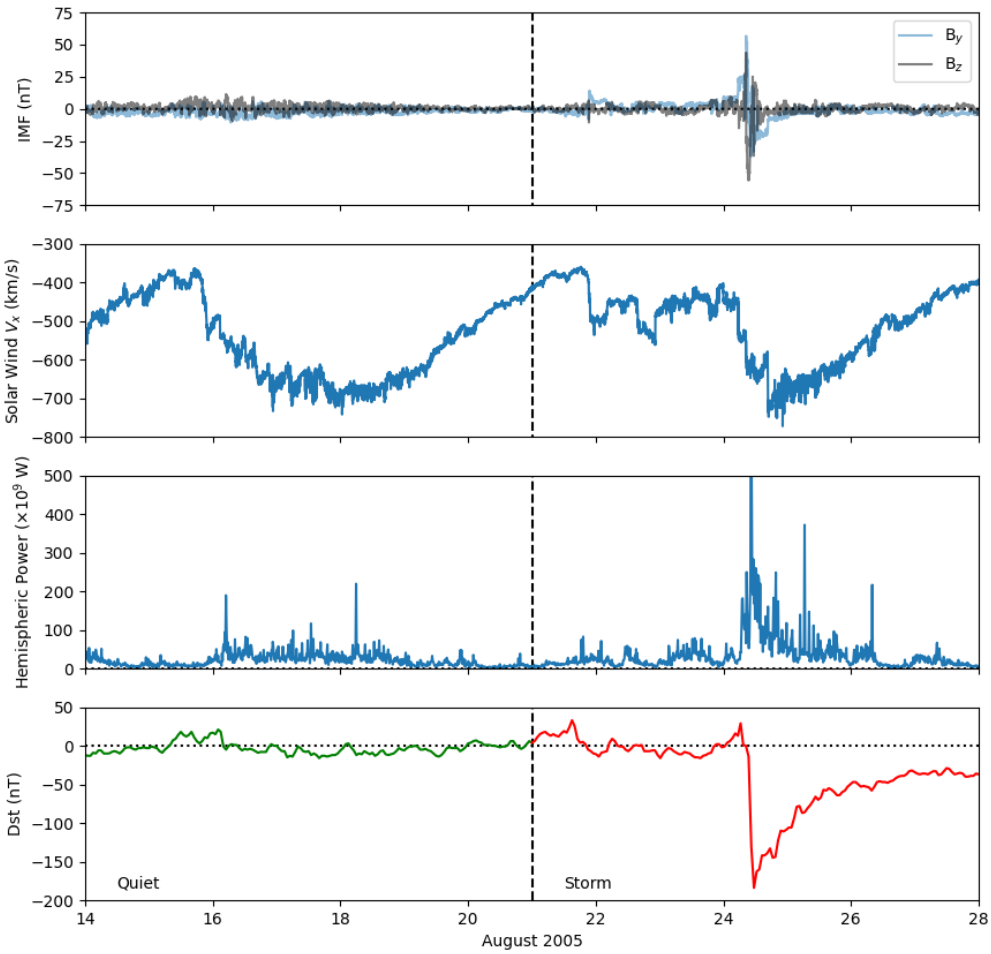

Figure 3.11: Interplanetary magnetic field (IMF), solar wind velocity, hemispheric power and Dst measurements from August 14th-28th, 2005. In the Dst panel, the green portion indicates the quiet time period before the storm, while the red indicates the active storm period.

The storm took place between August 24-26, 2005. In the RCMR run, the debiasing took place from August 14-21. The run continued through the storm from August 21-28 without the assistance of RCMR. During the storm, the exponent 's' was held constant at its last value specified by RCMR on August 21. In Figure 3.12, the debiasing was done prior to the storm using CHAMP measurements. As was done before, the densities, errors and dynamic thermal conductivity exponenent are shown in comparison to the static runs.

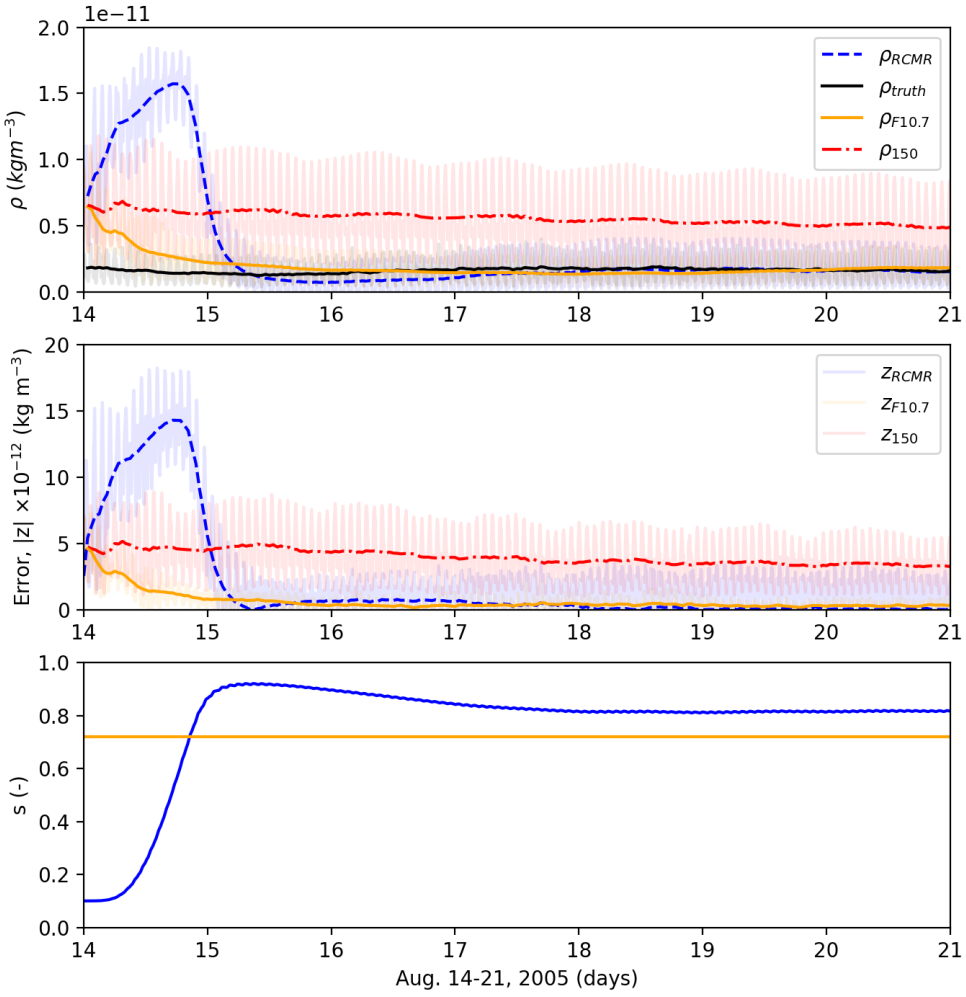

Figure 3.12: The densities and errors compared to CHAMP during August 2005 with RCMR on (blue) and RCMR off in two conditions. One run is with the daily averaged F10.7 values included (orange) and the other is with a constant, incorrect F10.7 of 150 (red). Both of the non-RCMR runs have the same constant thermal conductivity exponent, but only one of them is shown. The RCMR run is done with the incorrect F10.7. The bottom subplot shows the consequent thermal conductivity coefficient estimated.

As expected, the biased run with a constant F10.7 of 150 $\mathrm{Wm^{-2}Hz^{-1}}$ was very different than the CHAMP measurements and a GITM run using real F10.7 measurements. It is important to point out that the parameter estimation from RCMR showed that the best exponent s was around 0.8 which was considerably larger than the other runs. The F10.7 of 150 $\mathrm{Wm^{-2}Hz^{-1}}$ is higher than the true conditions artificially increasing mass densities. To counteract this, an increased thermal

conductivity was needed to dissipate this excess energy, reducing the mass density.

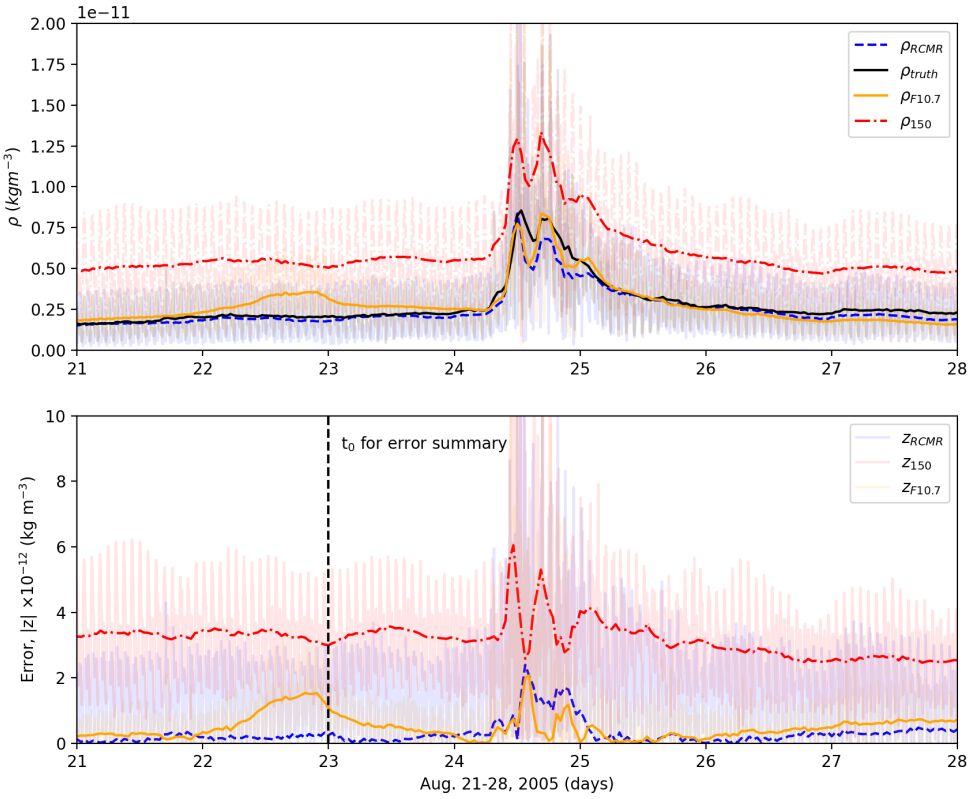

Figure 3.13: Similar to the previous figure, but for the August 21st-28th, 2005. RCMR is turned off so no thermal conductivities are being shown.

Figure 3.13 shows the runs proceeding through the storm and storm recovery. For the three days after RCMR was turned off, the densities stayed debiased. The storm was better represented because of this, although GITM with RCMR under predicted the storm response during the peaks. This is most likely due to the increased thermal conductivity, which pulled energy out of the thermosphere too quickly during the storms. This is relatively minor compared to the biased model results though. The RCMR run matched the recovery density after the storm quite well. Additional performance assessment metrics are shown in Table 3.4. The formulations for each metric is shown in Kalafatoglu Eyiguler et al. (2019). When comparing the RCMR run to the biased run, the RCMR run performed better in every metric. Each of these statistics help quantify the improvements that can be had to the mean and variability of the mass densities.

On the other hand, the calibrated model of GITM also performed better than the biased run. Comparing the RCMR run and the calibrated model of GITM, the Ratio_{avg} of the default GITM

simulation performed better than the RCMR run. RCMR was capable of improving the time delay (TD) of the storm peak, the mean average error (MAE) and normalized root mean square error (NRMSE).

3.3.4 Debiasing using an Empirical Model

Satellite measurements of the thermosphere are not always available, especially during real-time operations. For this reason, an empirical model such as MSIS may be useful as a source of ”truth data”. Whereas empirical models are not always skilled at correctly predicting highly perturbed events, like solar storms, they are useful for obtaining information on the background state. Further, satellite orbits may not be ideally placed to represent the global conditions, while an empirical model can be sampled anywhere (or everywhere). While satellite data is the ideal choice for debiasing, using an empirical model may help in some situations. For these reasons, a final test was run to attempt to debias GITM under conditions where satellite data was (in theory) not available.

In this run, MSIS mass densities at the subsolar point at 400 km altitude were used as the source of ”truth data”. The same time period in August 2005 was used for this. RCMR was allowed to debias GITM for seven days and then proceed through the storm. During the storm, RCMR was turned off and the storm-time performance evaluation of GITM was checked against CHAMP data, as in the previous case.

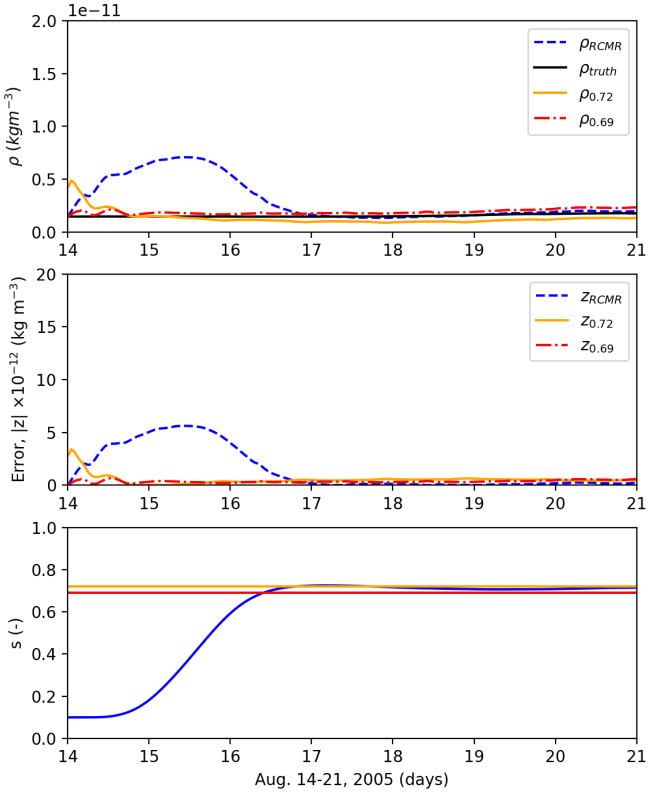

Figure 3.14: The densities and errors compared to MSIS at the 400 km altitude sub-solar point during August 2005 with RCMR on (blue) and RCMR off in two conditions. One run is with manually calibrated thermal conductivity values included (orange) and the other is with a constant, biased thermal conductivity exponent of 0.69 (red). The bottom subplot shows the consequent thermal conductivity coefficient estimated.

In Figure 3.14 shows the mass density for different runs at the subsolar point at 400 km altitude, which is where the MSIS data was extracted. The biased run (labeled $\rho_{0.69}$) and RCMR run no longer had error induced by the F10.7. The only source of error in the RCMR run (ρ_{RCMR}) was the initial value of 0.1 given to the thermal conductivity exponent s. The thermal conductivity exponent s in the wrong tuning run was 0.69, whereas the best tuning had an exponent of 0.72 ($\rho_{0.72}$). At the 400 km, subsolar point each run converged to MSIS results within a few days of the run. As shown in the bottom subplot, RCMR estimated the 's' to be 0.71, using the MSIS results.

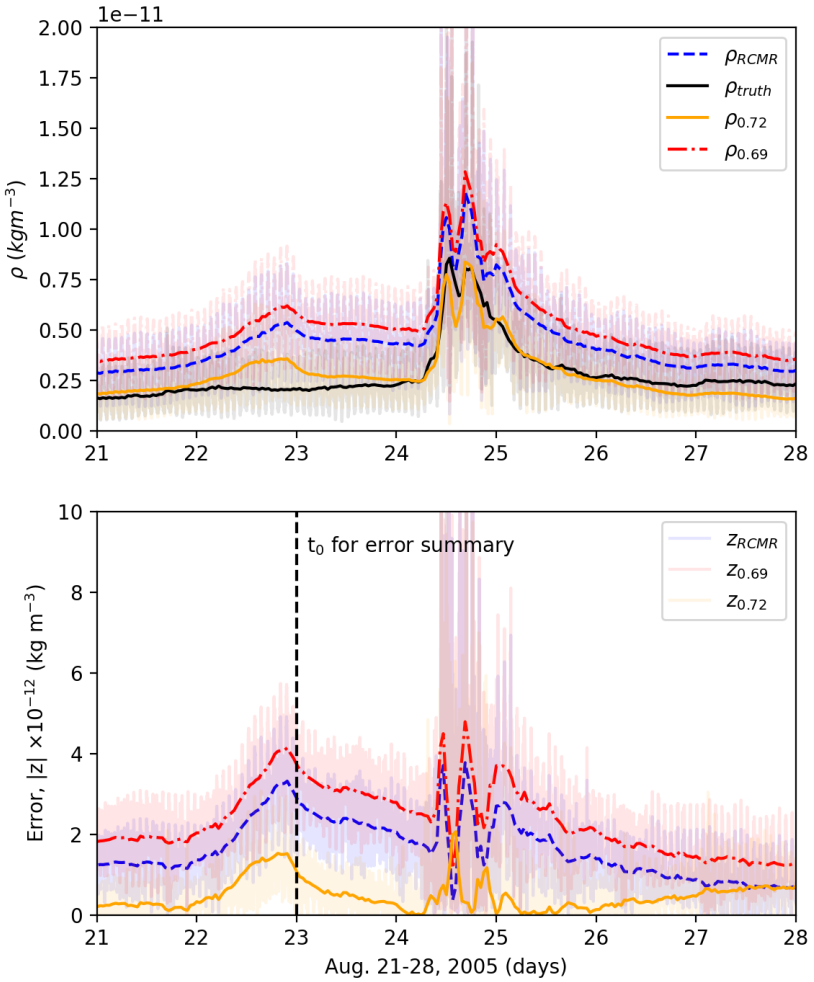

Figure 3.15: Similar to Figure 3.13, but for the MSIS debiased mass densities at CHAMP locations.

Figure 3.15 shows the same runs proceeding through the storm and storm recovery, but now at the CHAMP positions. These densities are quite different than the subsolar density, since CHAMP is a high inclination satellite sampling the high latitudes, where the energy balance can be quite different. In this case, the biased run performed worst of the three runs. In Table 3.4, the same performance tools from Kalafatoglu Eyiguler et al. (2019) are shown. The RCMR run performed similarly or better than the biased run, but considerably worse than the calibrated GITM run. This is due to the difference between MSIS and CHAMP during the proceeding time period. Since RCMR was debiasing towards MSIS, the debiasing improvement is subject to the accuracy of MSIS. It is possible that debiasing with MSIS at locations other than at 400 km altitude at the

subsolar point could improve this, but it was not explored in this work. This simulation does show that debiasing with an empirical model improves the performance of the biased model, but then is subject to other limitations.

Performance Assessment Tool	$\rho_{F10.7}$	ρ_{150}	ρ_{RCMR}	$\rho_{0.72}$	$\rho_{0.69}$	ρ_{RCMR}
Ratio$_{max}$ (-)	0.98	1.56	0.98	0.98	1.5	1.38
Ratio$_{avg}$ (-)	0.96	2.00	0.9	0.96	1.75	1.52
TD (hours)	3.8	3.8	-0.8	3.8	3.8	3.8
MAE (kg/m^3)	4.44e-13	3.13e-12	3.47e-13	4.44e-13	2.35e-12	1.64e-12
NRMSE (%)	8.32	48.68	8.29	8.32	38.15	27.41
PE (-)	0.65	-1.06	0.65	0.65	-0.62	-0.16

Table 3.4: Statistical analysis on orbit-averaged data from t_0 for each run in Figure 3.13. The first two are dimensionless quantities. TD is the time difference between storm peak as seen from data and from the model computed in hours. The mean average error (MAE) has units of kg/m^3. The normalized root mean square error (NRMSE) is shown as a percentage. The prediction efficiency (PE) is also a non-dimensional statistic. The columns are separated by run-type the first three columns being associated with debiasing with CHAMP data and the final three columns are associated with debiasing with MSIS.

3.4 Summary and Conclusion

In this work, GITM used RCMR with CHAMP and GRACE satellite measurements to correct for uncertain parameters and incorrect drivers. During these runs, it was shown that after sufficient error accumulation, RCMR was able to reduce the bulk of the error and nRMS to below 5% within 2-3 days. This work also showed the effectiveness of debiasing GITM prior to a storm in August 2005 with CHAMP measurements and MSIS. When debiasing was applied before a storm, the results during the storm were shown to improve in all metrics except the time delay between a measured storm peak and the model-predicted peak (where they performed identically with and without RCMR). It was demonstrated that RCMR could use empirical models within GITM to debias the model, but this was reliant on MSIS results having low error during the pre-storm time period and the choice of where to sample the empirical model. Future work will show more runs and have a statistical approach to address how beneficial using MSIS for parameter estimation can be. This work also implied that reducing the model bias improved the forecasting performance along a specified path. Lower model bias in neutral densities help make GITM a more feasible model to assist in satellite drag calculations. Getting the acceleration due to drag correct is important for accurate estimation of future satellite positions and potential collision detection and

prevention.

3.5 Open Research

GITM is freely available through GitHub (Ridley et al., 2023). Dst obtained from the World Data Center in Kyoto, Japan (https://wdc.kugi.kyoto-u.ac.jp/dstdir/). CHAMP and GRACE satellite data is available through Technical University, Delft (http://thermosphere.tudelft.nl/). The MSIS model is available on the Community Coordinated Modeling Center (https://ccmc.gsfc.nasa.gov/modelweb/models/nrlmsise00.php). Hemispheric power is provided by the National Oceanic and Atmospheric Administration (http://ftp.swpc.noaa.gov/). Plotting routines and data within this work are published on DeepBlue (https://doi.org/10.7302/9r1a-c979).

Acknowledgements

The research presented in this study was supported at University of Michigan partially by the U.S. Air Force Office of Scientific Research under Dynamic Data-Driven Applications Systems grant FA9550-16-1-0071. This work was also supported by the joint NSF-NASA Space Weather with Quantified Uncertainties program under NSF grant number 2028125 and NASA grant number 80NSSC20K1581.

CHAPTER 4

The Venus Global Ionosphere-Thermosphere Model (V-GITM): A Coupled Thermosphere and Ionosphere Formulation

4.1 Introduction

The search for life in our galaxy is a fundamental quest. In order to help in this process, an understanding of the habitability of different planetary environments is important. The launch of the new James Webb Space Telescope with the Transiting Expolanet Survery Satellite (TESS) will bring new data from the mapping of transiting exoplanets around bright stars, allowing spectroscopic analysis of a planet's atmospheric composition. Planets that are very close to the star are more likely to be observed due to the higher frequency of passing in front of the star. Along with this, there are characteristics that inner, rocky exoplanets may have in common. For example, it has been found is that the closer planets are to a star, the more likely they are to be tidally locked (Barnes, 2017). In addition, planets near a star often times encounter large amounts of solar radiation leading to the escape of lighter species, such as hydrogen and oxygen, throwing the carbon cycle out of balance resulting in a CO_2 rich atmosphere (Ehrenreich, D. and Désert, J.-M., 2011) (Taylor, F.W. et al., 2018). In our own solar system, Venus shares some of these characteristics. For example, Venus is not tidally locked, but has a very slow axial rotation period of 243 days which may respond similarly to the effects of stellar heating of tidally locked planets.

Further, Venus' atmosphere is dominated by CO_2. Comparative planetology of terrestrial planets and the role of CO_2 15 μm cooling in regulating the temperature structure of their upper atmospheres has been shown to be different between Venus, Earth and Mars (Bougher et al., 1999). As such, the CO_2 rich planets (Mars and Venus) have much colder thermospheric temperatures than at Earth. Knowing that radiative cooling is such an important process for these planets and is so dependent on atomic O and CO_2 densities, it becomes equally important to constrain the densities of each species. As pointed out in Huestis et al. (2008), atomic O should have variability throughout

the solar cycle for Mars and Venus but measurements are severely lacking. Bougher et al. (2023) used MAVEN NGIMS datasets and compared to M-GITM simulations to capture solar cycle effects upon exospheric temperatures. Measured O abundances were used to constrain simulated O densities and CO_2 cooling rates on Mars for the first time.

Atmospheres dominated by CO_2, slowly-rotating and tidally locked planets are very different than what we experience at Earth, but may be commonplace in exoplanets. For example, over 5,200 confirmed exoplanets are cataloged in NASA's Exoplanet Archive. A good way to partition whether they are potentially habitable is to link Venus-like or Earth-like characteristics for each exoplanet.

Measurements and numerical models are used to answer questions about the evolution, habitability, and the underlying physics of these atmospheres. Models allow for testing of different configurations, characterizing uncertainty ranges to broadly predicting habitability. On the other hand, direct measurements are probably the most reliable sources of data to attempt to improve our understanding of these atmospheres, but obtaining this data is a difficult task, and therefore the measurements are quite limited. New missions and modeling efforts characterizing the dynamics of the atmospheres of Venus and Mars assist in understanding atomic O densities and the radiative cooling that results. As our ability to describe the role of radiative cooling at Venus and Mars improves, we will be able to better synthesize exoplanet data and improve our ability to assess the habitability of planetary bodies.

4.1.1 Venus Data Sets used for Comparison in This Work

A variety of satellite missions with different instruments have visited Venus to collect data on the atmospheric state. Ground-based telescopes (see James Clark Maxwell Telescope and Heinrich Hertz Submillimeter Telescope) are capable of mesospheric temperatures and carbon monoxide densities. Remote-sensing revealed the temperatures at a larger variety of altitudes and the atmosphere's neutral and ion densities. Limaye et al. (2017) has compiled many ground-based and satellite-based instrument measurements of Venus' atmosphere and ionosphere, which are summarized here, and used in later sections to validate model results:

- SPICAV (Spectroscopy for the Investigation of the Characteristics of the Atmosphere of Venus) uses a UV spectrometer and two IR spectrometers onboard Venus Express (Bertaux et al., 2007). The UV instrument provides density and temperature profiles from approximately 60 km to 160 km. The VIS-IR instrument is one of two infrared sensors, but this is used in the $0.7 - 1.7 \mu m$ wavelength range to gather H_2O, CO_2 and aerosol information along with $O_2(1-\Delta)$ nightglow. SOIR (solar occultation IR) is part of the SPICAV suite of spectrometers, but measures CO_2 spectral lines from 2.2-4.3 μm (Korablev et al., 2003),

(Mahieux et al., 2008). Data is available at a wide variety of latitudes at the terminators between 70-170 km.

- JCMT (James Clark Maxwell Telescope) is a ground-based radio telescope in Hawaii that is capable of making sub-mm observations of CO absorption lines and temperatures between 70-110 km. Due to the differences in day-night CO densities, the observation range may vary.

- HHSMT (Heinrich Hertz Sub-Millimeter Radio Telescope) is located at the Arizona Radio Observatory and provides temperature profiles and CO distributions from 40-120 km on the dayside and nightside (Rengel et al., 2008).

- VeRa (Venus Express Radio Science) used radio signals to sound Venus' atmosphere and ionosphere at all longitudes and latitudes during Venus atmospheric occultation (i.e., the signal is occulted by Venus's atmosphere). During the occultations, Venus' atmosphere lies between satellites radio transmitter and the ground station receivers or on Deep Space Network antennas. Measurements of the attenuated radio signals were used to derive atmospheric states. VeRa.0 and VeRa.1 provide density and temperatures from 40 km up to roughly 100 km (Häusler et al., 2006).

- VIRTIS-H (Visible and InfraRed Thermal Imaging Spectrometer, high resolution channel) observed non-LTE emissions of carbon monoxide as part of the Venus Express spacecraft. Gilli et al. (2015) retrieved dayside temperatures, albeit with large uncertainties, between 100-150 km at a variety of local time and latitude bins by averaging non-LTE emission measurements.

- Pioneer Venus' Orbiter Neutral Mass Spectrometer (ONMS) measured density variations at low latitudes in the upper thermosphere (Keating et al., 1979). The data observed from this instrument are the foundation for the VTS3 empirical model, which is discussed more in the next section.

In addition to the data currently available, there have been two recently selected missions, VERITAS and DAVINCI, which will probe the atmosphere of Venus with new instruments. Venus Emissivity, Radio Science, InSAR, Topography, and Spectroscopy (VERITAS) aims to improve upon the radar maps from the Magellan mission in the 1990s, help scientists learn about the nightside IR emissivity, and measure the gravitational field around Venus to gain insights on the planet's core. VERITAS, now optimistically scheduled to launch in 2031, will perform aerobraking maneuvers that will sample the thermosphere and provide further constraints on upper atmospheric structure. The Deep Atmosphere Venus Investigation of Noble gases, Chemistry, and Imaging

(DAVINCI) mission is planned to launch as early as 2029. DAVINCI aims to deliver high precision measurements of the composition of the atmosphere as it descends through the thermosphere down to near surface altitudes (Garvin et al., 2022).

Piecing together all the data provides clues about the composition, dynamics and energetics of Venus' atmosphere, but they only tell part of the story due to data being available at limited times and discrete locations. Models are tools that can provide a complete four-dimensional dataset and can test our understanding of the physics of the Venusian atmosphere. Models have a variety of structures and assumptions that shape their usefulness in different situations.

4.1.2 Model Review

There are many models (empirical and first-principles-based) of the Venusian thermosphere:

- VTS-3: An empirical model created by Hedin et al. (1983) that used a spherical harmonic fitting of measurements from Pioneer Venus' Orbiter Neutral Mass Spectrometer (ONMS) from 1978 - 1980 to estimate measurements from 100 km to around 300 km. Near equator sampling by ONMS do not provide VTS-3 with useful mid-to-high latitude constraints. Also, ONMS in-situ datasets did not make measurements below about 140 km so extrapolations down to 100 km by VTS-3 are not well constrained. Empirical models rely on data assimilation from remote observations so they are able to estimate background atmospheric states well, but due to low statistics do not have the same success in dynamic conditions, such as flares. VTS-3 is used as a comparison tool for the model presented here.

- The empirical model from Theis et al. (1984) and Theis and Brace (1993) provide electron densities and electron temperatures extracted from Pioneer Venus' Orbiter Electron Temperature Probe (OETP) using the method described in Krehbiel et al. (1980). This has similar latitudinal and altitudinal constraints as VTS-3.

- VIRA (Venus International Reference Atmosphere) used both lower and upper atmosphere datasets to capture reference profiles at specific locations and intervals throughout the solar cycle (Kliore et al., 1985). For instance, upper atmospheric mass densities and temperatures were based upon PVO OAD datasets (Keating et al., 1985). VIRA-2 (Moroz and Zasova, 1997) updated the reference profiles based on composition, temperature and pressure measurements.

- VTGCM: The Thermosphere Ionosphere General Circulation Model (TIGCM) (Dickinson et al., 1984) was modified to work at Venus (Bougher et al., 1988; Brecht et al., 2011, 2012; Parkinson et al., 2021). VTGCM is a 3D physics-based model on a pressure coordinate

system. At the time, this model displayed the importance of 15 μm CO_2 cooling to balance EUV heating effects. VTGCM also uses a wave-drag parameterization to reduce the horizontal wind speeds.

- V-PCM: The Laboratoire de Météorologie Dynamique (LMD) team created a Venus GCM, formerly LMD-VGCM, (Gilli et al., 2017, 2021; Navarro et al., 2021; Martinez et al., 2023) now referred to as the Venus Planetary Climate Model (V-PCM). The V-PCM includes two unique parameterizations for the effects of the near IR solar heating at 4.3 μm and the radiative cooling at 15 μm. Additionally, a gravity wave parameterization is included to dampen the fast winds and improve stability of runs.

- TUGCM: Tohoku University's GCM (TUGCM) (Hoshino et al., 2012, 2013) uses an atmosphere of O, CO and CO_2 only and implements planetary scale waves (Rossby waves, diurnal and semidiurnal tides, and Kelvin waves) based on the assumption that these are driven upward from the mesosphere.

A side-by-side comparison of the physics-based models (V-PCM, TUGCM and VTGCM) was put together in Martinez et al. (2021). This comparison table presents some features of each model and was modified to justify the development of a new model, V-GITM. Table 4.1 shows the high-level differences between each model.

4.1.3 The Need for a New Venus Model

This study introduces a new Venus model which is focused on better understanding (1) how the nightside ionosphere of Venus is sustained, (2) what controls the thermospheric temperature as a function of altitude and solar zenith angle, (3) the impact of the retrograde super-rotating flow on the winds, densities, and temperatures, and (4) the role of the wind dynamics on day-night structures. The flexibility in the new model improves upon the simulated physics and leads to better answering the outstanding questions at Venus. The three important improvements to the physics this work offers are the use of chemical heating, a non-hydrostatic solver and the inclusion of coupled ion dynamics.

For example, the method of using chemical heating is standard at Earth, but less common for planetary environments. It is typical for GCMs to adopt a heating efficiency to account for the heating effects from the solar EUV. In many cases, this method offers a good approximation, but the implementations are incomplete when using a uniform heating efficiency due to the solar EUV heating coming through a route of ionizing neutrals that release heat in exothermic chemical reactions. Ions are not uniformly distributed and so the chemical reactions do not heat the thermosphere uniformly making a constant heating efficiency inaccurate. The use of an uncertain

	V-GITM	VTGCM	V-PCM	TUGCM
State variables	T, u, v, w, p, see Table 4.2 for neutrals and ions considered	T, u, v, w, O, CO, N_2, CO_2, Z, N(^{4}S), N(^{2}D), NO, O_2, SO, SO_2, PCE ions	T, u, v, w, O, CO, CO_2 + photochemical model (Stolzenbach et al., 2023)	T, u, v, w, O, CO, CO_2, N, Z
Vertical domain	70-170 km: 1 km spacing	70-200/300 km: 69 pressure levels	0-200/250 km: 90 pressure levels	80-150/180 km: 38 pressure levels
Horizontal Resolution (Lon $\times$ Lat)	Flexible, in this work $5^\circ \times 2^\circ$	$5^\circ \times 5^\circ$	$3.75^\circ \times 1.875^\circ$	$10^\circ \times 5^\circ$
Temporal discretization	Runge-Kutta Fourth Order, 0.5-1s timestep	Leapfrog scheme, 20s timestep	Leapfrog-Matsuno scheme, 21s timestep	Leapfrog scheme, 4s timestep
Hydrostatic assumption	No	Yes	Yes	Yes
Ionosphere	Photochemistry and O_2^+ dynamics	Photochemistry	Photochemistry	-
EUV Heating	Chemical heating + 1% FISM model	20-22% F10.7 model	17% E10.7 model	10% F10.7 model
Near IR	Direct absorption with an IR heating efficiency	Tabulated heating rates from: Roldán et al. (2000) Crisp (1986)	Martinez et al. (2023)	Ratios between NLTE and LTE heating rates calculated by the GCM (López-Valverde et al., 1998)
Eddy diffusion coefficient (m^2 s^{-1})	300	10-1000 Max value occurs above turbopause	-	0-500 Max value occurs above turbopause

Table 4.1: Four physics-based Venus models side-by-side comparing model characteristics and physics parameterizations. Adapted from Martinez et al. (2021).

heating efficiency produces an unreliable heating balance which may simulate incorrect temperatures and wind speeds or, in the case of plausible results, it biases our understanding of the physics incorrectly.

Hydrostatic equilibrium is a state of planetary atmospheres when the vertical pressure gradients are balanced by the effects of the planet's gravitational pull. This balance prevents atmospheres from being completely lost to space or collapsing under its own weight. As shown in Table 4.1, the existing Venus GCMs assume hydrostatic equilibrium to simplify the vertical wind calculation. V-GITM's non-hydrostatic solver is better-suited to address questions at Venus where it is still undetermined if the hydrostatic assumption is always appropriate. The hydrostatic assumption breaks down when vertical and horizontal scales are on the same order of magnitude, which is not the case in this study, but become more important as finer resolutions are used. Navarro et al. (2021) began exploring the effects of a finer horizontal grid and suggested the development of a

shock on Venus. It was also mentioned that the hydrostatic dynamical core may be limiting the 3D modeling of shock formation. GITM explicitly solves for the winds without the use of artificial wave-breaking which is useful for allowing vertically propagating sound waves to form naturally. This makes V-GITM a useful tool to support the findings of a shock-like feature or determine if the shocks are an artificial creation originating from the hydrostatic assumption.

Due to the slow-rotation of Venus, dayside ions do not co-rotate with Venus all the way to the nightside due to the timescales of chemistry. For this reason, Venus' nighttime ionosphere is assumed to be driven by ion dynamics or precipitating particles. Currently, VTGCM and V-PCM assume use a chemistry model with no advection to simulate the ionosphere. As discussed in section 4.2.3, V-GITM includes the dynamics of O_2^+ in an attempt to create a nightside ionosphere.

4.2 The Venus Global Ionosphere-Thermosphere Model (V-GITM)

The original Global Ionosphere Thermosphere Code (Ridley et al., 2006) was adapted into a Mars model that goes from the surface of Mars to 300 km which has been referred to as M-GITM (Bougher et al., 2015b). M-GITM is a 3D spherical code based in altitude coordinates that solves the Navier Stokes equations for the ions, electrons, neutral densities, temperatures and winds as well as the ion composition and velocities. It includes multiple parameterization models that are embedded in the code, including: (1) a model to simulate the effects of the dust in the lower atmosphere of Mars (Jain et al., 2020); (2) a modern NLTE CO_2 15 μm cooling scheme (Roeten et al., 2019) and (3) a FISM-M solar flux model, based upon MAVEN EUVM measured EUV-UV fluxes at Mars, is used to drive M-GITM solar heating, dissociation and ionization rates (Thiemann et al., 2017). A flat 20% EUV heating efficiency is used. FISM is able to better represent the solar EUV entering the Martian atmosphere compared to an Earth-based F10.7 proxy model.

V-GITM begins with the Mars GITM code, taking advantage of existing chemistry and CO_2 cooling scheme. Mars unique processes, such as dust storms and wave-drag parameterizations, are removed in the new model. The solar EUV heating has transitioned from using a 20% heating efficiency to primarily using chemical heating.

4.2.1 Planetary and Orbit Characteristics

The GITM code is very modular, making updating planet and orbit characteristics straightforward to update. Some of the main items that required updating are shown in Table 1.

Property	Mars	Venus
Surface Gravity (m/s^2)	3.73	8.87
Rotation period (days)	1.03	233.5
Radius (km)	3388.25	6051.8
Axial Tilt	25.19°	0°[1]
Sun-Planet Distance (AU)	1.38-1.67	0.718-0.728
Eccentricity	0.093	0.0067
Neutral Species Considered	$\mathbf{CO_2}$, $\mathbf{CO}$, $\mathbf{N_2}$, $\mathbf{O_2}$, $\mathbf{O}$, $\mathbf{Ar}$, $\mathbf{N(^4S)}$, $\mathbf{He}$	$\mathbf{CO_2}$, $\mathbf{CO}$, $\mathbf{N_2}$, $\mathbf{O_2}$, $\mathbf{O}$, $\mathbf{N(^2D)}$, $\mathbf{Ar}$, $N(^4S)$, NO
Ion Species Considered	O_2^+, O^+, CO_2^+, N_2^+, NO^+	$\mathbf{O_2^+}$, $\mathbf{O^+}$, CO_2^+, N_2^+, NO^+

Table 4.2: Planetary constants used for M-GITM and V-GITM. In the case of the final two constants related to orbit characteristics, these values come from Bannister (2001) that have compiled tables from NASA JPL's website (http://ssd.jpl.nasa.gov/). Bolded ion/neutral species are advected in the model. [1]Venus' true axial tilt is around 3°, flipped for retrograde rotation. 0° is used as an approximation until the retrograde rotation is added.

4.2.2 Neutral Dynamics

V-GITM is developed based on the the Earth and Mars Global Ionosphere Thermosphere Models with its own unique set of atmosphere species considered (Table 4.2). The atmospheric constituents and resulting chemistry are very similar to Mars with CO_2 being the major species getting overtaken in the upper thermosphere by atomic oxygen. The model solves the continuity, momentum and temperature equations in three dimensions using a finite difference scheme without assuming hydrostatic equilibrium. The GITM frameworks splits the horizontal solver, vertical solver, and source terms. Below, the vertical equations with source terms are described in detail, while the horizontal advection equations are similar to those described in Ridley et al. (2006).

The continuity equation is:

$$\frac{\partial N_s}{\partial t} + \frac{\partial u_{r,s}}{\partial r} + \frac{2u_{r,s}}{r} + u_{r,s}\frac{\partial N_s}{\partial r} = \frac{1}{N_s}C_s \tag{4.1}$$

where r is the radial (vertical, positive outward) direction in spherical coordinates, N_s is the total number density for species s for each bolded element in Table 4.2 , C_s is the sum of the source and loss terms due to chemistry and $u_{r,s}$ is the vertical velocities of species s. The sources and losses due to chemistry are computed for the reactions in Table 4.3.

Photolysis is the category of reactions that are performed when incoming radiation causes an ionization or dissociation of a neutral particle. This is a necessary component for creating and maintaining the dayside ionosphere on Venus. When ions are created, they may undergo charge exchange or recombination with an electron. Charge exchange or recombination are typically exothermic reactions and therefore produce heat that gets absorbed in the atmosphere. Keeping

track of this exothermic chemical heating is a major difference in V-GITM from existing Venus models that approximate this process via a direct heating rate, taking a fixed percentage (typically between 8-25%) of the incoming solar EUV energy deposition and using that as an energy source.

Reaction Number	**Chemical Reaction**	**Reaction Rate** ($m^3 s^{-1}$)	**Exothermicity** (eV)
Photolysis			
R1	$N_2 + h\nu \rightarrow N(^4S) + N(^2D)$		
R2	$N_2 + h\nu \rightarrow N_2^+$		
R3	$CO_2 + h\nu \rightarrow CO_2^+$		
R4	$CO_2 + h\nu \rightarrow CO + O$		
R5	$O + h\nu \rightarrow O^+$		
R6	$O_2 + h\nu \rightarrow 2O$		
R7	$O_2 + h\nu \rightarrow O_2^+$		
R6	$NO + h\nu \rightarrow N(^4S) + O$		
R7	$NO + h\nu \rightarrow NO^+$		
Neutral Bimolecular Chemistry			
R8	$CO_2^+ + O \rightarrow O_2^+ + CO$	1.64×10^{-16}	1.33
R9	$CO_2^+ + O \rightarrow O^+ + CO_2$	9.6×10^{-17}	-
R10	$CO_2 + O^+ \rightarrow O_2^+ + CO$	1.1×10^{-15}	1.21
R11	$N(^4S) + O \rightarrow NO$	See Appendix A	-
R12	$N(^2D) + O \rightarrow N(^4S) + O(^3P)$	2.0×10^{-17}	2.38
R13	$N(^2D) + O \rightarrow N(^4S) + O(^1D)$		0.42
R14	$N(^2D) + CO_2 \rightarrow NO + CO$	2.8×10^{-19}	-
R15	$O_2^+ + N(^4S) \rightarrow NO^+ + O$	1.0×10^{-16}	4.19
R16	$O_2^+ + N(^2D) \rightarrow NO^+ + O$	1.8×10^{-16}	-
R17	$O_2^+ + NO \rightarrow NO^+ + O_2$	4.5×10^{-16}	2.81
R18	$O_2^+ + N_2 \rightarrow NO^+ + NO$	1.0×10^{-16}	-
R19	$N_2^+ + CO_2 \rightarrow N_2 + CO_2^+$	$9.0 \times 10^{-16}(300/T_i)^{0.23}$	1.81
R20	$N_2^+ + O_2 \rightarrow N_2 + O_2^+$	$5.1 \times 10^{-17}(300/T_i)^{1.16}$	3.5
R21	$N_2^+ + O \rightarrow NO^+ + N(^2D)$	See Appendix A	3.06
R22	$N_2^+ + O \rightarrow O^+ + N_2$	$7.0 \times 10^{-18}(300/T_i)^{0.23}$	1.01
R23	$N_2^+ + NO \rightarrow N_2 + NO^+$	3.6×10^{-16}	6.32

Table 4.3: Photolysis and neutral bimolecular chemistry reactions with their corresponding reaction rates and exothermicity in V-GITM. Reaction rates are adopted from (Fox and Sung, 2001).

During O_2^+ and CO_2^+ recombination, many different states of O and CO can be produced. V-GITM groups all excitation states as one species in the model, i.e. $O(^1D)$, $O(^3P)$, and $O(^1S)$ are handled as just O. The same is done for CO's different states. The branching ratios that describe the partitioning into each state is important due to the different exothermicity associated with each recombination. Regarding CO_2^+ recombination (see R25), the branching ratios used are (0.24, 0.38, 0.18, 0.20) as follows from Rosati et al. (2003) and Gu et al. (2020).

O_2^+ recombination (see R24) branching ratios also vary with the O_2^+'s vibrational state (ν). As

Reaction Number	Chemical Reaction	Reaction Rate ($m^3 s^{-1}$)	Exothermicity (eV)
Electron Recombination Chemistry			
R24	$O_2^+ + e \rightarrow O(^3P) + O(^3P)$	$2.4 \times 10^{-13}(300/T_e)^{0.7}$	6.99
	$\rightarrow O(^1D) + O(^3P)$		5.02
	$\rightarrow O(^1D) + O(^1D)$		3.06
	$\rightarrow O(^1D) + O(^1S)$		0.83
R25	$CO_2^+ + e \rightarrow CO(X^1\Sigma^+) + O(^3P)$	$3.5 \times 10^{-13}(300/T_e)^{0.5}$	8.31
	$\rightarrow CO(a^3\Pi) + O(^3P)$		2.3
	$\rightarrow CO(a'^3\Sigma^+) + O(^3P)$		1.26
	$\rightarrow CO(d^3\Delta) + O(^3P)$		0.49
R26	$NO^+ + e \rightarrow O + N(^4S)$	$3.0 \times 10^{-13}\sqrt{300/T_e}$	2.75
	$\rightarrow O + N(^2D)$	$1.0 \times 10^{-13}\sqrt{300/T_e}$	0.38
R27	$N_2^+ + e \rightarrow 2N(^2D)$	See Appendix A	1.06
Termolecular Neutral Chemistry			
R28	$O + CO + CO_2 \rightarrow 2CO_2$	$6.5 \times 10^{-45} e^{-2180/T_n}$	-
R29	$O + O + CO_2 \rightarrow O_2 + CO_2$	2.75×10^{-44}	-
R30	$O + O + CO \rightarrow CO_2 + O$	$3.4 \times 10^{-39} e^{-2180/T_n}$	-
R31	$O + CO + CO \rightarrow CO_2 + CO$	$6.5 \times 10^{-39} e^{-2180/T_n}$	-

Table 4.4: Electron recombination and termolecular neutral chemistry reaction rates and exothermicity in V-GITM. Reaction rates are adopted from (Fox and Sung, 2001).

described in Petrignani et al. (2005), the branching ratio for $\nu = 0$ is (0.265, 0.473, 0.204, 0.058), $\nu = 1$ is (0.073, 0.278, 0.51, 0.139), and $\nu = 2$ is (0.02, 0.764, 0.025, 0.211). To approximate the correct fractional population of the vibration states by altitude, Figure 1 in Fox (1985) was followed. Below 130 km the vibrational population of O_2^+ is assumed to be 100% in the $\nu = 0$ state. In the altitude range of 130 km - 170 km, each vibrational state was interpolated between the fractional population values found at 130 and 170 km.

At the bottom boundary, each neutral species density is fixed using a constant value estimated by VTS3 except O, N(^{4}S), N(^{2}D), and NO which are all zero. The top boundary assumes a hydrostatic fall off of each species number density.

The vertical momentum equation is:

$$\begin{aligned} \frac{\partial u_{r,s}}{\partial t} + u_{r,s}\frac{\partial u_{r,s}}{\partial r} + \frac{u_\theta}{r}\frac{\partial u_{r,s}}{\partial \theta} + \frac{u_\phi}{r\cos(\theta)}\frac{\partial u_{r,s}}{\partial \phi} \\ + \frac{k}{M_s}\frac{\partial T}{\partial r} + T\frac{k}{M_s}\frac{\partial N_s}{\partial r} \\ = g + F_s + \frac{u_\theta^2 + u_\phi^2}{r} + \cos^2(\theta)\Omega^2 r + 2\cos(\theta)\Omega u_\phi \end{aligned} \tag{4.2}$$

where the north latitude direction is θ and the east longitude direction is ϕ. The eastward and northward bulk velocities are u_ϕ and u_θ, respectively. T is the neutral temperature, while M_s is the

mass of species s. Venus' angular velocity and gravity are Ω and g respectively. The u_θ^2 + u_ϕ^2/r term is due to spherical geometry. The final two terms on the RHS are the centrifugal and Coriolis forces. Neutral-neutral and ion-neutral friction in the F_s are:

$$F_s = \frac{\rho_i}{\rho_s}\nu_{in}(v_r - u_{r,s}) + \frac{kT}{M_s}\sum_{q\neq s}\frac{N_q}{ND_{qs}}(u_{r,q} - u_{r,s}) \tag{4.3}$$

where ρ_i is the ion mass density, ν_{in} is the ion-neutral collision frequency, v_r is the ion velocity in the radial direction, N_q is the total number density for species q that species s interacts with, and N is the bulk number density. D_{qs} is the molecular diffusion coefficient between s and q species as described in Colegrove et al. (1966), table 1. $u_{r,q}$ is the vertical velocity of the other species s. Eddy vertical mixing is added to the vertical velocity solved for in Equation (2) at every time step. The eddy vertical velocity as shown in Malhotra and Ridley (2020):

$$v_{eddy}^s = -K_{eddy}\frac{\partial}{\partial r}(ln(\frac{\rho_s}{\rho})) \tag{4.4}$$

where K_{eddy} is the eddy diffusion coefficient, ρ_s is the species-specific mass density, and ρ is the bulk mass density. Currently, the eddy diffusion coefficient used is a constant value of 300 m^2/s, but can be improved with future work following a variation of the non-uniform profile described in Mahieux et al. (2021). 1D values of the eddy diffusion coefficient may be too large for 3D models, due to the global circulation serving to modify vertical density profiles, thereby reducing the need for additional turbulent effects added via an eddy diffusion coefficient (Bougher et al., 1999).

The top boundary condition for the vertical winds is to have zero gradient for the out flow (positive radial velocities), while preventing any downflow (no downward radial velocities allowed). In the meridional (N/S) and zonal (E/W) direction, the top boundary conditions applies zero vertical gradient. The bottom boundary velocity is zero in the meridional direction and vertical direction, while the zonal velocity follows the cloud top behavior observed at Venus. The cloud motion is persistently westward and is commonly referred to as a retrograde superrotating zonal (RSZ) flow because it is faster than the rotation of the planet (Bougher et al., 2008). The lower boundary condition in the zonal direction is set to be -100 m/s with a cosine fall-off as a function of latitude as shown in Figure 4.1. This condition assists in better understanding the unique impact of the mesosphere on the thermosphere (Peralta et al., 2017; Schubert et al., 2007). A cosine fall-off is an elementary approximation to capture the low-latitude zonal velocity while also reducing the observed high-latitude velocity, which rapidly dissipates poleward of 50-60° N/S (Machado et al., 2012, 2017).

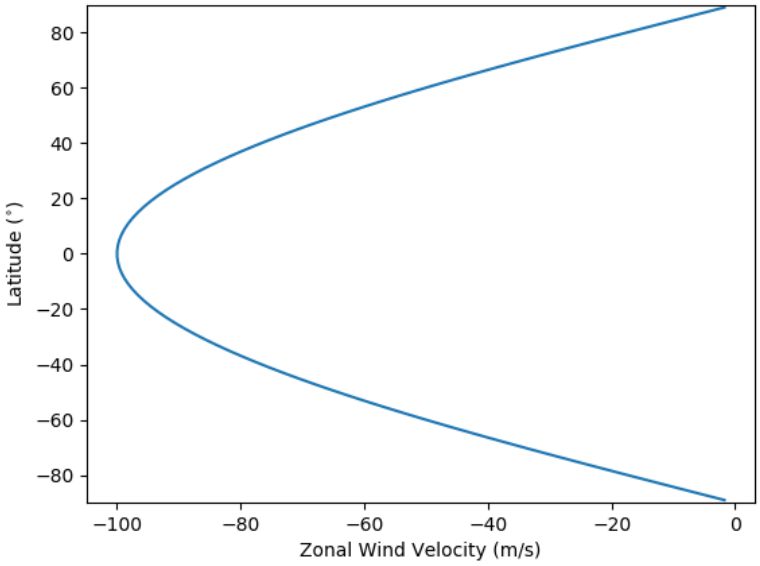

Figure 4.1: Zonal velocity lower boundary condition at 70 km altitude.

The vertical energy equation for the normalized, neutral temperature, $\mathcal{T} = kT/\bar{m}_n$ is:

$$\frac{\partial \mathcal{T}}{\partial t} + u_r \frac{\partial \mathcal{T}}{\partial r} + (\gamma - 1)\mathcal{T}(\frac{2u_r}{r} + \frac{\partial u_r}{\partial r}) = \frac{k}{c_v \rho \bar{m}_n} Q \tag{4.5}$$

where γ is the adiabatic index that is attached to the change in energy from the expansion of the gas, c_v is the specific heat constant, k is Boltzmann's constant, and $\bar{m}_n$ is the mean mass. The various source terms are given by:

$$Q = Q_{EUV} + Q_{IR} + Q_O + Q_{CO_2} + Q_{CHEM} + \frac{\partial}{\partial r}((\kappa_c + \kappa_{eddy})\frac{\partial T}{\partial r}) \tag{4.6}$$

where Q_{EUV} and Q_{IR} are the contribution from the Sun's extreme ultraviolet and infrared, respectively. The Q_O and Q_{CO_2} detail the cooling to space from the 63 μm and $15 \mu m$ bands respectively. Q_{CHEM} combines heat generated from exothermic reactions. κ_{eddy} is the heat conductivity due to eddy diffusion coefficient and κ_c is the molecular heat conductivity.

There are multiple options for adding the EUV flux. One implementation is EUVAC (Richards et al., 1994). This model estimates the top of atmosphere flux in 37 wavelength bins based using the 10.7 cm solar radio flux. One issue with EUVAC is that it does not extend to long enough wavelengths to fully describe the CO_2 physics. Photoabsorption, photodissociation and photoionization cross-sections for these 37 bins can be found in Schunk and Nagy (2004). Another option is to use the Flare Irradiance Spectral Model (FISM) fluxes (Chamberlin et al., 2008) which

GITM re-bins into 59 wavelengths from 0.1 nm to 175 nm. This option allows the user to input their own top of atmosphere fluxes or absorption/ionization cross-sections. Heays, A. N. et al. (2017) has compiled more than 100 different atoms and molecular photoabsorption, dissociation and ionization cross-sections in 0.1 nm spacing. This data is stored in the Leiden Observatory database (https://home.strw.leidenuniv.nl/$\sim$ewine/photo/). The neutral gas heating efficiency, the fraction of the total EUV energy absorbed into the atmosphere directly, is computed using a flat 1%.

Due to the varying distance from the sun, the planets receive varying amounts of radiation. For Earth, the TIMED spacecraft's Solar EUV Experiment (SEE) instrument (Woods et al., 2005) provides binned data for FISM. At Mars, the MAVEN satellite is able to monitor fluxes of several EUV wavelengths received at Mars (Eparvier et al., 2015), allowing for a Mars-specific FISM (Thiemann et al., 2017). For V-GITM, the FISM values at Earth are used and then scaled according to the r^{-2} proportionality:

$$F_{venus} = F_{earth}(\frac{d_{se}}{d_{sv}})^2 \tag{4.7}$$

where F_{earth} is the FISM EUV fluxes observed at Earth, d_{se} is the distance between the sun and the Earth, d_{sv} is the distance between the sun and Venus. With using FISM fluxes from a non-Venus planet, it is somewhat difficult to determine how useful the scaled measurements are. These measurements are only sufficient assuming that Venus and Earth are on the same side of the sun during the time of the FISM measurements. Since the results presented here do not involve comparisons for specific intervals, it is assumed that this approximation is reasonable.

The source of near infrared heating is a complex process which involves solar radiation to be absorbed and excite a CO_2 molecule. De-excitation and heat deposition occurs via quenching, direct thermalization or transfer to other particles. IR wavelength bands between 2-4 μm. Gilli et al. (2017) created a parameterization based off of the non-LTE model heating rates produced from Roldán et al. (2000). The parameterization was updated more recently in Gilli et al. (2021) to provide better agreement with the resulting PCM model's temperature structure. V-GITM can be run using either of these two parameterizations, but lacks IR heating at and beyond the terminators for the Gilli parameterization. For this reason, the IR heating within V-GITM utilizes a similar method to the EUV absorption given a CO_2 absorption cross-section, top of atmosphere intensity and wavelength energy. The intensity is then attenuated as a function of the optical depth, which is computed using the constituents of the atmosphere's absorption coefficients and evaluating the Chapman integrals which help determine the optical path. Smith and Smith (1972) improved Chapman's accuracy at large solar zenith angles which better captures the solar EUV and IR heating effects near the terminators.

Although there are more processes than CO_2 absorption, a first-principles based method would require a full radiative transfer code which V-GITM does not have due to the complexity and extra computational expense. V-GITM attempts to follow Gilli et al. (2021)'s process of matching heating rates to temperature measurements. Instead of via a parameterization, CO_2 absorption at 2.7 μm and 4.3 μm with cross-sections prescribed at 6.5e-24 $m^2$and 3.0e-25 m^2 respectively. Top of atmosphere fluxes for the 2.7 and 4.3 μm were 1.25e-15 W/m^2 and 4.9e-16 W/m^2 respectively. Such small cross-sections deposit heat over a large altitude do6main which may not be representative of what is actually occurring and so an IR-specific heating efficiency is applied to reduce some of the heating in the non-LTE region. The heating efficiency shown in Figure 4.2 uses a flat 100% up to 135 km in which a cosine function is used to reduce the heating efficiency to 0% at 170 km. The cosine function used:

$$\epsilon_{IR} = \begin{cases} 1.0 & z \leq z_0, \\ \frac{1}{2}(\cos(\omega(z - z_0)) + 1) & z > z_0 \end{cases} \tag{4.8}$$

where z is the local altitude, z_0 is the altitude in which below 100% heating efficiency is applied (i.e. 135 km), and ω is the angular frequency to fit a half period between z_0 and the top of the model. In this case, $\omega = \pi/(z_{top} - z_0)$, where z_{top} is the top of model altitude. This is done because GITM's absorption-only scheme produces non-trivial heating effects at altitudes above 140 km where quenching and other effects occur that, while occuring at these wavelengths, would not be accurately modeled through absorption coefficients. The heating efficiency from equation (8) helps remove the higher altitude heating that would otherwise make this inconsistent with other estimations of the near IR heating (Roldán et al., 2000; Gilli et al., 2017, 2021).

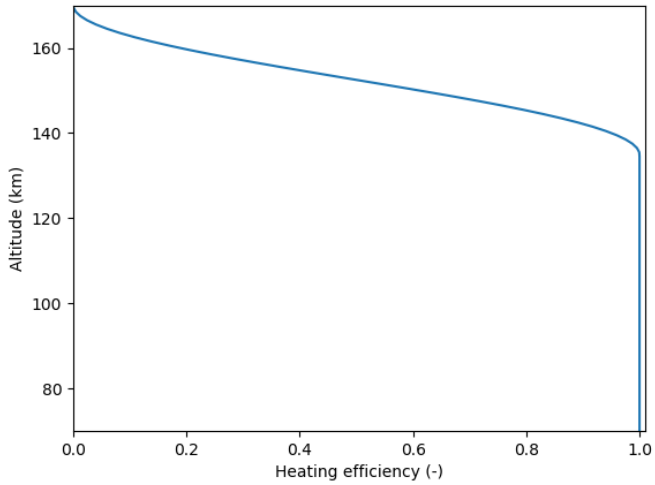

Figure 4.2: Infrared heating efficiency applied to direct absorption of 2.7 and 4.3 μm into CO_2.

The 15 μm cooling strongly controls the thermospheric structure at Venus (Bougher et al., 1994, 1999). Atomic oxygen excites CO_2 to enhanced vibrational and rotational states, which then radiates energy that is lost to space or is reabsorbed, depending on conditions. This process is responsible for the cold lower thermospheric temperature observed by satellite measurements (Schubert et al., 1980; Bougher et al., 1999, 2008). To properly estimate the effects of the CO_2 cooling, a full radiative transfer model is best, but this is not computationally practical in 3D, so the cooling effects follow the M-PCM non-LTE paramaterization (González-Galindo et al., 2013). The non-LTE parameterization simplifies the full problem into 5 rotational and vibrational levels, computes heat transfer between atmospheric layers and allows for spatially variable atomic oxygen and CO_2 densities. This code has been used in the M-PCM, V-PCM and M-GITM models (Bougher et al., 2017; González-Galindo et al., 2013; Gilli et al., 2017, 2021). Due to the necessity of CO_2 cooling in the LTE portion of the thermosphere and the non-LTE nature of this model, the lower thermosphere is cooled using a linear extrapolation from approximately 70-95 km. The effects of this assumption are discussed in subsequent studies.

At the top of the model, the neutral temperatures has a zero gradient. The bottom boundary neutral temperature is fixed at 215 K motivated by Limaye et al. (2017)'s compiled datasets.

4.2.3 Ion Dynamics

The ion continuity equation is:

$$\frac{\partial N_i}{\partial t} + \frac{v_\theta}{r}\frac{\partial N_i}{\partial \theta} + \frac{v_\phi}{r\cos(\theta)}\frac{\partial N_i}{\partial \phi} + v_r\frac{\partial N_i}{\partial r} = S_i \tag{4.9}$$

where N_i is the number density of the i^{th} ion and S_i is net rate at which the i ion is being produced or lost. The bottom boundary has zero gradient for all ions, but does not matter due to lack of substantial ion densities at that altitude. At the top, the ion densities follow an exponential fall off.

The ion momentum equation in the Venus code is different than the equation found in Ridley et al. (2006). The first difference is the removal of Lorentz force term due to the lack of planetary electromagnetic fields. The solver of the velocity is also changed due to the inclusion of the time rate of change term. The base ion momentum equation is:

$$\rho_i \frac{d\mathbf{v}}{dt} = -\nabla(P_i + P_e) + \rho_i \mathbf{g} - \rho_\mathbf{i} \nu_\mathbf{in}(\mathbf{v} - \mathbf{u}) \tag{4.10}$$

where the $\nabla(P_i + P_e)$ is the plasma pressure and $\mathbf{v}$ is the ion velocity. The velocity is solved for using an implicit time-stepping scheme, where the ion velocity on the right side of the equation is assumed to be the new velocity. The bottom boundary for the ion velocity is fixed at zero in the vertical direction. The top boundary has zero gradient for the horizontal drifts.

One of the problems with ionospheric models that are limited in altitude is that they can not capture the combined vertical and horizontal ion transport that may occur above the top of the model domain. For example, at Earth, ions flow up on the dayside into the plasmasphere, and then down at the night, filling in the nightside ionosphere. At Venus, there is evidence of O^+ transport at high altitudes from the dayside to the nightside during solar maximum to sustain the night-time ionosphere (Kliore et al., 1979; Knudsen, 1992). Currently, V-GITM does not advect O^+ and so it is not expected that the nightside ionosphere will be highly accurate yet.

During solar minimum, it is thought that the ionopause is compressed such that the ionosphere becomes too small to allow O+ transport to be the primary source of nightside ions, but rather that precipitating electron fluxes are sufficiently large to be a significant source of the ionization. Kliore et al. (1979) computed nightside electron densities from the precipitation of 30 eV, 75 eV, and 300 eV electrons based on information from Pioneer Venus measurements (figure 4 in their paper). Theis and Brace (1993) created an empirical model that provides nightside electron density and electron temperature values also based on Pioneer Venus measurements, as shown in their Figure 3a. They showed the densities can vary by nearly an order of magnitude depending on the solar cycle. More work by Brecht and Ledvina (2021) showed a nightside electron density profile produced from a coupling of the VTGCM and HALFSHEL model which matches the results from Theis and Brace (1993). No electron precipitation is included in V-GITM but it is something that could be implemented in future versions.

4.2.4 Initial Conditions and Model Domain

V-GITM follows the VTGCM model with an altitude range from 70 - 170 km. The smallest scale height, H is computed using the heaviest neutral species in the Venus atmosphere, CO_2. With a scale height of approximately 5 km, V-GITM's vertical grid is prescribed to be a uniform 1 km spacing. An adaptive time-step based on a CFL of 0.5 is used. The time-steps are typically 8-10 seconds for the $5^\circ \times 2.5^\circ$ (longitude $\times$ latitude) horizontal resolution used in this work.

The neutral densities are initialized using the VTS3 model, while the ion densities are all set to 1e-24 m^{-3} initially. Neutral and ion velocities are initialized to zero with a bottom boundary condition used to simulate a superrotating flow found near the cloud tops as described in Figure 4.1.

4.3 Simulation Results

In this section, the initial results of V-GITM simulations are shown for a run during March 1st-10th, 2009 in which the F10.7 was around 70 $Wm^{-2}Hz^{-1}$. This time period and F10.7 is representative of solar minimum conditions. Temperatures and densities as functions of time are shown to understand the necessary run-time for the model to reach an approximate steady state. The thermal structure, neutral and ion composition, and winds at the end of the run are shown with some accompanying data-model comparisons in Figures 4.3-4.17.

Figure 4.3 shows temperatures and densities at 75 km and 165 km for noon, midnight, dawn and dusk terminators. The noon and midnight quantities converge within three days with the exception of the 0 LT mass density at 165 km. Although temperatures (3a) and densities (3b) at the terminators changed throughout the entire run at 165 km, the variations are very small compared to the mean values which implies that steady state conditions have been achieved within V-GITM. It is important to point out that although steady state is reached within 5 days, this is only applicable for the current state of V-GITM. Dynamical and chemical time scales determe the time to steady state. These time scales vary with altitude and are important to consider below 100 km, especially as additional chemistry is added to the model (Brecht and Ledvina, 2021).

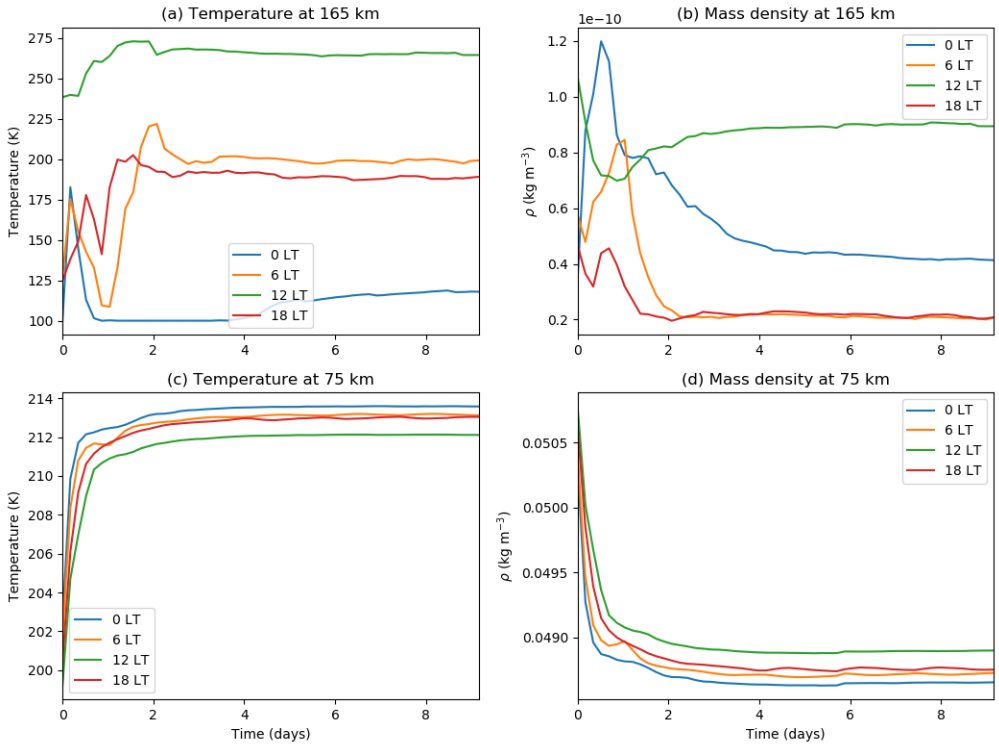

Figure 4.3: The mass density and neutral temperature as indicated near the equator for different local times at 165 km (panel (a) and (b)) and 75 km (panel (c) and (d)).

4.3.1 Thermal Balance and Structure

V-GITM's equatorial temperature as a function of longitude and altitude after 10 days of simulation time is shown in Figure 4.4. The lower altitudes do not have large source terms and the temperature fall off between 70 km to roughly 90 km stems from residual radiative cooling. Temperatures begin to increase above 90 km due to a contribution of heating from the solar near-IR that is absorbed by CO_2. On the dayside, the local temperature peaks at 215 K around 100 km because of the 2.7 μm and 4.3 μm contribution to the near IR heating. Above this local maxima, temperatures decrease briefly until 120 km where the solar near IR absorption peaks and the 15 μm CO_2 cooling has a local minimum.

On the nightside near 0 LT, temperatures decrease from 70 km until 110 km where there is a temperature valley. Above this is a very small peak of around 200 K around 120 km. This temperature peak has significantly colder temperature, approximately 165 K, surrounding this location. The temperature island at midnight near 120 km is created due to fast winds converging on this location. These winds are generated by large pressure gradients stemming from the warm dayside. There is a warm temperature spot at 100 km as well, but a nighttime temperature peak is not observed because the wind pattern is significantly different from the wind pattern at 120 km.

The causes of the different wind pattern is discussed more in section 3.3.1, but is primarily due to viscous interactions with the lower boundary that is significant up to 100 km, but is reduced by 120 km. As seen in Figure 4.4b, the horizontal winds are predominantly westward at 100 km which does not create compressional heating on the nightside.

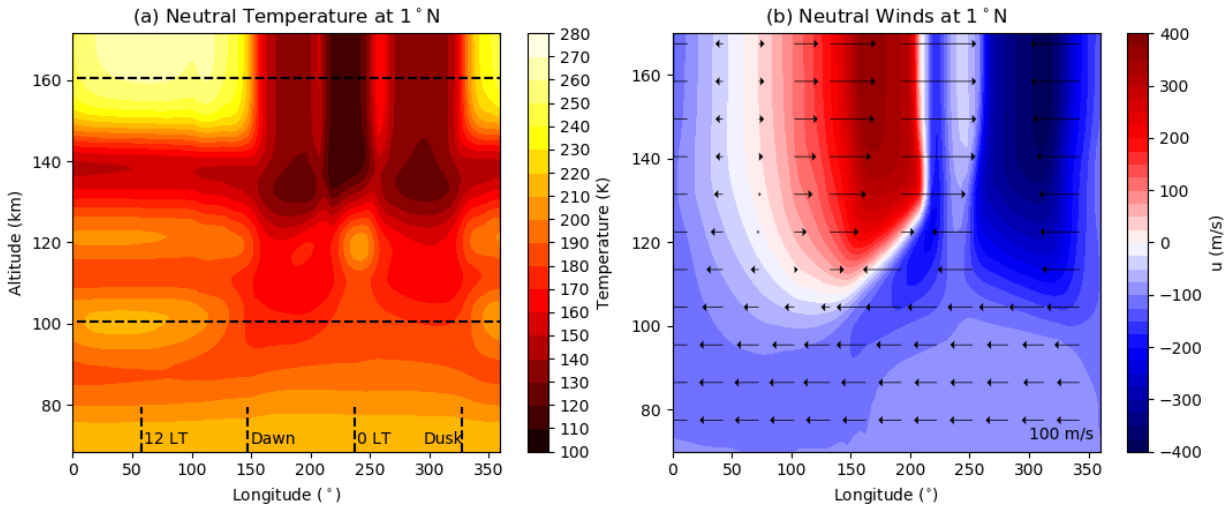

Figure 4.4: V-GITM temperature (left) and neutral winds (right) for a low solar activity simulation on March 10th, 2009 (F10.7 = 70) after simulating ten Earth days. Longitude-altitude cross-section taken at 1.0°N.

Above 140 km on the dayside, temperatures increase to an isothermal profile around 265 K. The heating is due to absorption of solar EUV in the form of direct heating and chemical heating. Between 140-170 km, the solar EUV is balanced by thermal conduction and CO_2 cooling. As shown in Figures 4.4 and 4.5, the diurnal variation is largest in this region with day-night differences of approximately 150 K. The temperature differences drive pressure gradients that create fast winds in the upper thermosphere as shown in Figure 4.4b and discussed in section 4.3.3.

On the nightside, temperatures drop to 110 K at the top of the model because of the lack of heating sources, with the only source being from adiabatic heating at 200° and 260° longitude. As shown in Figure 4.5b, there is a ring where temperature increases due to the convergence of winds near midnight. This region is where the supersonic winds from the dayside to the nightside slow down to subsonic speeds. This behavior was shown in other modeling studies, such as Navarro et al. (2021). This is discussed further in section 4.3.3.

Observational data from ground-based measurements from HHSMT and JCMT, along with Venus Express's VeRa data and empirical model results from VTS3 were compiled in Limaye et al. (2017). Figure 4.6 shows a data-model comparison using the Limaye et al. (2017) data and V-GITM results (dashed black line) latitudinally binned from 30°S to 30°N and longitudinally

binned based on local time (LT) between 7 LT and 17 LT.

Between 120 km and 135 km, there are limited measurements of the dayside temperature. Interpolating data from HHSMT at 120 km and VTS3 results at 135 km, it appears that temperatures should be between 180-200 K. HIPWAC-THIS and VIRTIS-H have measured this region with very large uncertainty bars. V-GITM's solar EUV quickly falls off below 145 km leading to a valley of temperature at 135-140 km. More measurements are needed to understand the appropriate heating and cooling balance in this region. This could be that solar EUV in V-GITM is not depositing energy low enough, the 2.7 μm near IR is not contributing at high enough altitudes, or some combination of the two.

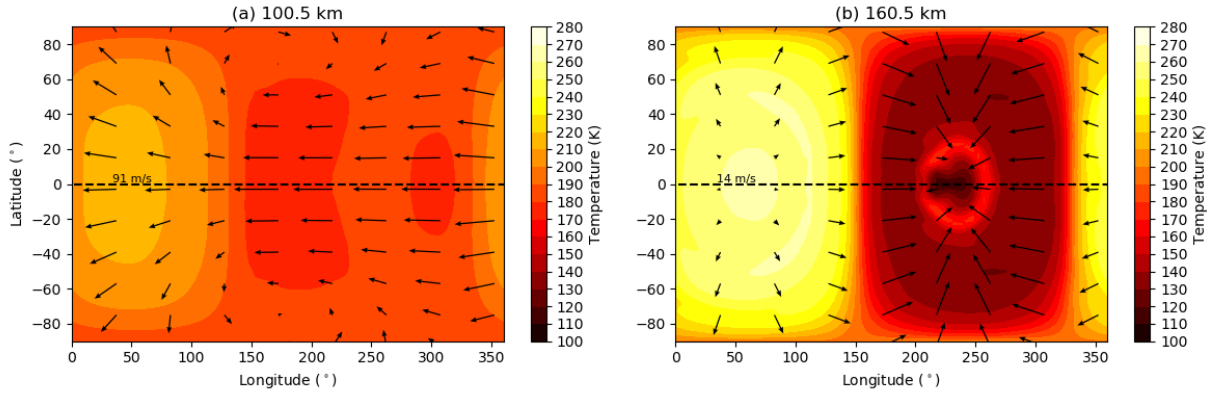

Figure 4.5: Temperature contours shown of constant altitude slices at (a) 100.5 km and (b) 160.5 km overlayed with horizontal winds for the same time as in Figure 4.4. A reference vector wind speed is shown at noon, near the equator, but maximum velocities are 137 m/s and 373 m/s for 100.5 km and 160.5 km, respectively.

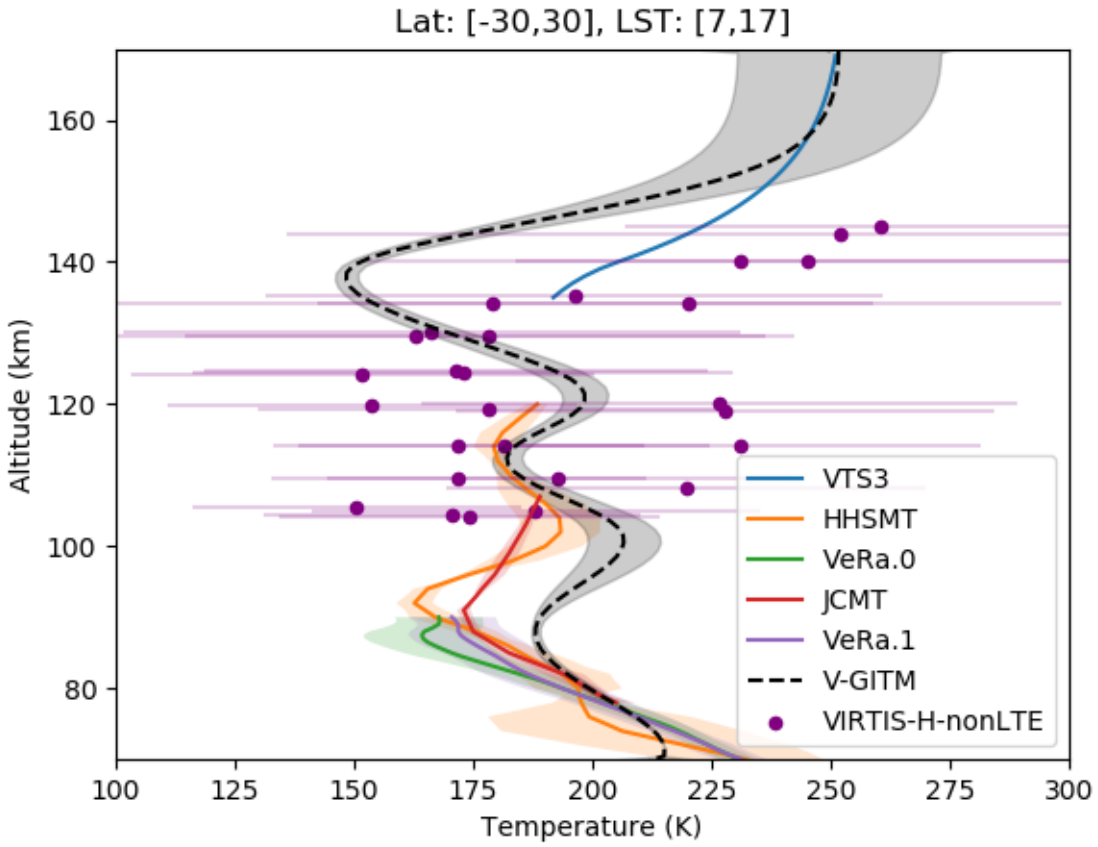

Figure 4.6: Dayside averaged temperature profiles from JCMT, HHSMT, VTS3, VeRa and V-GITM for the low latitude bins between -30° and 30° for March 10th, 00 UT, 2009. One standard deviation are plotted as colored areas for averaged profiles in the same bin.

The dayside heat balance described above is illustrated in Figure 4.7. The non-LTE 15 μm CO_2 cooling scheme is used between $\sim$100 km-170 km. One correction that V-GITM includes is a linear extrapolation of NLTE CO_2 cooling value at 100 km value down to a desired 70 km cooling rate. This is due to a breakdown of the NLTE scheme which does not work effectively below 100 km. The extrapolation cooling scheme was chosen in an attempt to match the HHSMT, VeRa, and JCMT profiles.

The near IR heating rate is a the sum of contributions from the transmission and direct absorption of the 2.7 μm and 4.3 μm spectra. The 1D profile shown in Figure 4.7 features heating throughout a similar vertical domain as the parameterization of Gilli et al. (2017), but with a dayside peak heating rate similar to Gilli et al. (2021).

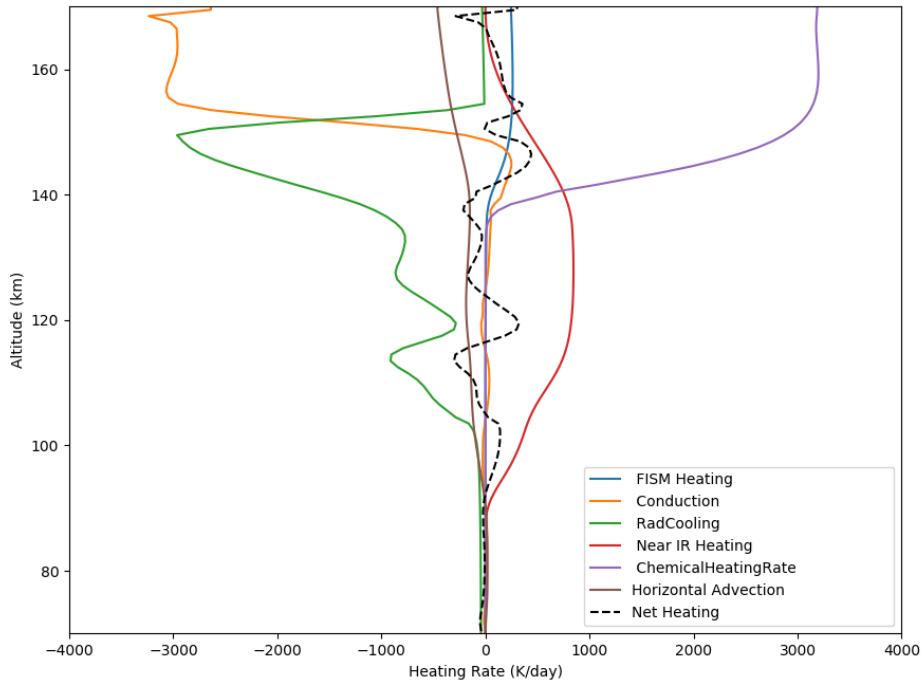

Figure 4.7: Heating and cooling rates (K/day) by V-GITM at 12 LT and 1°N for the same time as shown in Figure 4.4.

4.3.2 Neutral Densities

Resulting vertical profiles of V-GITM's nine individual neutral species from the simulation described above are shown in Figure 4.8. Several densities and density peaks are shown in Table 4.5 comparing the V-GITM results to VTS-3, Venus Express, VTGCM or Fox and Sung (2001)'s model.

Atomic O overtakes CO_2 as the dominant species in the thermosphere at altitudes where molecular diffusion is stronger than eddy diffusion. Matching VTS-3, V-GITM showed this to occur on the dayside and nightside to occur near 165 km and 140 km, respectively. At midnight, V-GITM's atomic oxygen peak value is 7×10^{11} cm^{-3} at 120 km whereas Venus Express measured a smaller value of roughly 2.5×10^{11} cm^{-3} nearer 100 km (Brecht et al., 2012). The disparity between the nightside values at 100 km could be due to the westward winds at this altitude advecting oxygen to the nightside. The nightside O(1-Δ) airglow that results from this simulated O-density peak could be a useful constraint on the thermospheric circulation (Brecht et al., 2011, 2012). Although not done in this thesis, it is a topic of future work. Below 80 km, O has a rapid decreases in density due

Measurable Quantity	V-GITM Result	Comparison Result	Reference
$z(n_{CO_2} = n_O)$	165 km at 12 LT 140 km at 0 LT	165 km at 12 LT 140 km at 0 LT	VTS-3
$\max(n_{O,12LT})$	6×10^{10} cm^{-3}	-	-
$\max(n_{O,0LT})$	7×10^{11} cm^{-3}	2.5×10^{11} cm^{-3}	Venus Express (Brecht et al., 2012)
n_N(140 km)	5.5×10^{7} cm^{-3}	3×10^{7} cm^{-3}	Fox and Sung (2001)
$n_{N(^2D)}$(140 km)	6.5×10^{4} cm^{-3}	2-3$\times10^{5}$ cm^{-3}	Fox and Sung (2001)
$z_{max}(n_{NO})$	95, 125 and 140 km	95 km	Fox and Sung (2001)
$\max(n_{NO})$	3.5×10^{6} cm^{-3}	2-3$\times10^{8}$ cm^{-3}	Fox and Sung (2001)
n_{CO}(170 km)	1.5×10^{8} cm^{-3}	1.2×10^{8} cm^{-3}	VTS-3
n_{N_2}(170 km)	1.4×10^{8} cm^{-3}	7.6×10^{7} cm^{-3}	VTS-3

Table 4.5: Notable density peak locations and number densities from V-GITM (see Figure 4.8) with a comparison against measurements or model-predicted results.

to the lower boundary condition. The lower thermosphere has not been reliably measured and so it is assumed that O will be completely depleted. Additionally, the dayside atomic oxygen density peak is smaller than the peak on the nightside. While it is unclear if this should be the case, having a dayside density to benchmark against is very important. Atomic oxygen is formed by CO_2 photodissociation on the dayside and advected to the nightside. Additionally, 15 μm cooling is highly dependent on oxygen densities. For these reasons, accurately constraining the dayside oxygen profile is necessary to improve the heat balance and nightside densities, chemistry and nightglow.

The nightside O(1-Delta) airglow that results from this simulated O-density peak should be a great constraint on the thermospheric circulation. Please state this here, and for future work in the Conclusions section.

N and N(^2D) are also affected by the lower boundary condition to deplete them. N peaks at 3 $\times10^{7}$ cm^{-3} near 140 km as computed in Fox and Sung (2001) which V-GITM matches reasonably well. Fox and Sung (2001) suggests that the N density may fall off to nearly zero below 115 km which V-GITM does not reproduce. V-GITM shows a secondary peak at 95 km because the only N loss term acting at this altitude is R11 which is acts very slowly. N(^{2}D), on the other hand, should peak between 150 km with a magnitude around 2-3$\times10^{5}$ cm^{-3} from Fox's model. V-GITM showed the peak to be roughly a third of their value.

NO peaks near 95, 125 and 140 km in V-GITM. Fox and Sung (2001) shows that NO peaks

near 95 km two orders of magnitude larger than that shown in V-GITM. Also pointed out in Fox and Sung (2001), NO below 120 km is created by N(^{2}D) and CO_2 producing NO and CO, balanced by a charge exchange between NO and O_2^+ to create NO^+. The N(^{2}D) density below 140 km is very small and so NO is not significantly produced. As seen in section 4.3.5, V-GITM has nearly no O_2^+ below 120 km preventing the charge exchange from occurring. Further investigation in the chemical balance, particularly at lower altitudes, will be given to N, N(^2D) and NO in future work.

The CO and N_2 densities at 70 km and 170 km match the order of magnitude of those predicted via VTS3. As pointed out in Mahieux et al. (2021), CO and N_2 are chemically inactive, particularly at high altitudes in the atmosphere. Despite the mismatch in some of the individual profiles, the dayside total number density profile (Figure 4.9) has agreement throughout.

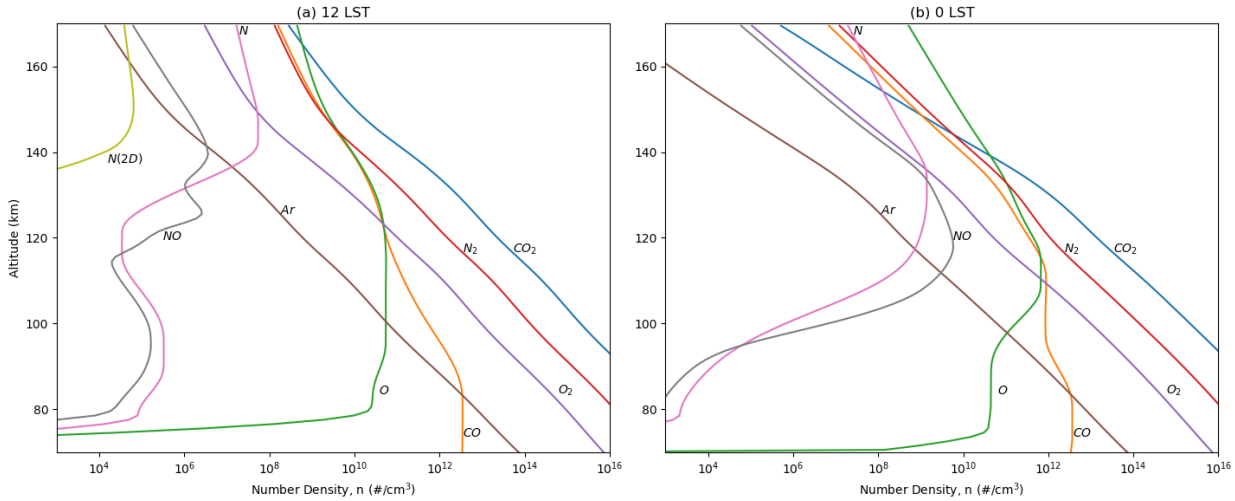

Figure 4.8: V-GITM altitude profile of neutrals at (a) 12 LST and (b) 0 LST at 1°N for March 10th 00:00:00 UT, 2009.

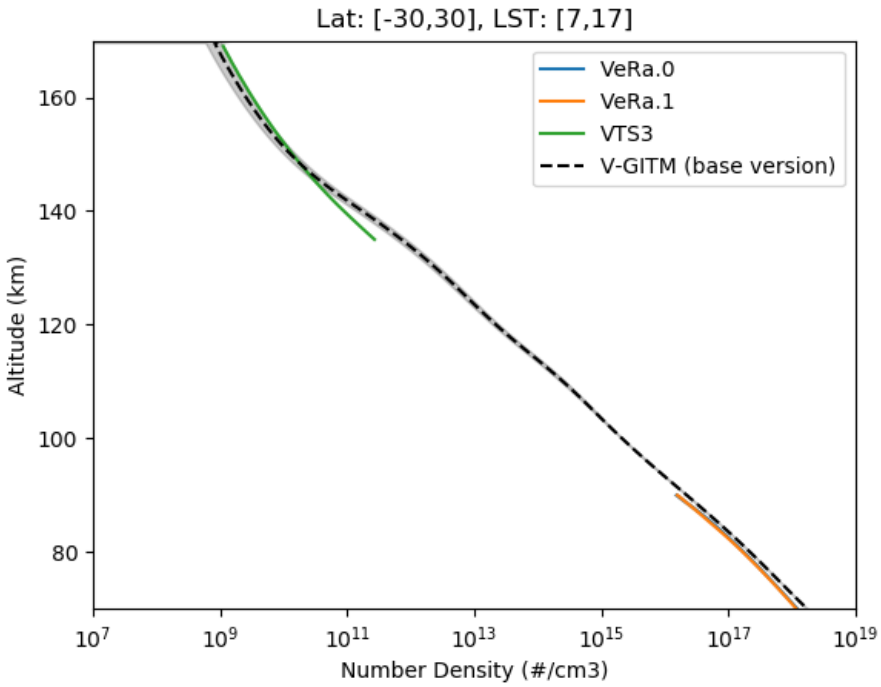

Figure 4.9: Dayside averaged from 30°S-30°N and from 7-17 LST density profiles from VeRa, VTS3 and V-GITM. One standard deviation for V-GITM densities is plotted as a colored area.

4.3.3 Bulk Neutral Winds and Momentum Sources

The V-GITM winds are self-consistently computed at every time step. They are initialized to zero except the bottom zonal superrotating boundary condition. The objective of solving for the winds explicitly is to better understand how the neutral winds in Venus' thermosphere drive atmospheric processes.

As shown in Figure 4.10, the mesosphere and lower thermosphere have a retrograde superrotating zonal (RSZ) circulation pattern. At the top of the thermosphere, EUV deposition creates a large pressure gradient that drives the winds poleward on the dayside at mid latitudes and towards the nightside at low latitudes. These circulation patterns create a large altitudinal velocity shear at the morning terminator where the effects of viscosity are large. The vertical shearing makes it difficult to predict the wind pattern in the transition region between the cloud tops (RSZ flow) and the thermosphere/exosphere boundary (subsolar to antisolar flow). Wind measurements taken by the MESSENGER (only sampling up to 110 km) spacecraft show that the westward maximum wind speeds range from 97-143 m/s (Peralta et al., 2017). In the sampling range, the maximum occurred between 75-90 km. This may suggest a good constraint for the boundary conditions at 70 km. Simulations were performed with different lower boundary conditions on the zonal flow to

understand the impact this may have.

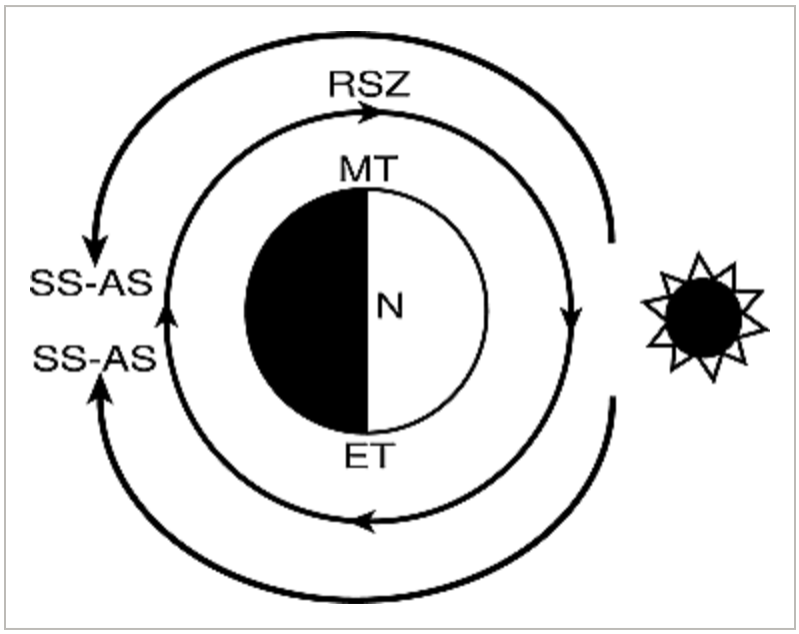

Figure 4.10: Depiction of the retrograde super rotating zonal (RSZ) circulation in the lower atmosphere of Venus with the subsolar (SS) to antisolar (AS) flow at higher altitudes. Adapted from (Schubert et al., 2007)

Horizontal winds, vertical winds, and temperatures produced by V-GITM are shown in Figures 4.11 and 4.12 with different lower boundary condition on the zonal winds of 0 m/s, 50 m/s and 100 m/s. Beginning at 90 km, the horizontal velocity almost identically matches the corresponding boundary condition due to the effects of viscosity from the lower layers. The vertical winds are less than 1 m/s.

The simulated zonal winds at 105 km are a superposition of the day-to-night flow generated due to the large pressure gradient (from near IR at 105 km), which intensifies as the boundary condition zonal wind is increased. This is most apparent at the terminators, particularly at low latitudes. Meridional winds are orthogonal to the zonal winds and so they do not vary much for a specific zonal boundary condition.

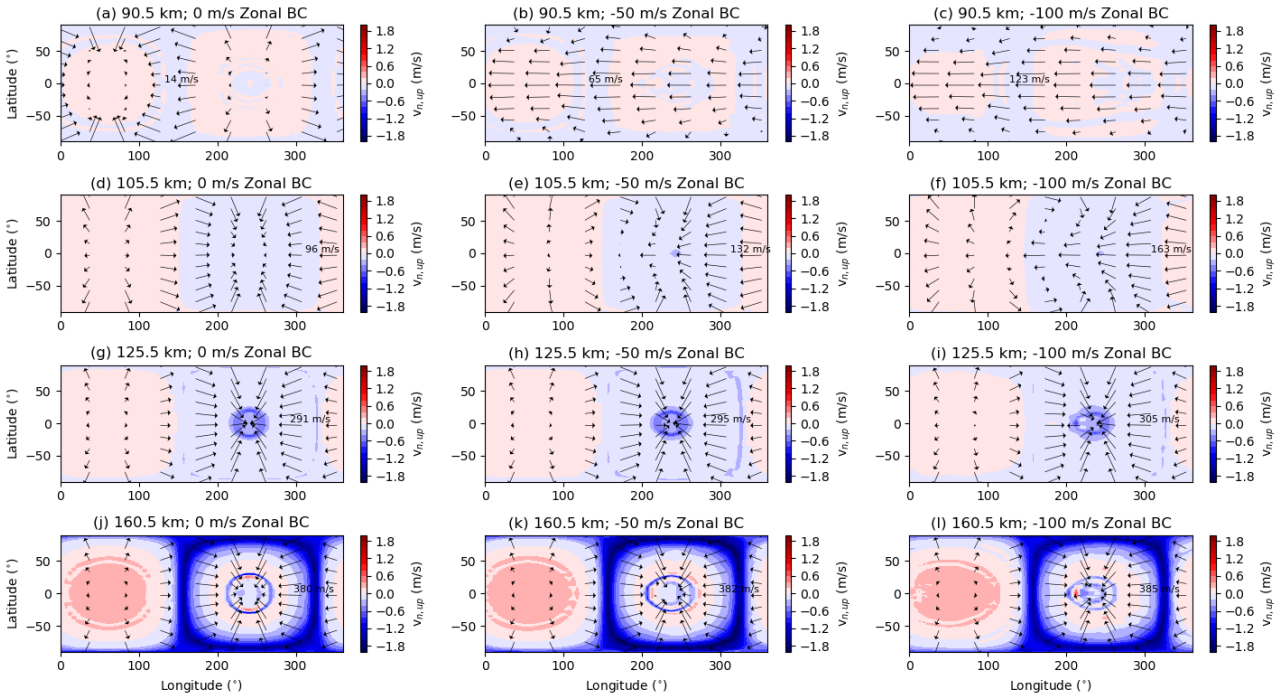

Figure 4.11: Constant altitude slices of horizontal (arrows) and vertical (contours) winds at 90.5 km (first row), 105.5 km (second row), 125.5 km (third row) and 160.5 km (final row). From left to right, columns show lower boundary conditions of 0 m/s, -50 m/s and -100 m/s. Positive vertical wind values correspond to upward motion. Note that the wind vector length scale changes in each plot, while the vertical wind color scale does not.

At 125 km, velocities are noticeably different than the 105 km horizontal velocities. The 0 m/s boundary condition (see Figure 4.11g) has a SS-AS pattern which is also driven by the dayside temperature peak, except that the max velocities are much faster. Subplots (g)-(i) do not vary much and the velocities are all within $\pm$20 m/s indicating that influence of RSZ is much less at this altitude and above. The non-zero boundary conditions runs at 160 km behave in a similar fashion despite the low difference in horizontal wind speeds.

Figure 4.12 shows the nightside, 1°N latitude cross-section of temperature for the 0 m/s, -50 m/s and -100 m/s zonal boundary condition runs. With the 0 m/s run condition, the horizontal winds at high altitudes converge on the nightside producing a small amount of adiabatic heating as described above. The midnight convergence causes the midnight temperatures to be warmest for the -100 m/s RSZ case.

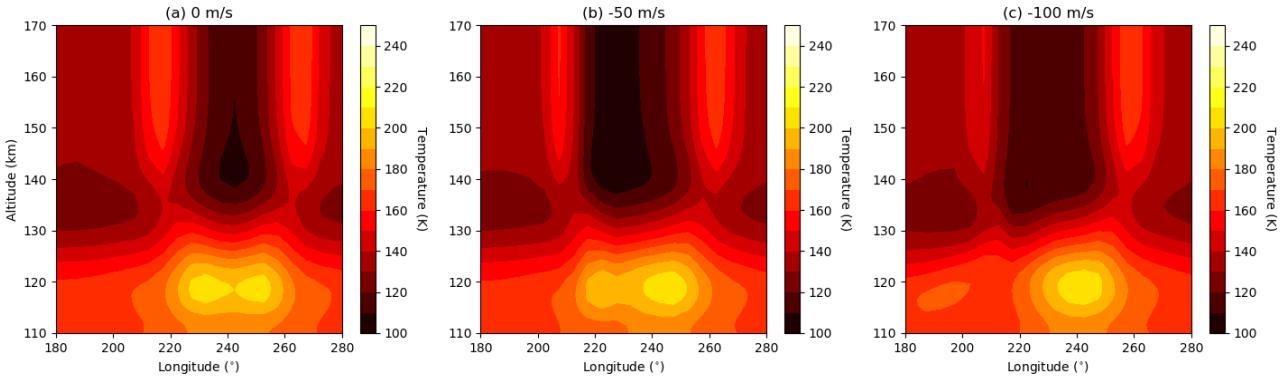

Figure 4.12: Equator slices of temperatures from 110-170 km on the nightside. From left to right, the lower boundary condition is (a) 0 m/s, (b) -50 m/s or (c) -100 m/s.

Figure 4.13 shows the zonal accelerations for the -100 m/s run condition at different local times. A description of these momentum sources, although described in the vertical direction, are discussed in equations 4.2 and 4.3. For the specific horizontal momentum equation, please refer to (Ridley et al., 2006). As previously mentioned, the near IR and solar EUV create warm regions on the dayside. The solar flux is deposited over a large area so the pressure gradient term at noon is not particularly large. The largest temperature and pressure gradients occur at the terminators and are much stronger than any other acceleration term at these locations. Although included in the momentum equation, ion drag is a negligible forcing on the neutrals since there are no magnetic and electric fields to drive the ion motion. For this reason, after a short amount of time the neutrals drag on the ions which accelerates them to move in unison with one another leading to no expected ion drag. However, ion winds from the solar wind interaction may drag neutrals at higher altitudes (Brecht and Ledvina, 2021).

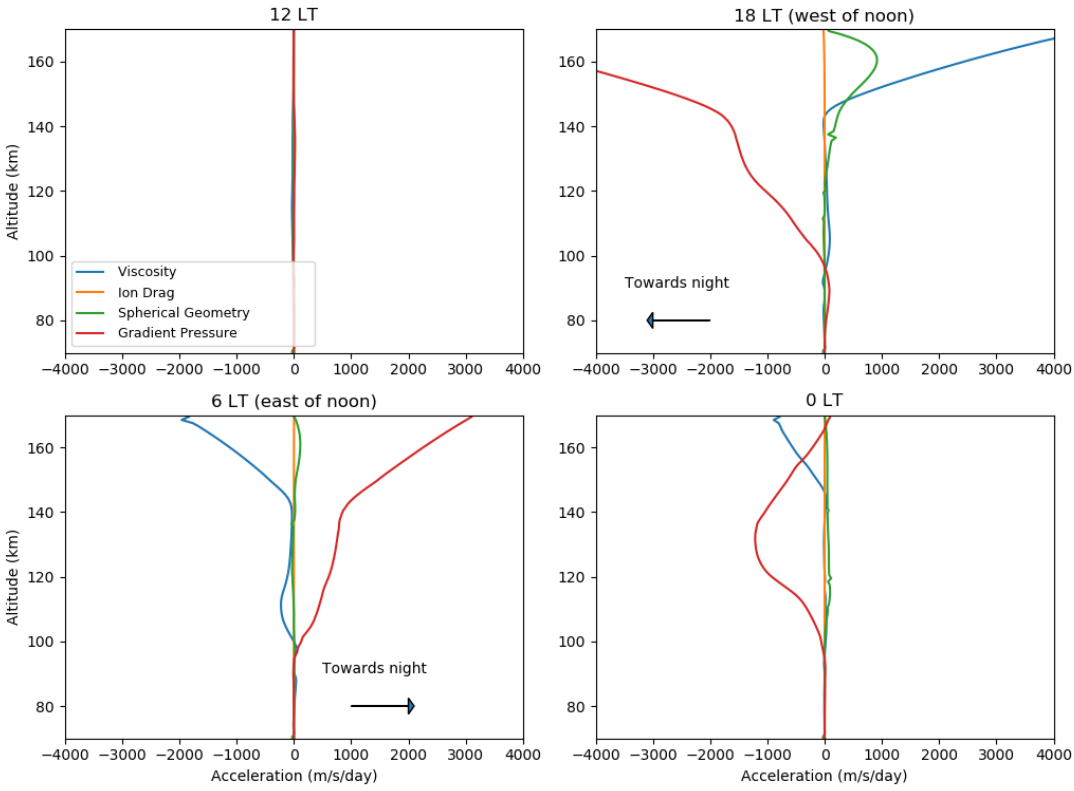

Figure 4.13: Momentum sources at equator in the zonal (east/west) direction for the -100 m/s base case at four different local times.

4.3.4 Shock-like Features within V-GITM

A higher resolution simulation was performed matching the horizontal resolution in Navarro et al. (2021). The standard resolution used up to this point and the Navarro resolution runs are compared in Figure 4.14. Following some of the metrics in their work, V-GITM showed supersonic winds on the nightside and a "hot ring" around midnight during two simulations with different horizontal resolutions. Mach numbers reach a value of 2 east of midnight. West of midnight, the mach number is also supersonic with a lower value of 1.6. The lower resolution was performed at $5^\circ \times 2^\circ$ while the Navarro et al. (2021) is performed at $3.75^\circ \times 1.875^\circ$. Over a distance of roughly 500 km, the flow is slowed to subsonic speeds in both simulations. In addition to the supersonic speeds, the η indicator pointed out in (Navarro et al., 2021) (Zhu et al., 2013) (Fromang, Sébastien et al., 2016) provides a dimensionless quantity to assess the presence of a shock where the η is greater than 0.2. Equatorial values of η were computed at 130 km and 160 km, η remained below 0.2 across all longitudes except around 200-210° and around 250-255°. These longitudes are consistent with the crossings of supersonic to subsonic flows in Figure 4.14c and 4.14d. As mentioned in Navarro et al. (2021), an enhanced model is needed to accurately handle shock formation because fluid

models, even if non-hydrostatic, do not resolve supersonic shock effects.

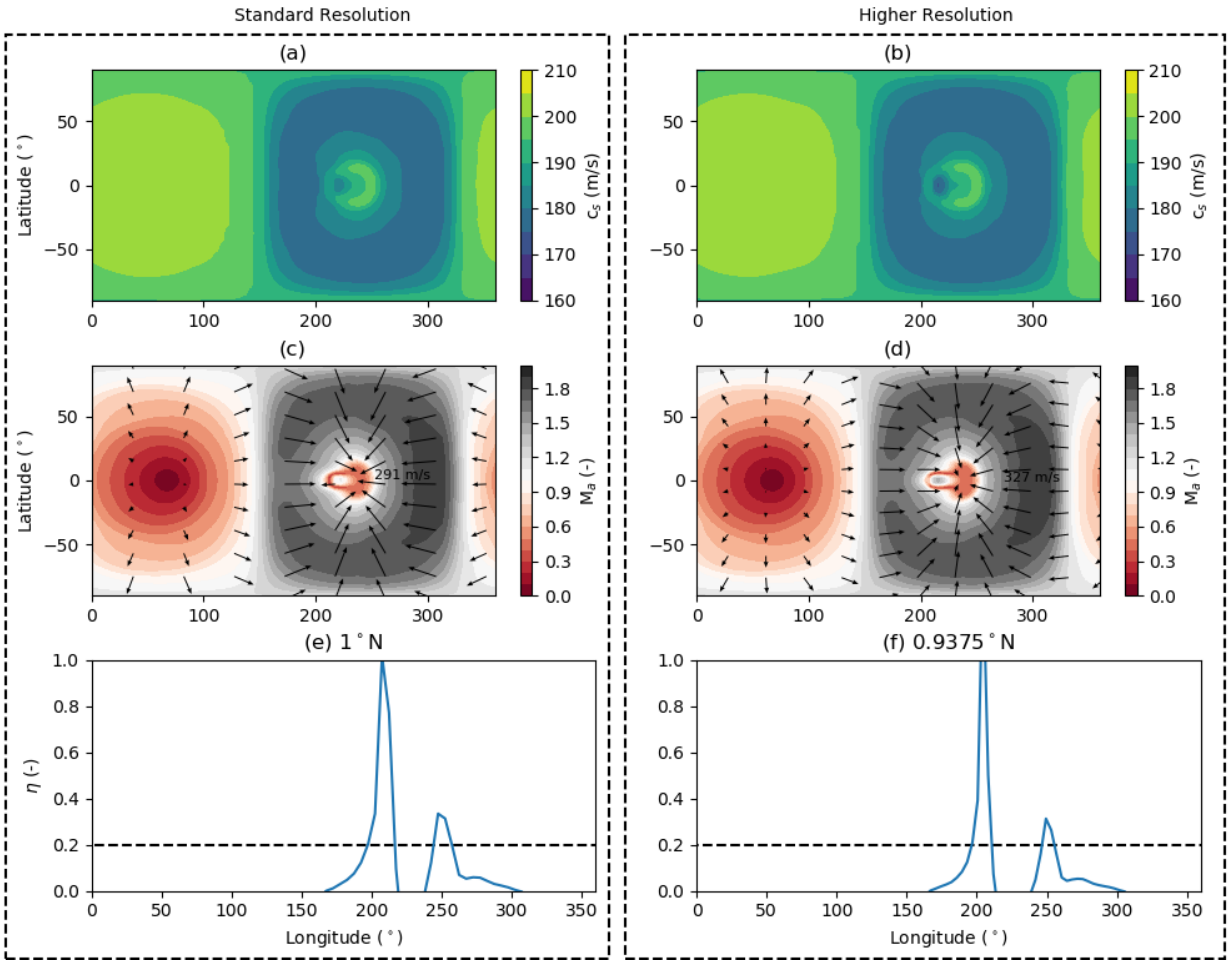

Figure 4.14: The speed of sound (c_s) and Mach number (M_a) and a dimensionless quantity (η) are shown at 130.5 km for two different horizontal resolutions. In (e) and (f), η describes flow divergence was computed at all longitudes near the equator. A black, dashed line showing a threshold of 0.2 is plotted to help distinguish shock locations.

4.3.5 Ionosphere

V-GITM's ionosphere is driven by the photochemistry described in Table 4.3 and coupled ion-neutral dynamics described above. In this section, individual ion density profiles and bulk electron densities are shown in Figure 4.15. The dayside ionosphere is robust, with densities peaking at over 10^5 cm^{-3} which is consistent with Venus Express measurements taken during solar minimum (Hensley et al., 2020). Near midnight, however, a more meager ionosphere exists with the main density being NO^+ which peak values are greater than 10^1 cm^{-3} at 170 km. On the nightside nearer either terminator, the electron density has a peak of 10^3 cm^{-3}. The ion population at these

locations consist of a relatively equal amount of NO^+ and O_2^+. O_2^+ is advected to the nightside, but not fully across the anti-solar point which explains the lack of O_2^+ at midnight in Figure 4.15.

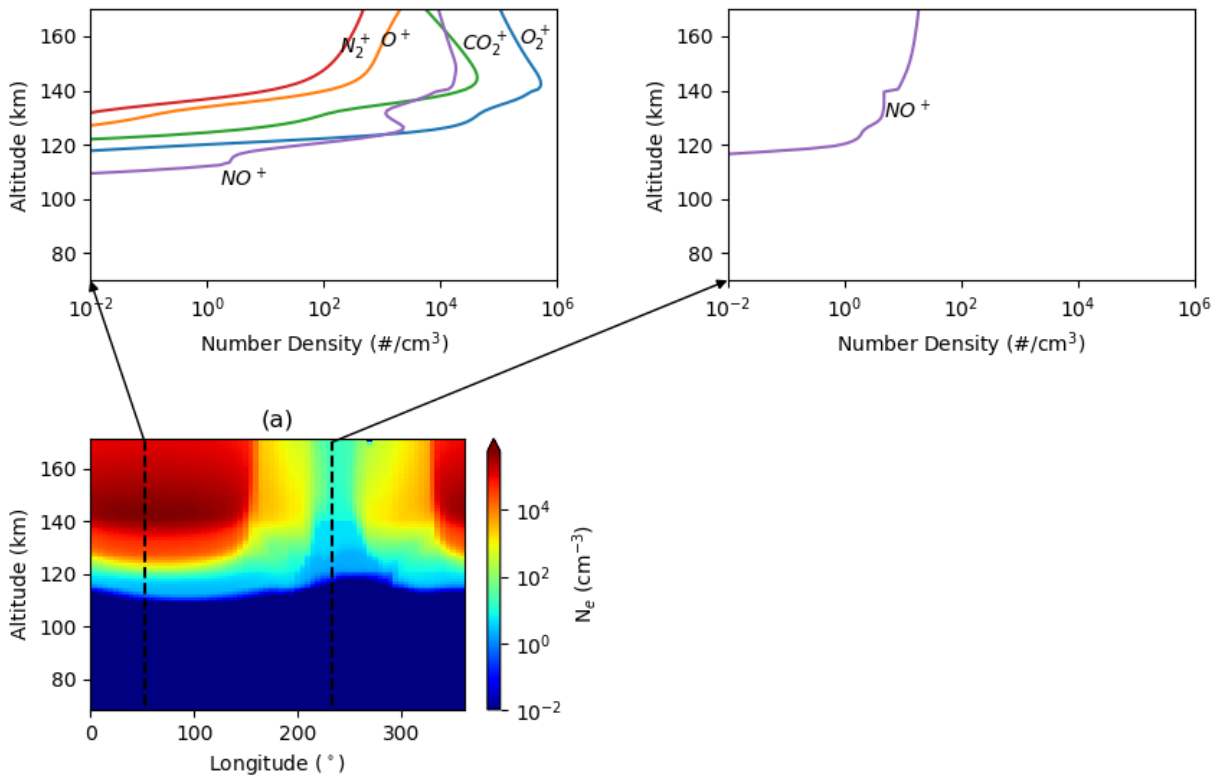

Figure 4.15: Electron densities at the equator with altitude slices showing species-specific ion densities at noon (left) and midnight (right).

Figure 4.16 provides a side-by-side comparison of the neutral and ion velocities at 140.5 km. This location was selected due to O_2^+ being the only species advected and 140 km is near the dayside density peak. The ions and neutrals have been shown to move in unison in the zonal and meridional directions. As seen in Figure 4.16b, the ion vertical velocities have a large downflow on the nightside not seen in the neutrals. This location corresponds to a density of O_2^+ less than 10^2 cm^{-3} and is believed to not be physical nor a significant detraction from the other findings of this simulation.

The midnight cross-section of the ion population (see Figure 4.15) shows only NO^+ despite not being an advected ion. Given the neutral profiles shown in section 4.3.2, the primary reactions creating NO^+ are R15 and R18. NO^+ is lost through electron recombination. Balancing the mass flow rate reaction rates showed that NO^+ will stay roughly 50x larger than the corresponding O_2^+ density. This relationship will hold until additional the NO^+ reaction rate coefficient is re-examined or additional NO^+ loss terms are added.

Overall, the nighttime electron densities are between two to four orders of magnitude less than the simulated dayside. Taylor Jr. et al. (1980) has indicated the day-night difference should be one to three orders of magnitude smaller with the same composition. Cravens et al. (1982) concluded that the nightside ionosphere is highly variable. Occasionally it would be completely depleted ($[e^-] < 10^2$ cm^{-3}), most of the time it showed irregularities and sometimes it was smooth with maximums between 10^4 and 10^5 cm^{-3}.

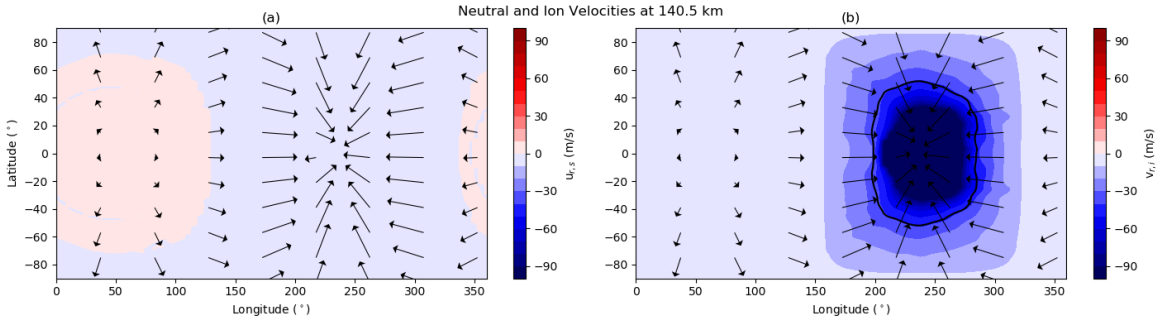

Figure 4.16: Ion and neutral velocities at 140.5 km. Horizontal velocities for the (a) neutrals and (b) ions are plotted as arrows with the corresponding vertical velocity plotted as a contour in the background. A contour line of $n_{O_2^+} = 10^2$ cm^{-3} is plotted in (b).

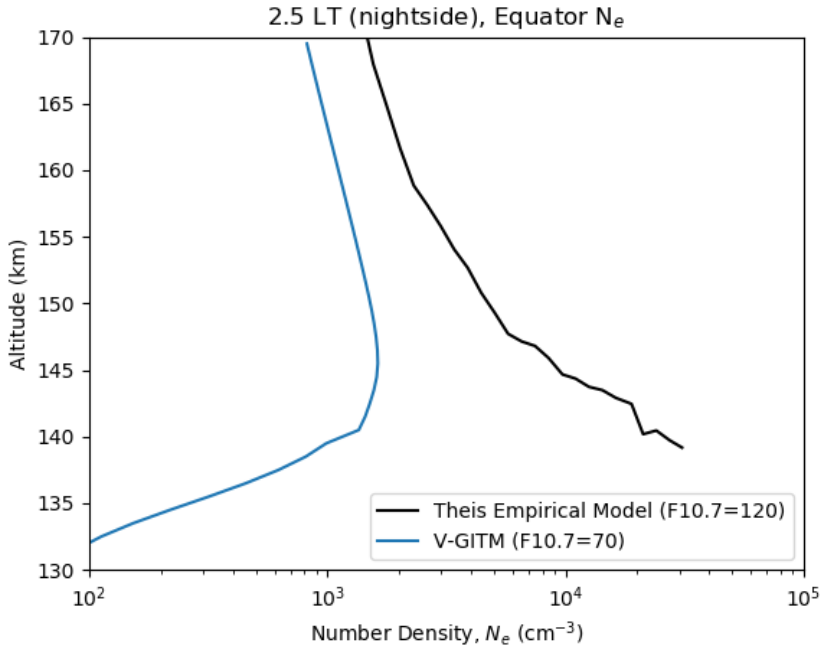

Figure 4.17: Electron density structure at the equator for 2.5 LT for the empirical model from (Theis and Brace, 1993) and V-GITM.

Figure 4.17 shows a data-model comparison of the nightside electron density at 2.5 LT from Theis and Brace (1993) (in black) and V-GITM results (in blue). It is not expected to have the same electron densities between the lines due to the inherent difference in solar activity. Theis and Brace (1993) has shown that between F10.7 values of 120 $Wm^{-2}Hz^{-1}$ and 200 $Wm^{-2}Hz^{-1}$ that the electron density peak does not vary much near 140 km. Knudsen (1987) points out that dayside electron densities may have an effects on the day-to-night flow of plasma.

Spenner et al. (1981) and Kliore et al. (1991) also indicate that transport of O^+ from the dayside is a source of night-time ionosphere, but V-GITM does not extend at high enough altitudes to properly attempt to capture this effect. The influence of a nightside upper boundary condition for O^+ will be explored in future work to simulate this effect. Precipitation of solar wind light ions or electrons onto the nightside is the other mechanism that is often considered (Gringauz et al., 1979). The lack of this process in the physics for V-GITM may explain why the observed peak is not matching, but is beyond the scope of this paper.

4.4 Conclusion

This paper introduces the main features of a new Venus global circulation model of the ionosphere-thermosphere region. The new model, V-GITM, is based on the terrestrial GITM model (Ridley et al., 2006) and Mars counterpart (Bougher et al., 2015b). V-GITM utilizes Venus specific parameters and physical processes from several existing Venus codes, including the Venus Thermosphere General Circulation Model (VTGCM) and LMD-IPSL's V-PCM. V-GITM self-consistently solves for the neutral densities, winds, and temperatures as well as the ion and electron densities, and the ion velocities while assuming a partially dynamical ionosphere. Overall, this is the first Venus model to couple the ionosphere-thermosphere without assuming hydrostatic equilibrium and uses chemical heating to correctly approximate energy depositing from the solar EUV.

Comparisons between the model results and a wide range of neutral and ion measurements across a variety of local times are shown. Dayside neutral temperature and bulk density structure of the upper atmosphere match reasonably well, although species-specific densities do not always match other models' predictions. Neutral winds are shown including a variety of retrograde super-rotating zonal flow speeds demonstrating the strong influence on neutral wind profiles up to 100 km, but having a relatively minor impact on wind speeds in the upper thermosphere and dayside temperatures. Finally, V-GITM explored the ion velocities and nighttime ionosphere that forms from only the advection of O_2^+.

Introducing V-GITM, with all of its features, allows the Venus modeling community to perform more insightful model-model comparisons to determine the importance of a hydrostatic solver, ion dynamics and exothermic heating. Further work is needed for all Venus models to improve

upon inaccurate approximations or parameterizations of the physics implemented. Processes like eddy diffusion, 15 μm CO_2 cooling and solar IR heating are complicated to correctly model alone are thus parameterized, which makes them highly uncertain. It is understood that each of these significantly affect Venus' thermosphere and so future studies about quantifying the uncertainty of these terms is an important topic so that this model can be a useful tool for future Venus studies, particularly with the upcoming VERITAS and DAVINCI missions scheduled.

4.5 Open Research

V-GITM is freely available through GitHub (Ridley et al., 2023). Plotting routines and data within this work will be published on DeepBlue.

Acknowledgements

The research presented in this study was supported at University of Michigan partially by the joint NSF-NASA Space Weather with Quantified Uncertainties program under NSF grant number 2028125 and NASA grant number 80NSSC20K1581. This work was also supported by the NASA grant 80NSSC19K0562. This research has made use of the NASA Exoplanet Archive, which is operated by the California Institute of Technology, under contract with the National Aeronautics and Space Administration under the Exoplanet Exploration Program.

CHAPTER 5

The Venus Global Ionosphere-Thermosphere Model (V-GITM) II: Quantifying the Effect of Energy Sources

5.1 Introduction

Accurate general circulation models (GCM) can greatly assist in the interpretation of planetary atmosphere data. Models typically provide four dimensional state variables which provide a global context for the often limited satellite observations. This is ideally done by correctly implementing equations that accurately and completely capture all dynamics, boundary conditions and drivers within the model. In practice, the models use approximated physics that may be for computational efficiency or because of scientific misunderstandings which lead to inconsistencies with model simulation results when compared to direct measurements.

Earth's atmosphere is the most studied planet due to a combination of convenience and interest. There are many satellites in varying orbits gathering information for comparison. Earth GCMs are typically the building blocks when developing models of other planetary atmospheres. This is done because much of the physics can be carried over directly, but with that also comes model bias. Bias at Venus is more difficult to quantify than at Earth due to the lack of direct measurements of Venus' atmosphere. This makes studying the uncertainty in a Venus model an important topic. Further, planetary models can forecast mass densities of an aerobraking or entry, descent and landing mission. Temperatures and mass densities are highly correlated adding to the importance of accurate heating representations and uncertainty quantification.

Uncertainty quantification involves identifying sources of uncertainty, such as model assumptions, parameterizations, and coefficients, and using statistical or computational methods to estimate the range of possible outcomes and the likelihood of different outcomes. Uncertainty quantification work has been performed at Earth to improve the reliability and decision-making capabilities of the terrestrial GITM model (Pawlowski and Ridley, 2009). The Venus Global Ionosphere-

Thermosphere Model (V-GITM) is used in this study to investigate the effect of modifications in the implementations of solar EUV, solar near IR, eddy diffusion coefficient, radiative cooling in the lower thermosphere, and thermal conduction.

Radiation in the solar infrared (IR) is absorbed by CO_2 atmospheres particularly well at 2.7 μm and 4.3 μm. The efficiency of IR absorption depends on the CO_2 density, solar inclination, and intensity of the incoming radiation. A physics-based approach to estimating the IR heating would involve solving the radiative transfer equations that include absorption, scattering, and emission. Some of the detailed information necessary for performing such a calculation is (1) reliable measurements of the top of atmosphere flux at near IR wavelengths, (2) corresponding CO_2 absorption cross-sections for multiple isotopes, (3) tracking of vibrational states and energy exchanges between the various state-state (thermal, vibrational, rotational) collisions, and (4) an accounting for the difference in LTE and non-LTE effects to name a few. This is a large undertaking by itself and to couple it an IT model would significantly add to the computation time and overall complexity of the model.

The Institut Pierre-Simon Laplace's (IPSL) Venus Planetary Climate Model (V-PCM) is a popular model, but has recognized the benefit of simplifying the near IR heating into a parameterization primarily dependent on pressure and solar zenith angle. Work from (Gilli et al., 2021) updated parameterization constants to yield heating rates and shapes for the solar IR to rectify V-PCM's data-model temperatures differences. The new heating rates are inconsistent with heating rates from (Roldán et al., 2000)'s radiative transfer model. Measurements from VIRTIS-H show large uncertainties in the temperature between 105-145 km making the differences reasonable. Furthermore, the near IR parameterization utilizes a cosine solar zenith angle function which would be inconsistent with our understanding of the deposition of solar irradiance which has shown to have non-zero heating at the terminators Smith and Smith (1972). Seeing as the origin of both the EUV and near IR is the same, it would be expected that the geometry/mechanisms to deposit the energy would be similar. While the effects of varying the dayside heating rate magnitude have been studied (Gilli et al., 2021), the terminator differences in the two methods are unclear.

After energy is absorbed in the near IR, CO_2 atoms can become excited and undergo a de-excitation process also emitting energy at 15 μm (Dickinson, 1976; Fox and Bougher, 1991). Venus' atmosphere is transparent to this energy wavelength and so the energy is lost to space. The best way to capture the LTE cooling is to use a full radiative transfer model which tracks radiative absorption, emission and scattering like Haus et al. (2015) and Roldán et al. (2000). Radiative transfer models typically are not implemented in 3D GCMs due to the high individual computational costs of the radiative transfer model. Many models attempt to capture this process as a form of CO_2 cooling. It has been show to be an important term to balance a large span of altitudes in Venus' thermosphere (Chapter 4 of this thesis, Bougher et al. (1999)). Implementing a comprehen-

sive CO_2 cooling scheme is still an ongoing process. The thermosphere is in a state of non local thermodynamic equilibrium (non-LTE) which the existing 15 μm CO_2 cooling scheme attempts to capture (Bougher et al., 2017; González-Galindo et al., 2013; Gilli et al., 2017, 2021). The 15 μm CO_2 implementation was added to V-GITM, but is limited due to the dependence on pressure levels, temperature differences, and O number densities. For unclear reasons, the approximations break down in the lower thermosphere where LTE effects become significant. To compensate for this, Chapter 4 implemented a numerical scheme to provide a reasonable cooling rate below 100 km.

Eddy diffusion is a way to express the turbulent mixing of the atmosphere. At Earth, it is still highly uncertain (von Zahn et al., 1980; Pilinski and Crowley, 2015; Malhotra and Ridley, 2020; Mahieux et al., 2021). The balance of eddy diffusion and molecular diffusion dictate the homopause location. Further, the turbulent mixing enters all of the transport equations, effecting the density, momentum and energy directly. Indirectly, these equations are coupled, so changes in the eddy diffusion coefficient can have non-linear effects on the entire system. There are effects on the neutral densities, neutral temperatures and electron densities. At Venus, Mahieux et al. (2021) built a 1D profile of the eddy diffusion coefficient based on CO measurements from the SOIR mission. Due to the innate global circulation in 3D models, the necessity of additional turbulent effects using an eddy diffusion coefficient is less compared to 1D models, making it incorrect to translate 1D profiles into 3D models effectively (Bougher et al., 1999). M-GITM has used a variable eddy diffusion coefficient between 500-1,000 m^2s^{-1} that increases the coefficient with altitude (Bougher et al., 2015a). This method is used in both the VTGCM and Tohoku University's GCM although the bounds for K_{min} and K_{max} vary. Instead of applying this during the development of V-GITM, a constant value of 300 m^2s^{-1} was used instead for the work in Chapter 4. VTGCM varies the eddy diffusion coefficient between 10-1,000 m^2s^{-1} (Brecht et al., 2012) and TUGCM uses a coefficient that varies between 0-500 (Hoshino et al., 2012).

The choice of eddy diffusion coefficient and the implementation of other energy terms affect temperatures, pressure gradients and consequently wind speeds. It is therefore important to provide boundaries for these parameters to constrain horizontal wind speeds. Navarro et al. (2021)'s work insinuates the presence of a normal shock in the nightside thermosphere above 130 km. The shock-like feature is assumed due to the presence of Mach number greater than 1 and slowing to subsonic speeds within $\sim$500 km. This has been explored with V-GITM and similar results have been found. If it is found that the energy balance should be varied, this helps determine if the theory of Venus' shock formation is appropriate.

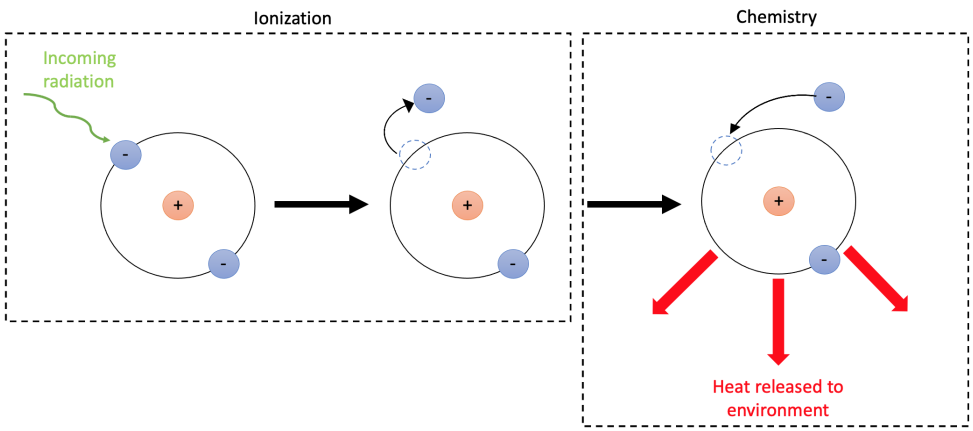

Figure 5.1: An illustration of how incoming radiation heats the atmosphere. On the left, incoming radiation ionizes a neutral particle creating a free ion and electron. A pair of charged particles undergo a chemical reaction that heat the surrounding environment.

A significant driver of the thermosphere at planets that maintains an atmosphere and ionosphere is the absorption of solar EUV. A popular implementation of capturing the effects of the solar EUV is to use top of atmosphere fluxes and transmit them through the atmosphere allowing absorption via forms of direct heating, ionization and dissociation of the neutral population. A fraction of the total incident energy gets absorbed as kinetic energy (direct heating). Following previous studies of the Venus heating efficiency (Fox, 1988) (Hollenbach et al., 1985), nearly all Venus GCMs use a constant heating efficiency of 10-25% to approximate all of the direct and indirect heating processes. A more accurate representation of the heating due to EUV radiation absorption is through the ionization of many different neutral species and tracking of the consequent chemistry. When ions chemically react to become neutral (through charge-exchange, electron recombination, etc...), these reactions are often exothermic. This is the means that the chemical reactions produce heat for the surrounding atmosphere. This process is illustrated in Figure 5.1. In reality, this is also an approximation due to the creation of photoelectrons which complicates the tracking of energy in the chemical processes (Richards et al., 2006; Richards, 2022).

The effects of solar EUV, solar near IR, CO_2 in the LTE region, and eddy diffusion are explored in this work. Global temperature changes, among other state variable changes, for varying implementations of these parameterizations are believed to be affected. Additionally, heating efficiencies that approximate V-GITM's solar EUV deposition through direct heating, chemical heating and photodissociation heating are computed for solar minimum, solar medium and solar max conditions. Due to the large uncertainty and influence the eddy diffusion coefficient and solar IR have on the thermosphere, these are explored in more detail.

5.2 Model Conditions

5.2.1 Recent Model Improvements

Incoming photons with energies greater than the dissociation threshold contribute to local heating (Fox, 1988; Gu et al., 2020). V-GITM assumes the dissociation threshold of CO_2 is 5.453 eV (Shaw et al., 1995), and that 66% of the energy in excess of the dissociation threshold is deposited into the atmosphere as heating:

$$Q_{diss}(z) = 0.66 \sum_{\lambda} (E_\lambda - E_0) P(\lambda, z) \tag{5.1}$$

This is discussed in (Dickinson, 1976; Fox, 1988) as the fraction deposited as translational energy. The remaining 34% is assumed to be partitioned in rotational and vibrational energies which do not directly contribute to the heating. These fractions are highly uncertain. They vary based on wavelength and the resulting excitation state and so the method applied within V-GITM is a simplification of the radiative process. From equation (5.1), Q_{diss} is the heat accumulation from excess dissociation, λ is the photon wavelength ($\sim$85-190 nm), E_λ is the energy of an incoming photon which is greater than the dissociation threshold, E_0. P(λ) is the CO_2 dissociation production rate at a specific wavelength and is given by:

$$P(\lambda, z) = I(\lambda, z)\sigma(\lambda)n \tag{5.2}$$

where I is the attenuated intensity, σ is the CO_2 dissociation cross-section, and n is the species-specific number density. In this case, it is only for CO_2. CO_2 dissociation can be dissociated at wavelengths greater than 190 m, but this is the current upper limit of the wavelength range within V-GITM. The lower spectral bin, 85-90 nm, is the highest energy photon allowed to add excess dissociative energy, because at higher photon energies, ionization will occur instead. These quantities will be extrapolated in future work to be computed for species like O_2, N_2 and CO.

V-GITM also recently added neutral helium, with a lower boundary condition of 5×10^{11} cm^{-3}. The number density is initialized following a hydrostatic profile. He is chemically inactive within V-GITM, but a good tracer of dynamics, eddy diffusion and global winds (von Zahn et al., 1980). The response of n_{He} to eddy diffusion is examined in section 5.3.3.

5.2.2 Other Heating Sources

The Venus Global Ionosphere-Thermosphere Model (V-GITM) is used to perform the simulations. V-GITM is a 3D spherical model that uses the Navier-Stokes equations to solve for the state variables. It is a unique Venus model due to the ability to directly solve the neutral vertical momentum

equation for the vertical velocities. Additionally, the solar EUV heating effects are computed through chemical reactions with a much smaller direct heating efficiency of 1%.

The vertical energy equation for the normalized neutral temperature ($\mathcal{T} = kT/\bar{m}_n$) is:

$$\frac{\partial \mathcal{T}}{\partial t} + u_r \frac{\partial \mathcal{T}}{\partial r} + (\gamma - 1)\mathcal{T}(\frac{2u_r}{r} + \frac{\partial u_r}{\partial r}) = \frac{k}{c_v \rho \bar{m}_n} Q \tag{5.3}$$

where u_r is the vertical velocity, r is the distance in the radial direction, γ is the adiabatic index that is attached to the change in energy from the expansion of the gas, c_v is the specific heat constant for a fixed volume, k is Boltzmann's constant, ρ is the mass density, and $\bar{m}$ is the mean mass.

The various source terms are given by:

$$Q = Q_{EUV} + Q_{IR} + Q_O + Q_{CO_2} + Q_{CHEM} + Q_{diss} + \frac{\partial}{\partial r}((\kappa_c + \kappa_{eddy})\frac{\partial T}{\partial r}) \tag{5.4}$$

where Q_{EUV} and Q_{IR} are the contribution from the Sun's extreme ultraviolet and infrared wavelengths, respectively. The Q_O and Q_{CO_2} are terms detailing the radiative cooling to space from the 63 μm and 15 μm bands, respectively. Q_{CHEM} combines heat generated from all exothermic reactions. κ_{eddy} is the heat conductivity due to eddy diffusion coefficient and κ_c is the molecular heat conductivity.

In this work, variations on the source terms simulating the eddy diffusion, EUV heating, LTE CO_2 cooling, near IR heating and thermal conduction coefficients for CO_2 as described by parameter changes in Table 5.1. The effects of each of these uncertain terms are investigated to determine the importance in determining the structure and dynamics of Venus' upper atmosphere. The eddy diffusion coefficient is changed to explore its importance in the temperature structure as well as its role in the composition. A factor of three larger and smaller from the value used in Chapter 4 was used to modify the eddy diffusion coefficient to understand both the effects of a smaller eddy diffusion coefficient that is more representative of the eddy diffusion coefficient values used in the Earth version of GITM (Ridley et al., 2006) and a higher which pushes the boundary towards a used value in 1D Venus modeling (Mahieux et al., 2021).

Differences in EUV heating are performed using the Flare Irradiance Spectral Model (FISM) fluxes (Chamberlin et al., 2008) from Oct. 1st-10th, 2011 (solar moderate conditions) with a flat 20% heating efficiency, a 1% heating efficiency coupled with the heat generated via exothermic chemistry, and the summation of 1% heating efficiency, exothermic chemistry and photodissociation heating.

Below $\sim$100 km, the non-LTE CO_2 cooling model approximations break down due to being in a LTE-dominated region, so it is unclear how to account for this. In this study, the LTE CO_2 cooling is numerically applied by extrapolating from the non-LTE value at 10^{-2} Pa to the bottom

boundary of the model via a linear or logarithmic method. Additionally, one of the extrapolations is done to mimic the cooling rates shown in Haus et al. (2015). While these variations are not large, there is almost no heating to balance it. Near IR heating is implemented using the parameterization schemes as shown in (1) Gilli et al. (2017), (2) Gilli et al. (2021) and (3) the radiative transfer of 2.7 μm and 4.3 μm waves absorbed directly by CO_2 given an intensity at the top of the atmosphere and a set of cross-sections. This allows for the treatment of IR heating across the terminators where the Sun is still shining. Finally, the thermal conduction coefficient of CO_2 is increased to best fit the recommended thermal conduction values from Huber et al. (2016). The goal of these simulations is to show how uncertainty in each energy term affects the results.

5.3 Results

A variety of source terms were modified according to the Table 5.1 during October 1st-10th, 2011 which is representative of solar moderate conditions as described by the F10.7 and 90-day average, F10.7a (Figure 5.4). A summary of all the individual impact of varying the source term is shown in Figure 5.2. The Eddy 1, EUV 1, 15 μm 1, and IR 1 are the baseline parameters used in all simulations unless otherwise specified. For example, the eddy diffusion coefficient was 300 m^2 s^{-1} in all runs except Eddy 2 and Eddy 3. Results are shown as a function of altitude, which is V-GITM's neutral coordinate system, and pressure, which is used by most models, and can therefore be directly compared.

Varying the total EUV scheme between the V-GITM configuration from Chapter 4 (EUV 2), the latest V-GITM configuration (EUV 1), and a representative method in other models (e.g. 20% fixed heating efficiency) has large temperature differences near the top of the model. While there is almost no effect below 140 km, the three simulations vary dramatically above this. With an expected temperature of approximately 240 K (Hedin et al., 1983), the EUV 1 is closest. As seen when comparing EUV 1 to EUV 2, adding excess photodissociation heating increased the globally averaged temperature from 220 K to more than 240 K at 170 km. This is a large increase in temperature that creates dayside temperatures exceeding the results from VTS3. We believe this adds importance to re-examining the thermal conduction and non-LTE CO_2 cooling adjustments which are particularly important in balancing the heat in this part of the atmosphere.

The near IR parameterization had some effect on the temperature through nearly the entire domain. The largest temperature differences were near 120 km and at 170 km. At 120 km, the non-LTE cooling experiences a minimum which is ultimately responsible for the local temperature maxima. An exploration on the solar IR parameterization into specifically the dayside, terminator and nightside temperatures are discussed in section 5.3.4.

The 15 μm cooling variation runs drive dramatic changes to the temperature throughout the

Parameter	Formulation	Label
Eddy diffusion coefficient	Flat 300	Eddy 1
	Flat 100	Eddy 2
	Flat 900	Eddy 3
EUV model	FISM (1%) + Chemical + Dissociation	EUV 1
	FISM (1%) + Chemical	EUV 2
	FISM (20%)	EUV 3
LTE CO_2 cooling	Linear	15 μm 1
	Logarithmic	15 μm 2
	Linear (Haus et al., 2015)	15 μm 3
Near IR heating	V-GITM I (Chapter 4)	IR 1
	(Gilli et al., 2017)	IR 2
	(Gilli et al., 2021)	IR 3
Thermal conduction	A_{CO_2} = 0.82$\times 10^{-5}$ (Schunk and Nagy, 2004)	Conduction 1
	A_{CO_2} = 1.1$\times 10^{-5}$ (Huber et al., 2016)	Conduction 2

Table 5.1: Parameters in V-GITM that have an effect on the thermospheric temperature along with the values used for this study.

entire domain. From 70-100 km, the temperature changes respond proportionally to the way the cooling term was modified. For example, the logarithmic run (15 μm 2) has the largest temperatures in up to nearly 120 km. This is due to the fact that the logarithmic extrapolation of NLTE CO_2 cooling value near 100 km decreases much faster than a linear extrapolation, creating a much weaker cooling term from 70-100 km. It is interesting that the temperature above 140 km is the lowest in that same run. The reason for this is still unclear.

The eddy diffusion coefficients changed the temperature below 105 km. V-GITM showed that lower eddy diffusion correlates to lower temperatures in the lower thermosphere. It is interesting to note that the lower temperatures do not significantly modify the average temperature structure above 105 km which is different than the behavior exhibited in the varied NLTE cooling runs. They cause minor deviations, but the temperature variations below 105 km are small compared to the CO_2 cooling changes.

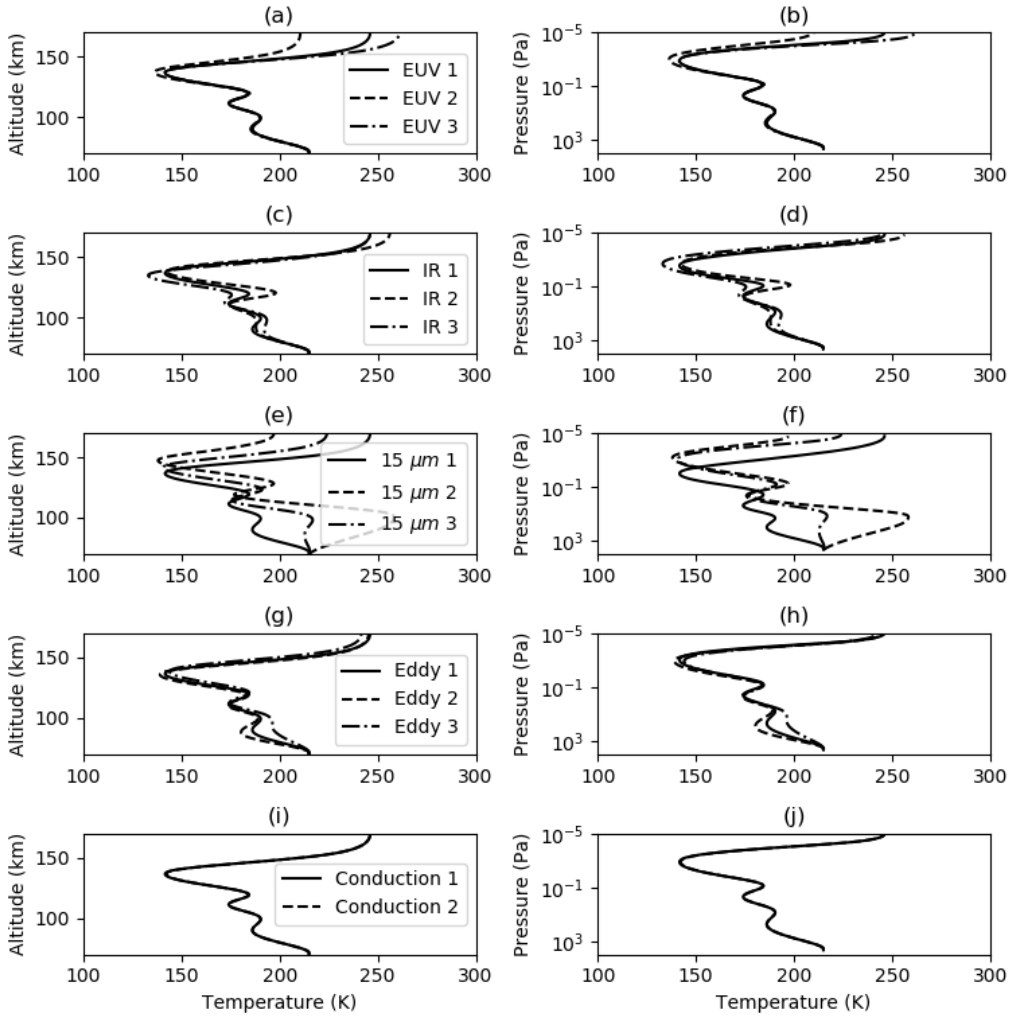

Figure 5.2: Global average temperature for solar moderate conditions. Each panel shows a comparison between the different values in each parameter category which are plotted as a function of altitude (left column) or pressure (right column).

As pointed out in Chapter 3, thermal conduction is another uncertain term. GITM and V-GITM adopted (Schunk and Nagy, 2004)'s parameterization to calculate thermal conductivity:

$$\kappa_c = \sum_{i=CO_2,N_2,O} [\frac{N_i}{N_{total}}] A_i T^{s_i} \tag{5.5}$$

using the major neutrals at the top and bottom of the model domain. Recommended values of A_i and s_i are shown in Table 10.1 of (Schunk and Nagy, 2004). A sensitivity study on the 'A' and 's' parameters for N_2 and O have been a previously studied topic (Pawlowski and Ridley, 2009). For this reason, this study focuses on the A_{CO_2} coefficient.

A compilation of experimental values for the thermal conductivity of CO_2 at pressure levels

from 0-200 MPa and temperatures from 50-1100 K are shown given in Poling et al. (2001); Huber et al. (2016). The limits of this testing largely exceed the thermosphere temperatures and pressures of Venus which are in the range of 100-300 K and 10^{-10}-10^{-2} MPa. Despite this, there are 0 MPa recommended thermal conductivities published in a table that we've best-fit the thermal conductivity parameterization shown in equation 5.5. The change in A_{CO_2} from 0.82e-5 to 1.1e-5 theoretically works well, this is shown in Figure 5.3.

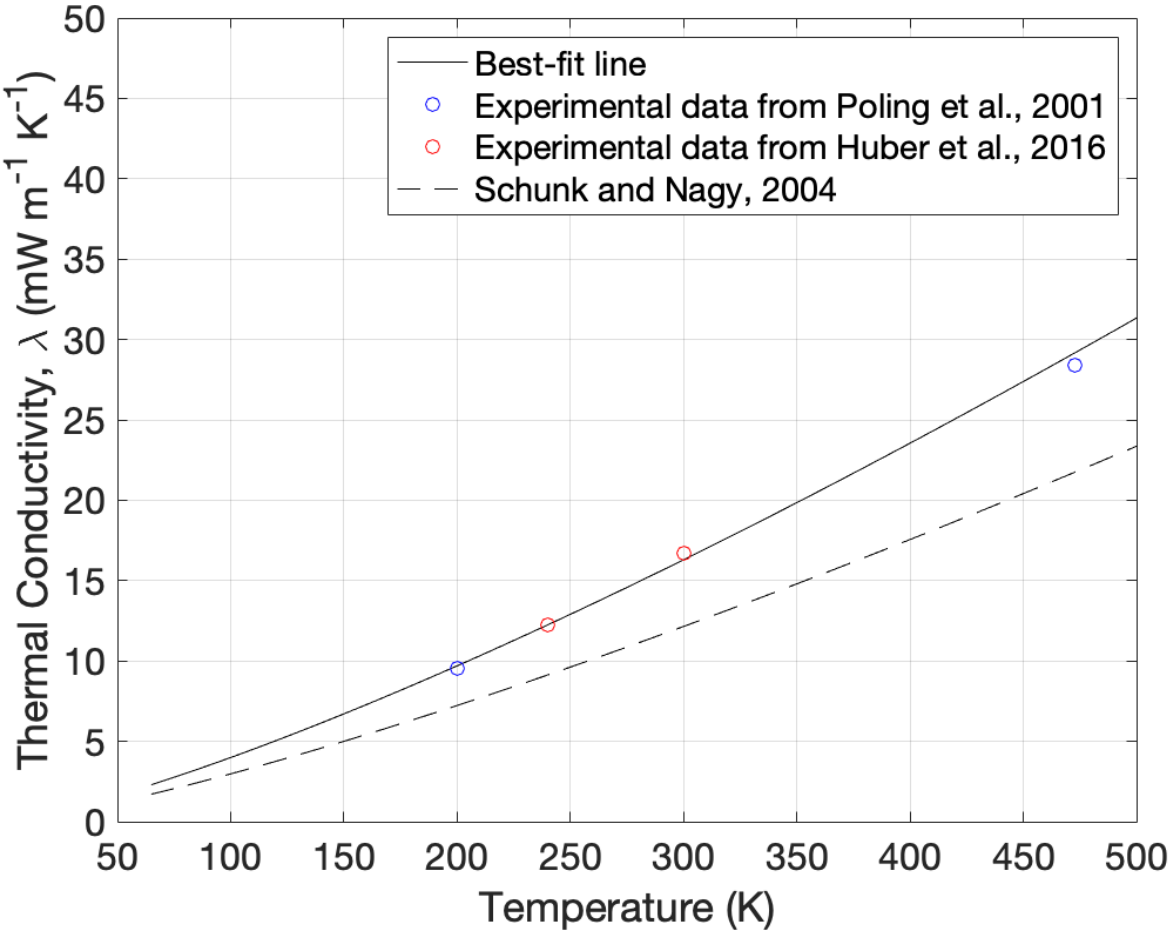

Figure 5.3: Conduction 1 and Conduction 2 CO_2 thermal conductivities plotted as a function of temperature. Two red circles show reference data within the 0 MPa pressure level at 240 K and 300 K from (Huber et al., 2016).

Increasing the thermal conductivity coefficient, A_{CO_2}, increased the vertical transport of heat downward at $\sim$15% larger rate. Despite the increased cooling, the dayside maximum and globally averaged temperature saw essentially no difference (Figure 5.2. It was noticed that the chemical heating rate and thermal conduction maintained a similar net heating rate above 140 km between the Conduction 1 and Conduction 2 runs. Altering the thermal conduction at Venus has almost

no effect on the thermal structure unlike at Earth, where it is extremely important (Pawlowski and Ridley, 2009; Ponder et al., 2023). In addition, this reinforces the importance of CO_2 15 μm cooling at lower thermospheric altitudes rather than cooling by thermal conduction.

5.3.1 Solar Cycle Variations

This section shows simulations under three runs which are performed during solar minimum, moderate and maximum conditions using the same parameters in Table 5.1, EUV 1. Although FISM from 0.1 nm - 190 nm is used, F10.7 and F10.7a are nice proxys for getting an idea of what the sun is doing in these time periods. These values are displayed in Figure 5.4.

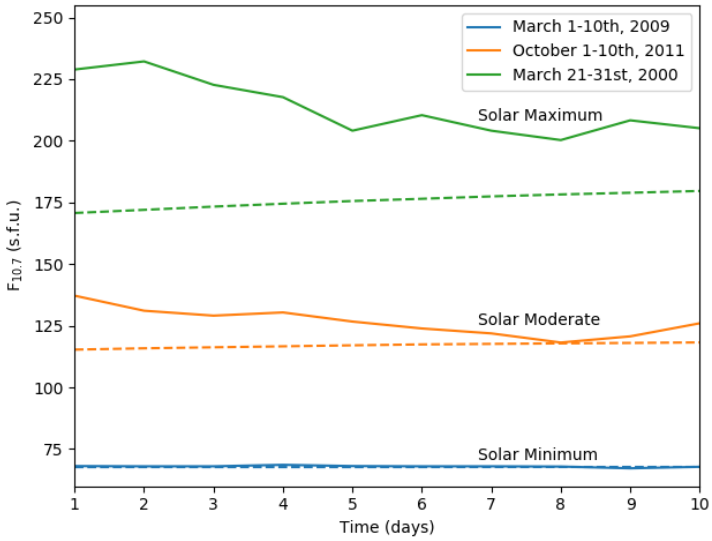

Figure 5.4: F10.7 (solid lines) and F10.7a (dashed lines) for the time periods explored in this work.

Figure 5.5 shows altitude profiles of globally averaged mass densities, max horizontal wind speeds and temperature at the end of the different ten day periods. Mass densities increase by more than 150%, which is an effect of uplifting of the atmosphere due to the increased temperature. Horizontal winds speeds are primarily a balance of gradient pressure and viscosity so that when the temperature and density increase on the dayside, the gradient in pressure increases, driving stronger winds. Maximum winds typically occur near the evening terminator and this varies from 410 m/s to 450 m/s at 170 km. The globally averaged temperatures drastically change from 220 K to 265 K due to the increase in solar EUV. Below 140 km there are no noticeable changes due to the dominant thermodynamic terms, like solar IR and radiative cooling, not changing with solar conditions.

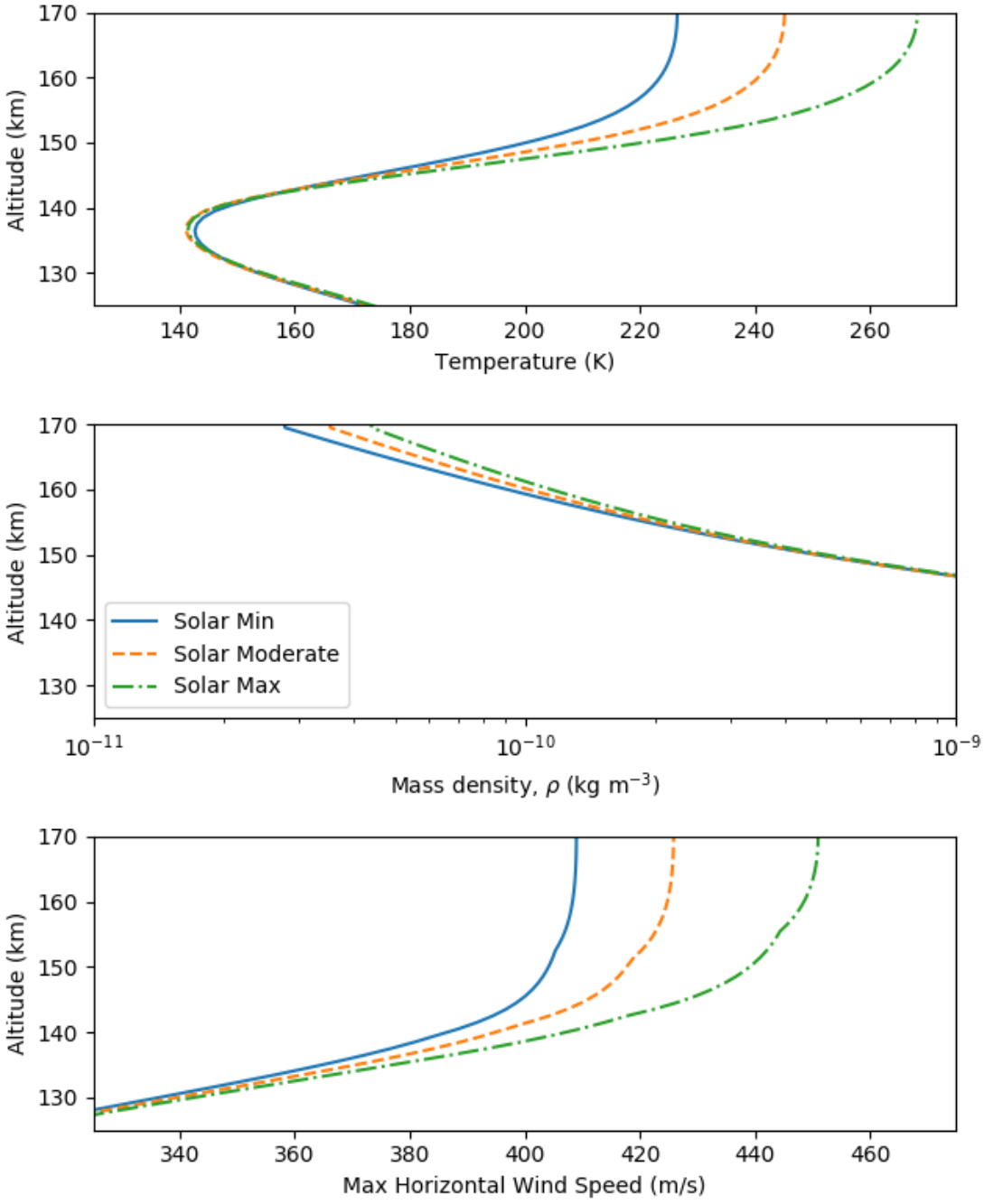

Figure 5.5: Globally averaged mass densities (top), maximum horizontal wind speeds (middle), and globally averaged temperatures (bottom) for different solar conditions.

Figure 5.6 shows how the chemical heating, photodissociation heating, FISM, NLTE CO_2 cooling and thermal conduction vary between solar conditions. Chemical heating varied from roughly 3,500-6,000 K/day, excess photodissociation varies from almost 2,000-3,000 K/day, and 1% of FISM is 270-505 K/day. In sum, these are the total heating effects other Venus GCMs often sim-

plify through the use of a heating efficiency which has been summarized to be 10-20% and through non-FISM, EUV models (Martinez et al., 2021). The equivalent EUV heating these models would receive is 2,700-5,400 K/day for solar minimum or 5,050-10,100 K/day for solar maximum. More analysis of the heating efficiency and an estimation of the ”effective” heating efficiency is discussed in section 5.3.2. The near IR is a major heating source but is not plotted because it has no variability with solar cycle.

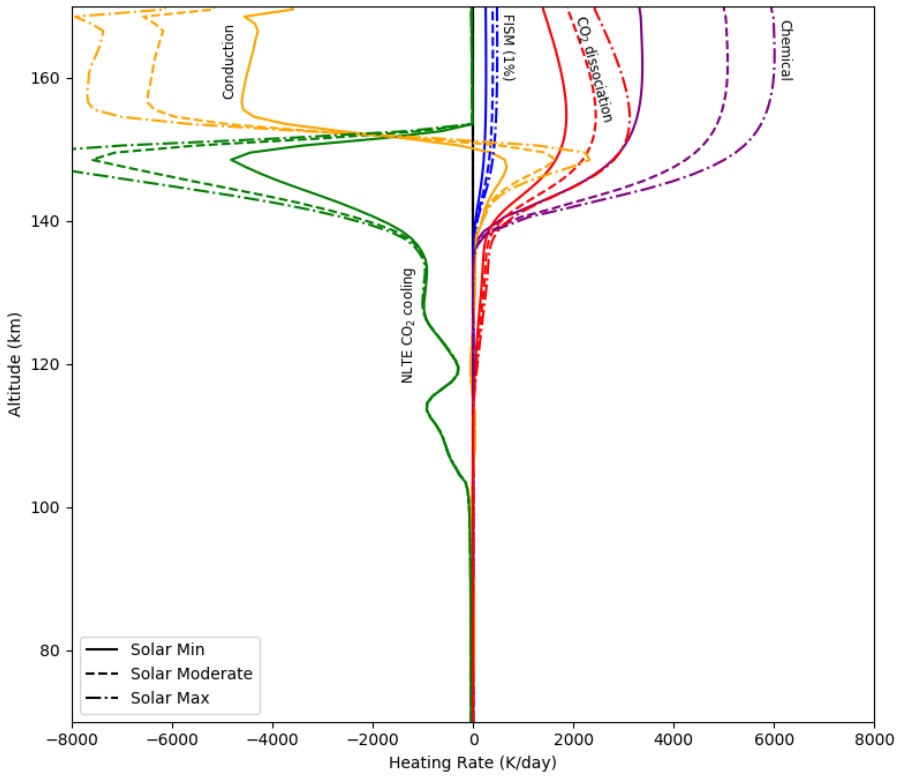

Figure 5.6: 12 LST heating and cooling rates for terms for varied terms over run periods shown in Figure 5.4.

5.3.2 Heating Efficiency

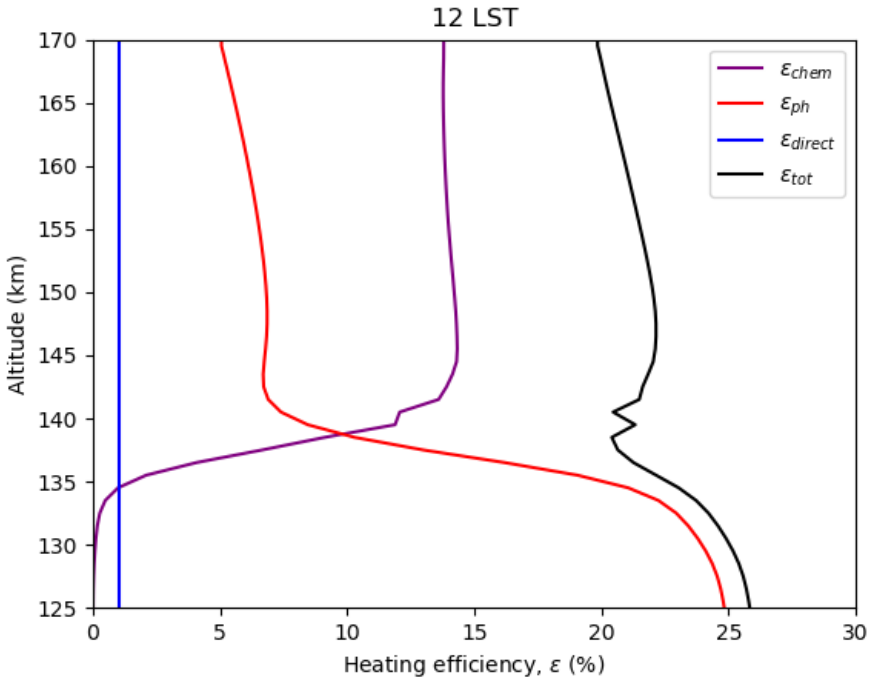

Figure 5.7: Individual heating efficiencies at 12 LST to model exothermic chemistry and photodissociation effects via a single heating efficiency from 0.1-190 nm.

This section explores the "effective" heating efficiency that would be needed within FISM to approximate the cumulative EUV heating processes (1% direct heating, chemical heating and photodissociation of CO_2) used in V-GITM during the EUV 2 run parameters during solar moderate conditions. Figure 5.7 shows the calculated heating efficiency relative to the total available energy near 12 LST. The chemical heating is nearly constant above 140 km contributing about 12-14% of the heating efficiency. Photodissociation of CO_2 takes over and peaks at nearly 25% at 125 km. Below 140 km, the intensity of EUV is very low and so not much heating is added despite the large heating efficiency. 1% is added to the total heating efficiency to account for the 1% EUV direct heating. Although not shown, the heating efficiencies were calculated for solar minimum and solar maximum conditions and found the total heating efficiency to be within 17-20%.

Fox (1988) has vertical profiles of Venus heating efficiencies from 115-200 km. These profiles are uncertain and have lower limit and best guess values that vary from 16% to roughly 25% within V-GITM's vertical domain. V-GITM's results are not largely different from Fox's work except below 135 km where the total EUV heating efficiency within V-GITM is approximately 5-10% larger than Fox's work.

Hollenbach et al. (1985) performed a 1D simulation finding heating efficiencies between 10-15% due to photodissociation, photoionization and photoelectrons and chemistry. Gu et al. (2020) detailed a heating efficiency calculation for Mars finding cumulative heating efficiencies near 20%, including photon impact and photoelectron effects. Although their work is for Mars, due to the similarities in CO_2-based planets, the chemistry and EUV deposition may be similar enough that it may help to provide understanding as to why the heating efficiencies are mismatched between what is presented here and what is widely accepted in other GCMs. While V-GITM ignores photoelectron heating, this has been shown to be a small term for Mars (Gu et al., 2020). This is a topic of future work to confirm its relative impact for Venus.

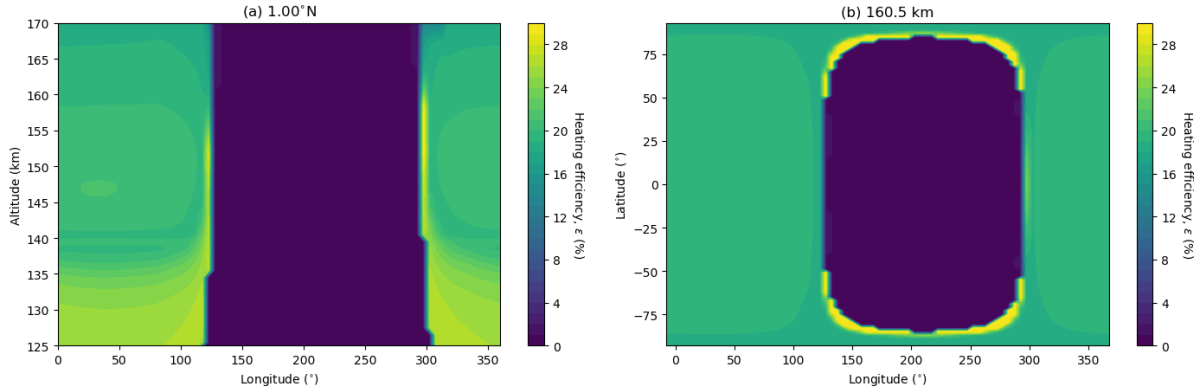

Figure 5.8: Top panel: Effective heating efficiency at equator to model exothermic heat generation due to chemistry via FISM from 0.1-190 nm. Bottom panel: Local noon, 1D heating efficiency profile between 125-170 km. Note: The heating efficiency is reported as zero when there is no heating at all, such as the night side.

Figure 5.8 shows that there is spatial variability in the heating efficiency, as shown in the slice at 1°N and at 160.5 km. As shown in Figure 5.7, there is more vertical variation in the heating efficiency where above 135 km have the greatest seperation from a uniform profile. The reason for the spikes in computed heating efficiency at the terminators is due to the total EUV heating in these cells being close to zero. Overall, there is little variation of the heating efficiency at a constant altitude when only the dayside is considered.

5.3.3 Eddy Diffusion Coefficient

In Chapter 4, the eddy diffusion coefficient was applied uniformly across the model domain at a constant value of 300 m^2 s^{-1}. This section explores the impact of increasing and decreasing the coefficient by a factor of three to 100 and 900 m^2 s^{-1}. In Figure 5.2, the eddy diffusion primarily effects the temperature between 70 and 100 km altitude. At 70 km, the temperature is a constant

value of 215 K. The eddy diffusion increases the thermal conduction below ∼115 km, therefore, increasing the eddy diffusion coefficient raised the temperature between 70-115 km, since the boundary acts as a heat source. A data-model comparison of runs with constant eddy diffusion coefficients of 100, 300, and 900 is shown in Figure 5.9. The eddy diffusion coefficient affects the globally-averaged CO number densities up to almost 115 km. In Figure 5.9, V-GITM CO profiles are shown against the SOIR measurements over the 2007-2014 time period. According to Mahieux et al. (2021), CO is supposed to be driven by the dynamics due to its low chemical activity. It seems that V-GITM's molecular diffusion or chemical reactions must drive the number density above 115 km.

The corresponding V-GITM and Pioneer Venus measured helium profiles are shown in the right subplot. Each run was initialized with a value of 5×10^{11} cm^{-3} at 70 km. Near 130 km, the densities transition into region dominated by molecular diffusion where the densities fall off is determined by the helium scale height. The differences in density are due to the different locations of the homopause which increase with altitude as the eddy diffusion coefficient is increased. A higher homopause altitudes allows the bulk scale height to act on the helium to higher altitudes in the atmosphere causing a faster fall off of the number density. As (von Zahn et al., 1980) demonstrated, it is possible to tune the eddy diffusion coefficient to match Pioneer Venus' measurements of the helium densities, but should be cautiously done due to the uncertainty in the lower boundary condition number density which also has a strong influence on the overall helium density. Further, the densities at the top of the model are driven by the temperature structure in the entire model domain.

The eddy diffusion coefficient further affects the neutral temperature and strength of eddy viscosity. Raising the eddy diffusion coefficient causes increased viscosity, meaning that the winds would be dragged more towards lower boundary condition velocities. Figure 5.10 shows the wind speeds for eddy diffusion coefficients of 100, 300 and 900 m^2 s^{-1} at 90.5 km, 105.5 km, and 160.5 km. At 90.5 km, the winds follow the RSZ pattern implemented at the bottom boundary.

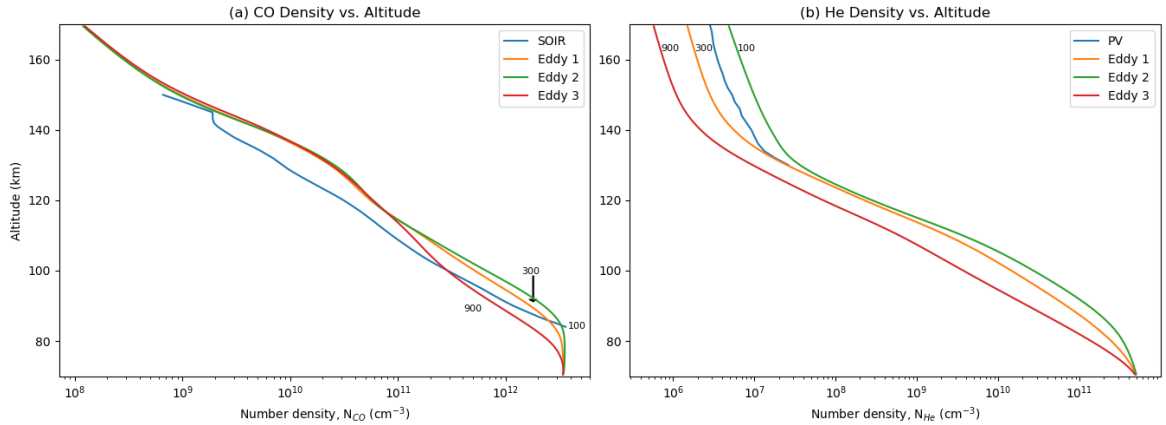

Figure 5.9: Three V-GITM runs with differing eddy diffusion coefficients (300, 100, 900 in that order) against (a) SOIR CO measurements (Mahieux et al., 2021) and (b) Pioneer Venus He measurements (von Zahn et al., 1980).

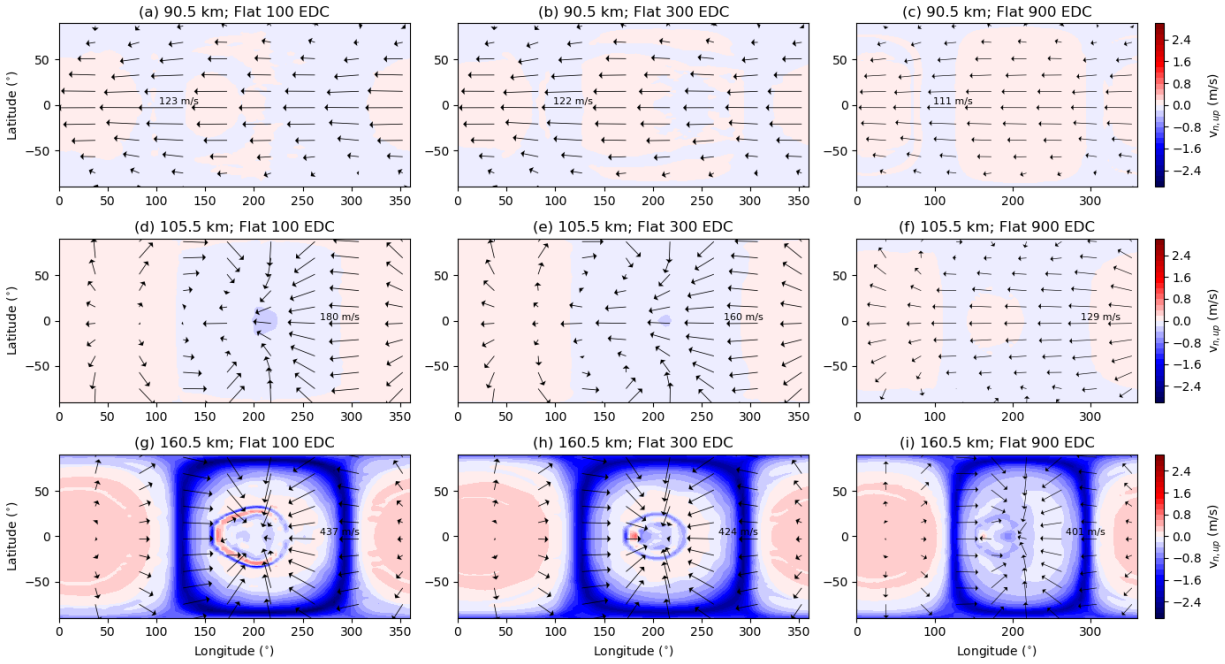

Figure 5.10: Constant altitude slices of horizontal (arrows) and vertical (contours) winds at 90.5 km (first row), 105.5 km (second row), and 160.5 km (final row). From left to right, columns show eddy diffusion coefficient values of 100 m^2/s, 300 m^2/s and 900 m^2/s. Positive vertical wind values correspond to upward motion. Note that the wind vector length scale changes in each plot, while the vertical wind color scale does not change.

At 105.5 km, the wind patterns are very different for different eddy diffusion coefficient values. With 900 m^2 s^{-1}, the wind has many similarities to the RSZ pattern imposed at the lower boundary

condition with similar wind speeds. This is due to the linear scaling of eddy viscosity parameterization with eddy diffusion coefficient (Bougher et al., 1986; Hoshino et al., 2012). When the eddy diffusion coefficient is lowered to 100 m^2 s^{-1} the wind pattern is different. Except at the equator, the horizontal winds flow in a subsolar-to-antisolar pattern which is driven due to pressure gradients from the warm dayside and cooler nightside (refer to Figure 5.11). Eddy viscosity has a strong influence on the location of the "transition region" which occurs higher in the atmosphere as the eddy viscosity is stronger. At 160 km, the winds are inversely proportional to to the eddy diffusion coefficient. The large changes in eddy diffusion change the maximum wind speeds by less than 10%, because the wind speeds at this altitude are largely dictated by the solar EUV's impact on dayside temperatures.

Figure 5.11 shows equatorial slices of neutral temperature for the three runs. The dayside is very similar except below 90 km in the 100 m^2/s run where the temperatures seem to decrease more rapidly from the lower boundary condition, 228 K. The nightside ztemperature is strongly dependent on the eddy diffusion coefficient. Near 100 km, a nightside temperature peak exists in the 100 m^2 s^{-1} run, whereas is disappears in the two larger eddy diffusion coefficient runs. This is due to the strong SS-AS wind structure that is allowed to form because of the lower eddy viscosity. Slightly higher at 120 km, there is another local maximum for the temperature that is evident in all three eddy conditions. SS-AS flow is the wind pattern at this altitude independent of the eddy diffusion strength. For a eddy diffusion coefficient of 900 m^2 s^{-1}, the transition region is below 120 km.

Above 140 km, the nightside is known for being very cold and often called a cryosphere. The different eddy diffusion coefficients change the longitudinal position of the temperature patches in the upper thermosphere. This is believed to be due to eddy diffusion induced temperature changes on the dayside that modify the strength of the pressure gradients that drive the SS-AS winds. As winds are strengthened, the location of adiabatic heating is changed because the nightside convergence location is changed.

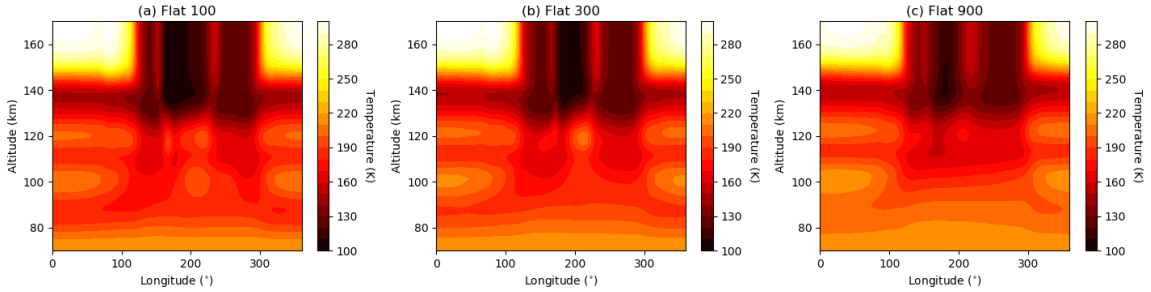

Figure 5.11: Equator slices of temperatures. From left to right, the eddy diffusion coefficient is (a) 100 m^2/s, (b) 300 m^2/s and (c) 900 m^2/s.

5.3.4 Near IR

V-GITM includes two models for the solar near IR: the transmission of radiation directly absorbed (Chapter 4) or the V-PCM's non-LTE parameterization (Gilli et al., 2017, 2021). Martinez et al. (2023) has recently expanded the LMD-PCM's parameterization to a multi-band heating rate, but this has not been tested with V-GITM yet.

Figure 5.12 shows the heating rates as they are deposited in V-GITM for the different IR parameterizations. These methods are compared under solar moderate conditions and should be representative of any solar conditions because there is very little near IR variability from SORCE measurements up to 2400 nm (2.4 μm) (Coddington et al., 2019; Woods et al., 2022). Noon heating rates are shown in Figure 5.12a. V-GITM's transmission method matches the magnitude of heating reported in Gilli et al. (2021), but with a width closer to the Gilli et al. (2017) results. The width is a natural consequence of transmitting radiation through the atmosphere and having it absorbed. Accurately estimating the altitude spread of heating would be better done in a detailed radiative transfer model that captures the line-by-line transmission of radiation, absorption and consequent vibrational excitation and quenching of CO_2. Roldán et al. (2000)'s radiative transfer code was the basis of Gilli et al. (2017)'s parameterization and is the basis for one of the run configurations in this section. As pointed out in Gilli et al. (2021), the 2017 parameters were updated to address data-model discrepancies.

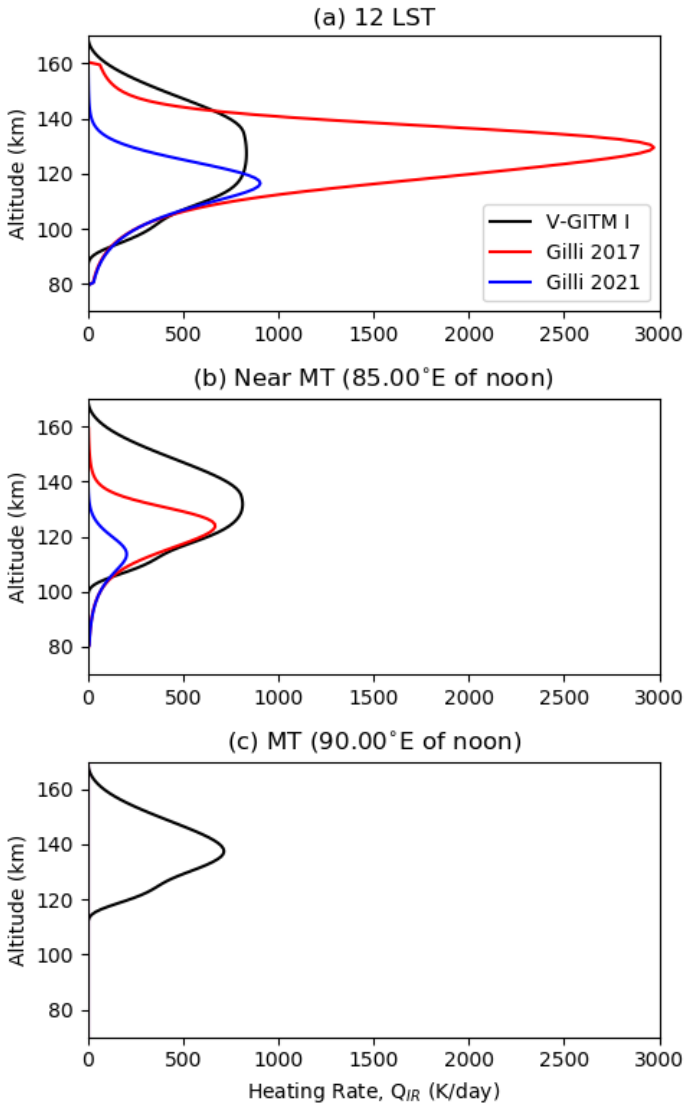

Figure 5.12: Heating rates comparison from solar near IR methods (a) at noon, (b) near the morning terminator, and (c) at the morning terminator.

Figures 5.12b and 5.12c display the rates near the eastward terminator and directly at the terminator to compare heating rates for the different IR methods. Although V-GITM's transmission method does not consider all the IR radiative processes, this method utilizes Chapman integrals and this provides non-trivial heating at and beyond the terminators, much larger than the cosine function used in each of the Gilli papers.

Limaye et al. (2017) compiled the temperature measurements shown in Figure 5.13. V-GITM's corresponding results were added to try to validate the model results. Both nightside and dusk show a peak at $\sim 10^{-2}$ mbars, which is thought to be driven by IR heating in one way or another. Firstly, the 5-7 LT averaged temperature slightly underestimates the temperature near 100 km (10^{-2} mbar)

because the 2.7 and 4.3 μm radiation has been completely attenuated preventing any heating at this altitude. Slightly higher, at 10^{-3}-10^{-4} mbar, the temperature is overestimated. This manifests either due to excessive IR heating or lack of CO_2 cooling. It is our understanding that the CO_2 cooling is underestimating the cooling rate leading to an artificial temperature peak seen both on the dayside and at the terminators.

Regarding the nightside, similar to the 5-7 LT temperatures, errors show up as an underestimation at $\sim 10^{-2}$ mbar and temperature overestimation between 10^{-3}-10^{-4} mbar. The temperature underestimation at 10^{-2} mbar is due to the lack of a SS-AS flow pattern which should converge on the nightside leading to a nighttime temperature peak. This principle is also responsible for explaining the overestimation of temperature on the nightside where an artificial temperature peak exists near 120 km on the dayside, but the winds move in a SS-AS direction that adiabatically heats the nightside (see Figure 5.11b).

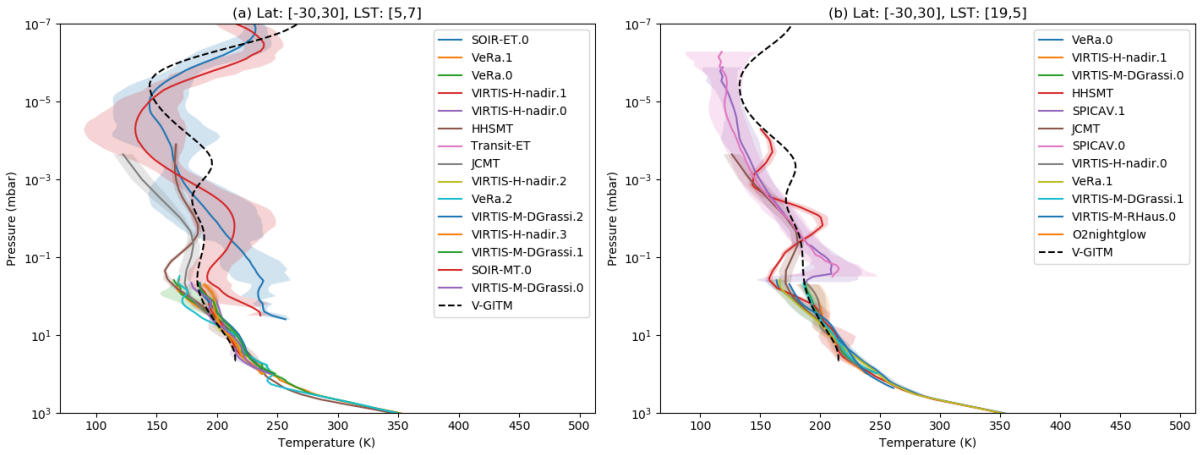

Figure 5.13: Limaye et al. (2017) and V-GITM data averaged between (a) 5-7 LT and (b) 19-5 LT and from 30°S to 30°N latitude.

Net heating (near IR - NLTE CO_2 cooling), temperatures, and pressure scales are plotted in Figure 5.14 for the dayside (first row), terminator (second row) and nightside (final row). It is difficult to predict how the NLTE radiative cooling effects respond to the changing energy balance so the difference of the two are shown in panel (a), (e), and (i). From 160-170 km, the temperatures have differences at each local time. The Gilli 2017 parameterized run is warmest and this is because it has the largest dayside heating rate. The V-GITM I and Gilli et al. (2021) dayside heating rates are similar at all altitudes near noon, but the temperatures are very different. Away from noon, the heating rates are quite different. As seen in 5.12g, the 120 km temperatures are very different and this is due to the difference in heat generated at and beyond the terminator with V-GITM I's use of Chapman integrals.

There are up to 60 K variations in temperature from each method used although the pressure levels are mostly unaffected. This implies that the mismatch of temperature peaks between 10^{-2} mbar and 10^{-4} mbar is unlikely due to altitude-pressure mismatches. The 10^{-2} mbar relates to approximately 105-110 km which is consistent with the approximate altitude shown in the related figures in Limaye et al. (2017). There is a similar net heating applied at 120 km, which we believe is due to a breakdown of the NLTE CO_2 cooling at this altitude artificially heating the dayside at this altitude. The warm dayside will drive warm temperatures horizontally to the nightside where this is mismatching temperature peak is also seen (see Figure 5.13b).

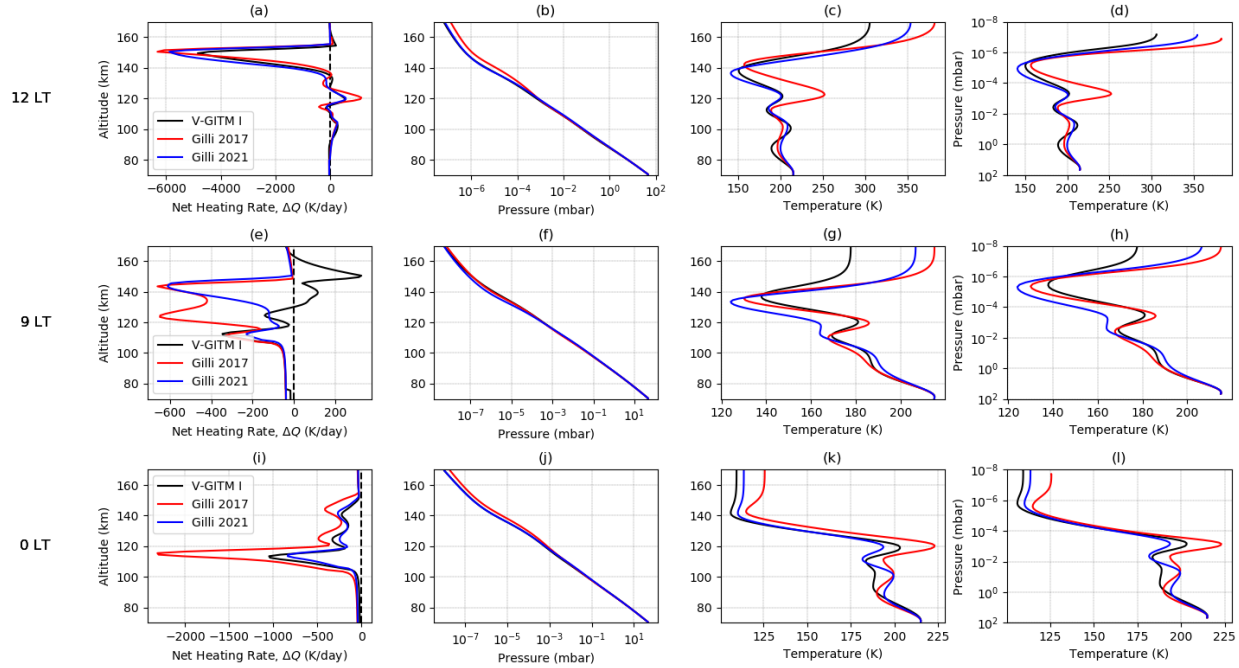

Figure 5.14: Net heating between near IR and NLTE cooling, pressure, and temperatures are shown for three different configurations of near IR. Subplots (a)-(d) correspond to 12 LST, (e)-(h) correspond to 6 LT, and (i)-(l) correspond to 24 LT. The temperature is shown as a function of altitude (c, g, k) and pressure (d, h, l).

5.4 Conclusion

Having a quantified understanding of the uncertainties in a model is crucial when seeking to comprehend the behavior of a system through modeling. V-GITM investigated the solar EUV & near IR, thermal conduction coefficients, eddy diffusion, and lower thermosphere CO_2 cooling. Each source term was modified from the benchmarked values from Chapter 4 based on other published parameterizations. Globally averaged temperatures were displayed in every configuration, while in some instances, additional state variables were also shown. It is shown that uncertainty in

the EUV and lower atmosphere 15 μm CO_2 cooling had the largest impact on the temperatures. Additionally, the same near IR parameterizations were shown to have significant heating near the terminators leading to temperature differences of 20-30 K compared to a method including Chapman-based heat deposition. Furthermore, the eddy diffusion coefficient and its direct proportionality to eddy viscosity had a strong influence on the height of Venus' transition region between RSZ and SS-AS flow patterns. The height of the transition region was shown to be important for determining the existence of nightside temperature peaks.

This work also included a detailed study on the solar EUV effects. The individual contributions of chemical heating and inclusion of excess photodissociative heating were quantified in relation to an overall neutral heating efficiency. Heating rates of chemical and photodissociation heating during different parts of the solar cycle were presented.

Venus thermosphere models may use more parameters in the energy equation than those addressed here. There are many more that are more pertinent to the momentum and mass continuity equations, as well as the ionosphere itself. This work is meant to shed light into the scale of the uncertainty involved with using such parameters in the modeling community, but is also specific to V-GITM. While other models must use similar parameterizations, the implementation may not necessarily be the same, and therefore, the effect on the results may be different. However, the goal of this work is to provide some knowledge of the relative importance of each of these parameters, and while the results from each model may be different, the effects due to each of the parameters presented should be quite similar.

Venus thermosphere models may use more parameters in the energy equation than those addressed here. Additional parameters may be more significant in the context of the continuity, momentum and all ion equations. While other models may employ similar energy sources, the implementation may differ resulting in varied outcomes. Nonetheless, this work provides insight into the relative significance of each parameter and emphasizes that models yielding different results are driven by the uncertainty parameterizations.

5.5 Future Work

In the future, V-GITM will look to enhance the EUV processes by adding more species to the heating from photodissociation of other species (O_2, N_2, CO, NO). Aside from dissociation, excess energy from ionizing photons and photoelectron heating may also contribute but are not accounted for currently. Due to the uniqueness of V-GITM, determining the specific impact of the non-hydrostatic solver is an important question to solve. Another difference is the coupling of ion dynamics with the photochemically generated ionosphere. For this reason, model-model comparisons should be performed to determine if (a) the hydrostatic assumption is limiting the existing

Venus GCMs and (b) the consequence of have a dynamical ionosphere.

5.6 Open Research

V-GITM is freely available through GitHub (Ridley et al., 2023). Plotting routines and data within this work will be published on DeepBlue.

Acknowledgements

The research presented in this study was supported at University of Michigan partially by the joint NSF-NASA Space Weather with Quantified Uncertainties program under NSF grant number 2028125 and NASA grant number 80NSSC20K1581. This work was also supported by the NASA grant 80NSSC19K0562.

CHAPTER 6

Conclusion and Future Work

6.1 Conclusion

This dissertation focused on heat balance through the Earth and Venus thermosphere. The heat balance distinctly determines the temperature, wind and density structure. GITM and V-GITM were used to simulate the coupled ionosphere-thermosphere system and several in-situ datasets were used to validate our findings. The foundation was set for why the development of GCMs and better understanding the physics systematically dependent on one another. Chapters 3-5 attempted to answer the science questions posed in the Chapter 1.

- **Outstanding question:** What are the uncertain thermodynamic source terms?
  Finding: There are uncertainties in essentially every source term. In Chapter 3, it was shown how a variety of thermal conductivity coefficients could be used depending on the literature source. Often times the basis for recommended coefficients are measured in a laboratory at temperatures and pressures inconsistent with those applicable to thermospheres. Chapter 5 varied four more source terms indicating alternative methods or parameter coefficients for each term. Methods for the deposition of solar EUV were completely exchanged from a commonly used direct heating method to that of chemical and photodissociation heating. Near IR parameterizations were modified and differences at the terminators were emphasized.

- **Outstanding question:** How do uncertainties in the thermodynamics change the global and regional temperature structure?
  Finding: In Chapter 3, the uncertainty in thermal conductivity coefficients and exponents were shown to have up to a 50-100% affect on neutral mass densities. Although used tangentially, an EUV driven input, F10.7, affected the mass densities similarly. In Chapter 5, the impact of a heating efficiency to drive solar EUV heating was shown to have dramatic changes in the globally averaged temperatures. At the top of the model, globally averaged temperatures changed by nearly 50 K when changing from the use of chemical heating to a

commonly used heating efficiency value. In regards to the solar IR, the leading parameterizations from other models were re-parameterized showing significant temperature changes at the terminators. Unexpectedly so, changes to the to the lower atmosphere NLTE CO_2 cooling had significant changes to the global temperature profile.

- **Outstanding question:** How do the uncertainties influence other terms like composition, density and neutral velocities?
  Finding: Studies on the eddy diffusion coefficient were shown to affect homopause locations leading to large species-specific changes in number density. Additionally, changes in the eddy diffusion coefficient affected the overall viscosity profiles which are important for the neutral wind structure. It was emphasized in Chapter 4 and Chapter 5 that temperatures, winds and densities are all coupled together. This means that each uncertain term affecting temperatures will inevitably influence wind speeds and bulk densities. Narrowing the model uncertainties is helpful for establishing more concrete answers to some of the other existing science questions.

- **Outstanding question:** Due to the slow planetary rotation, how is a nightside ionosphere sustained at Venus? Does solving for the winds explicitly change day-night structure? What is the impact of a non-zero, lower boundary condition for the zonal winds? What controls the temperature as a function of altitude? Does advection drive any of this?
  Finding: Although Venus' maintains a nightside ionosphere, the composition and mechanism for sustaining it are largely unknown. To address this, the 3D model, V-GITM was developed in Chapter 4. It was found that a combination of advection of O_2^+ and chemistry allowed for the accumulation of NO^+ on the nightside. We do not expect this to be the lone ion, but it has been interesting to find that the ions, when advected, and neutrals move together allowing for transport to the nightside due to the high wind speeds. It is expected that similar mechanisms to that of Earth that ions may precipitate from high altitudes to bulk the ionosphere and add diversity to the composition.

6.2 Future Work

Presented here are questions that need to be still addressed and ideas regarding possible improvements of GITM and V-GITM to better represent the Earth and Venus states:

- Chapter 3 studied the implementation of RCMR to estimate the thermal conductivity coefficient based on satellite and empirical datasets. Future work is necessary with the goal of

investigating the ability of thermal conductivity to improve mass density and temperature states at new locations. Work has not yet been performed to determine how the terminators, nightside or lower atmosphere respond to heat conductivity changes.

- In the second study, V-GITM was introduced as a model. With any new model, it will not be perfect and so continuously improving the model is necessary. This is especially true due to the uniqueness of V-GITM when compared to the existing Venus GCMs. Future work should be done in the development of the ion dynamics paying particular attention to the nightside ionosphere. This includes adding advection of more ions (O^+, NO^+, etc...). Additionally, it is expected, but still unclear if there is plasma precipitation on the nightside and if it is important or could even be captured in V-GITM's limited vertical domain. Given this, new nightside boundary conditions to simulate precipitation can be added. If deemed important, the domain could be expanded to self-consistently model the physics.

- As V-GITM's ionosphere density and dynamics are improved, it would be important to complete the set of equations by solving for the ion and electron energy equations. Currently, the ion temperature is assumed to be equal to the neutral temperature. This reasonable temporary approximation, but should be self-consistently solved in the future with magnetohydrodynamic models. Ion temperatures drive changes in many of the other GITM state variables: ion velocities and neutral temperatures to only mention two. Chemistry also relies heavily on the ion and electron temperatures to correctly compute reaction rates meaning that ion and electron temperatures are intimately coupled with the neutral population. While implementing all of the magnetohydrodynamics may be outside of the scope of V-GITM, parameterizations of the ion and electron temperatures could be a simpler, but more accurate representation of these states.

- V-GITM's neutral composition at noon and midnight were shown in Chapter 4. It was pointed out that N-based molecules were not always accurate to observations or other researcher findings. It was not expected that these had a major impact on the bulk temperature, winds and number density, but as V-GITM is used for more science such as the exploration of NO nightglow, then the N-based densities need to be corrected. NO and O_2 nightglow are important tracers for thermospheric circulation. To do so, NO_x chemistry should be addressed in great detail with modern reaction rates and ion/electron temperatures should be better captured. Uncertainty in the overall Venus heat budget also adds to the importance of ensuring that these densities are correct due to the unknown impact of incorrect densities on the overall contribution to chemical heating. For this reason, the chemistry should be re-investigated with a focus on N(^4S), N(^2D) and NO.

- In Chapter 5, the energy contribution of excess photodissociation for CO_2 was added to V-GITM. This mechanism is not unique to CO_2 and should be completed for other neutrals undergoing photolysis, such as O_2, N_2, and CO. This source term is not included in the Earth, Mars or Titan versions of GITM and should be implemented as deemed necessary.

Given the many recommendations for improvements to V-GITM, this model could have a role in the upcoming missions to Venus. The new model and its improvements may be helpful in making predictions for aerobraking maneuvers and data analysis activities pre-launch. With the addition of new measurements, V-GITM is also a useful tool to evaluate the accuracy of space weather forecasting as a whole which may uncover new upper atmosphere physics. These types of studies are impactful because they improve our understanding of Venus, but also drive the new research ongoing for terrestrial-like exoplanet upper atmospheres.

Appendix A

Chemistry Reaction Rates

The reaction rate for some chemical equations from Table 4.3:

(R11) $N(^4S) + O \rightarrow NO$

$$1.9 \times 10^{-23} \sqrt{\frac{300}{T_n}} (1 - \frac{0.57}{\sqrt{T_n}})$$

(R21) $N_2^+ + O \rightarrow NO^+ + N(^2D)$

$$1.33 \times 10^{-16} (300/T_i)^{0.44}$$

(R27) $N_2^+ + e \rightarrow 2N(^2D)$

$$1.01 \times 10^{-13} (300/T_e)^{0.39}$$

BIBLIOGRAPHY

Arridge, C. (2020). Solar wind: Interaction with planets.

Banks, P. M. and Kockarts, G. (1973). *Aeronomy*. Academic Press.

Bannister, R. N. (2001). A guide to computing orbital positions of major solar system bodies: forward and inverse calculations. *Data Assimilation Research Center, University of Reading, U.K*, pages 19–23.

Barlier, F., Berger, C., Falin, J., Kockarts, G., and Thuillier, G. (1969). Aeronomica acta. *Inst. Aéronomie Spatiale, Bruxelles*.

Barnes, R. (2017). Tidal locking of habitable exoplanets. *Celest Mech Dyn Astr*, 129:509–536.

Bell, J. M., Bougher, S. W., Waite, J. Hunter, J., Ridley, A. J., Magee, B. A., Mandt, K. E., Westlake, J., DeJong, A. D., Bar-Nun, A., Jacovi, R., Toth, G., De La Haye, V., Gell, D., and Fletcher, G. (2011). Simulating the one-dimensional structure of Titan's upper atmosphere: 3. Mechanisms determining methane escape. *Journal of Geophysical Research (Planets)*, 116(E11):E11002.

Bell, J. M., Bougher, S. W., Waite Jr., J. H., Ridley, A. J., Magee, B. A., Mandt, K. E., Westlake, J., DeJong, A. D., Bar–Nun, A., Jacovi, R., Toth, G., and De La Haye, V. (2010). Simulating the one-dimensional structure of titan's upper atmosphere: 1. formulation of the titan global ionosphere-thermosphere model and benchmark simulations. *Journal of Geophysical Research: Planets*, 115(E12).

Bertaux, J.-L., Nevejans, D., Korablev, O., Villard, E., Quémerais, E., Neefs, E., Montmessin, F., Leblanc, F., Dubois, J., Dimarellis, E., Hauchecorne, A., Lefèvre, F., Rannou, P., Chaufray, J., Cabane, M., Cernogora, G., Souchon, G., Semelin, F., Reberac, A., Van Ransbeek, E., Berkenbosch, S., Clairquin, R., Muller, C., Forget, F., Hourdin, F., Talagrand, O., Rodin, A., Fedorova, A., Stepanov, A., Vinogradov, I., Kiselev, A., Kalinnikov, Y., Durry, G., Sandel, B., Stern, A., and Gérard, J. (2007). Spicav on venus express: Three spectrometers to study the global structure and composition of the venus atmosphere. *Planetary and Space Science*, 55(12):1673–1700. The Planet Venus and the Venus Express Mission, Part 2.

Bougher, S., Dickinson, R., Ridley, E., and Roble, R. (1988). Venus mesosphere and thermosphere: Iii. three-dimensional general circulation with coupled dynamics and composition. *Icarus*, 73(3):545 – 573.

Bougher, S., Dickinson, R., Ridley, E., Roble, R., Nagy, A., and Cravens, T. (1986). Venus mesosphere and thermosphere: Ii. global circulation, temperature, and density variations. *Icarus*, 68(2):284–312.

Bougher, S. W., Benna, M., Elrod, M., Roeten, K., and Thiemann, E. (2023). Maven/ngims dayside exospheric temperatures over solar cycle and seasons: Role of dayside thermal balances in regulating temperatures. *Journal of Geophysical Research: Planets*, 128(1):e2022JE007475. e2022JE007475 2022JE007475.

Bougher, S. W., Blelly, P.-L., Combi, M., Fox, J. L., Mueller-Wodarg, I., Ridley, A. J., and Roble, R. G. (2008). Neutral upper atmosphere and ionosphere modeling. *Space Sci Rev*, 139(63):107–141.

Bougher, S. W., Engel, S., Roble, R. G., and Foster, B. (1999). Comparative terrestrial planet thermospheres: 2. solar cycle variation of global structure and winds at equinox. *Journal of Geophysical Research: Planets*, 104(E7):16591–16611.

Bougher, S. W., Hunten, D. M., and Roble, R. G. (1994). Co2 cooling in terrestrial planet thermospheres. *Journal of Geophysical Research: Planets*, 99(E7):14609–14622.

Bougher, S. W., Parkinson, C. D., Brecht, A. S., Schulte, R., Fischer, J., Mahieux, A., Wilquet, V., and Vandaele, A. (2015a). Upper atmosphere temperature structure at the venusian terminators: A comparison of soir and vtgcm results. *Planetary and Space Science*, 113-114:336–346.

Bougher, S. W., Pawlowski, D., Bell, J. M., Nelli, S., McDunn, T., Murphy, J. R., Chizek, M., and Ridley, A. (2015b). Mars global ionosphere-thermosphere model: Solar cycle, seasonal, and diurnal variations of the mars upper atmosphere. *Journal of Geophysical Research: Planets*, 120(2):311–342.

Bougher, S. W., Roeten, K. J., Olsen, K., Mahaffy, P. R., Benna, M., Elrod, M., Jain, S. K., Schneider, N. M., Deighan, J., Thiemann, E., Eparvier, F. G., Stiepen, A., and Jakosky, B. M. (2017). The structure and variability of mars dayside thermosphere from maven ngims and iuvs measurements: Seasonal and solar activity trends in scale heights and temperatures. *Journal of Geophysical Research: Space Physics*, 122(1):1296–1313.

Bowman, B., Tobiska, W., and Marcos, F. (2006). A new empirical thermospheric density model jb2006 using new solar indices. In *AIAA/AAS Astrodynamics Specialist Conference and Exhibit*, page 6166.

Bowman, B., Tobiska, W. K., Marcos, F., Huang, C., Lin, C., and Burke, W. (2008). *A New Empirical Thermospheric Density Model JB2008 Using New Solar and Geomagnetic Indices*.

Bowman, B. R. (2004). The semiannual thermospheric density variation from 1970 to 2002 between 200-1100 km. *Advances in the Astronautical Sciences*, 119:04–174.

Brandt, D. A., Bussy-Virat, C. D., and Ridley, A. J. (2020). A simple method for correcting empirical model densities during geomagnetic storms using satellite orbit data. *Space Weather*, 18(12):e2020SW002565. e2020SW002565 10.1029/2020SW002565.

Brecht, A., Bougher, S., Gérard, J.-C., and Soret, L. (2012). Atomic oxygen distributions in the venus thermosphere: Comparisons between venus express observations and global model simulations. *Icarus*, 217(2):759–766. Advances in Venus Science.

Brecht, A. S., Bougher, S. W., Gérard, J. C., Parkinson, C. D., Rafkin, S., and Foster, B. (2011). Understanding the variability of nightside temperatures, no uv and o2 ir nightglow emissions in the venus upper atmosphere. *Journal of Geophysical Research: Planets*, 116(E8).

Brecht, S. H. and Ledvina, S. A. (2021). An explanation of the nightside ionospheric structure of venus. *Journal of Geophysical Research: Space Physics*, 126(2):e2020JA027779. e2020JA027779 2020JA027779.

Bruinsma, S., Tamagnan, D., and Biancale, R. (2004). Atmospheric densities derived from CHAMP/STAR accelerometer observations. *Planetary and Space Science*, 52:297–312.

Burrell, A., Goel, A., Ridley, A., and Bernstein, D. (2015). Correction of the photoelectron heating efficiency within the global ionosphere-thermosphere model using retrospective cost model refinement. *Journal of Atmospheric and Solar-Terrestrial Physics*, 124.

Bussy-Virat, C. D., Ridley, A. J., and Getchius, J. W. (2018). Effects of uncertainties in the atmospheric density on the probability of collision between space objects. *Space Weather*, 16(5):519–537.

Chamberlin, P. C., Woods, T. N., and Eparvier, F. G. (2008). Flare irradiance spectral model (fism): Flare component algorithms and results. *Space Weather*, 6(5).

Clancy, R. T., Wolff, M. J., Whitney, B. A., Cantor, B. A., Smith, M. D., and McConnochie, T. H. (2010). Extension of atmospheric dust loading to high altitudes during the 2001 mars dust storm: Mgs tes limb observations. *Icarus*, 207(1):98–109.

Coddington, O., Lean, J., Pilewskie, P., Snow, M., Richard, E., Kopp, G., Lindholm, C., DeLand, M., Marchenko, S., Haberreiter, M., and Baranyi, T. (2019). Solar irradiance variability: Comparisons of models and measurements. *Earth and Space Science*, 6(12):2525–2555.

Colegrove, F. D., Johnson, F. S., and Hanson, W. B. (1966). Atmospheric composition in the lower thermosphere. *Journal of Geophysical Research (1896-1977)*, 71(9):2227–2236.

Council, N. R. (2008). *Severe Space Weather Events: Understanding Societal and Economic Impacts: A Workshop Report*. The National Academies Press, Washington, DC.

Courant, R., Friedrichs, K., and Lewy, H. (1928). On the partial difference equations of mathematical physics. *Mathematical Annals*, 100:32–74.

Cravens, T., Brace, L., Taylor, H., Russell, C., Knudsen, W., Miller, K., Barnes, A., Mihalov, J., Scarf, F., Quenon, S., and Nagy, A. (1982). Disappearing ionospheres on the nightside of venus. *Icarus*, 51(2):271–282.

Crisp, D. (1986). Radiative forcing of the venus mesosphere: I. solar fluxes and heating rates. *Icarus*, 67(3):484–514.

DeVries, P. L. and Wolf, R. P. (1994). A first course in computational physics. *Computers in Physics*, 8(2):178–179.

Dickinson, R. E. (1976). Venus mesosphere and thermosphere temperature structure: I. global mean radiative and conductive equilibrium. *Icarus*, 27(4):479–493.

Dickinson, R. E. and Ridley, E. (1977). Venus mesosphere and thermosphere temperature structure: Ii. day-night variations. *Icarus*, 30(1):163–178.

Dickinson, R. E., Ridley, E. C., and Roble, R. G. (1984). Thermospheric general circulation with coupled dynamics and composition. *Journal of Atmospheric Sciences*, 41:205–219.

Dietrich, N., Matsuo, T., and Hsu, C.-T. (2022). Specifying satellite drag through coupled thermosphere-ionosphere data assimilation of radio occultation electron density profiles. *Space Weather*, 20(8):e2022SW003147. e2022SW003147 2022SW003147.

Doornbos, E., Klinkrad, H., and Visser, P. (2008). Use of two-line element data for thermosphere neutral density model calibration. *Advances in Space Research*, 41(7):1115–1122.

Drob, D. P., Emmert, J. T., Meriwether, J. W., Makela, J. J., Doornbos, E., Conde, M., Hernandez, G., Noto, J., Zawdie, K. A., McDonald, S. E., Huba, J. D., and Klenzing, J. H. (2015). An update to the horizontal wind model (hwm): The quiet time thermosphere. *Earth and Space Science*, 2(7):301–319.

D'Amato, A. M., Ali, A. A., Ridley, A., and Bernstein, D. S. (2013). Retrospective cost optimization for adaptive state estimation, input estimation, and model refinement. *Procedia Computer Science*, 18:1919–1928. 2013 International Conference on Computational Science.

Ehrenreich, D. and Désert, J.-M. (2011). Mass-loss rates for transiting exoplanets. *A&A*, 529:A136.

Eparvier, F. G., Chamberlin, P. C., Woods, T. N., and Thiemann, E. M. B. (2015). The solar extreme ultraviolet monitor for maven. *Space Science Reviews*, 195(1-4):293–301.

Fillingim, M., Peticolas, L., Lillis, R., Brain, D., Halekas, J., Lummerzheim, D., and Bougher, S. (2010). Localized ionization patches in the nighttime ionosphere of mars and their electrodynamic consequences. *Icarus*, 206(1):112–119. Solar Wind Interactions with Mars.

Fojas, J. J. R. and De Leon, R. L. (2013). Carotid artery modeling using the navier-stokes equations for an incompressible, newtonian and axisymmetric flow. *APCBEE Procedia*, 7:86–92. The 3rd International Conference on Biomedical Engineering and Technology - ICBET 2013.

Fox, J. (1988). Heating efficiencies in the thermosphere of venus reconsidered. *Planetary and Space Science*, 36(1):37–46.

Fox, J. L. (1985). The O_2^+ vibrational distribution in the Venusian ionosphere. *Advances in Space Research*, 5(9):165–169.

Fox, J. L. (1993). The production and escape of nitrogen atoms on mars. *Journal of Geophysical Research: Planets*, 98(E2):3297–3310.

Fox, J. L. and Bougher, S. W. (1991). Structure, luminosity, and dynamics of the venus thermosphere. *Space Sci Rev*, 55:357–489.

Fox, J. L. and Sung, K. Y. (2001). Solar activity variations of the venus thermosphere/ionosphere. *Journal of Geophysical Research: Space Physics*, 106(A10):21305–21335.

Fromang, Sébastien, Leconte, Jeremy, and Heng, Kevin (2016). Shear-driven instabilities and shocks in the atmospheres of hot jupiters. *A&A*, 591:A144.

Fuller-Rowell, T. J. and Rees, D. (1980). A three-dimensional, time-dependent, global model of the thermosphere. *Journal of the Atmospheric Sciences*, 37.

Garcia, M. (2021). Space debris and human spacecraft.

Garvin, J. B., Getty, S. A., Arney, G. N., Johnson, N. M., Kohler, E., Schwer, K. O., Sekerak, M., Bartels, A., Saylor, R. S., Elliott, V. E., Goodloe, C. S., Garrison, M. B., Cottini, V., Izenberg, N., Lorenz, R., Malespin, C. A., Ravine, M., Webster, C. R., Atkinson, D. H., Aslam, S., Atreya, S., Bos, B. J., Brinckerhoff, W. B., Campbell, B., Crisp, D., Filiberto, J. R., Forget, F., Gilmore, M., Gorius, N., Grinspoon, D., Hofmann, A. E., Kane, S. R., Kiefer, W., Lebonnois, S., Mahaffy, P. R., Pavlov, A., Trainer, M., Zahnle, K. J., and Zolotov, M. (2022). Revealing the mysteries of venus: The DAVINCI mission. *The Planetary Science Journal*, 3(5):117.

Gilli, G., Lebonnois, S., González-Galindo, F., López-Valverde, M., Stolzenbach, A., Lefèvre, F., Chaufray, J., and Lott, F. (2017). Thermal structure of the upper atmosphere of venus simulated by a ground-to-thermosphere gcm. *Icarus*, 281:55–72.

Gilli, G., López-Valverde, M., Peralta, J., Bougher, S., Brecht, A., Drossart, P., and Piccioni, G. (2015). Carbon monoxide and temperature in the upper atmosphere of venus from virtis/venus express non-lte limb measurements. *Icarus*, 248:478–498.

Gilli, G., Navarro, T., Lebonnois, S., Quirino, D., Silva, V., Stolzenbach, A., Lefèvre, F., and Schubert, G. (2021). Venus upper atmosphere revealed by a gcm: Ii. model validation with temperature and density measurements. *Icarus*, 366:114432.

Goel, A., Ponder, B. M., Ridley, A. J., and Bernstein, D. S. (2020). Estimation of thermal-conductivity coefficients in the global ionosphere–thermosphere model. *Journal of Aerospace Information Systems*, 17(9):546–553.

Goel, A., Ridley, A. J., and Bernstein, D. S. (2018). Estimation of the eddy diffusion coefficient using total electron content data. *2018 Annual American Control Conference (ACC)*.

González-Galindo, F., Chaufray, J.-Y., López-Valverde, M. A., Gilli, G., Forget, F., Leblanc, F., Modolo, R., Hess, S., and Yagi, M. (2013). Three-dimensional martian ionosphere model: I. the photochemical ionosphere below 180 km. *Journal of Geophysical Research: Planets*, 118(10):2105–2123.

Gringauz, K. I., Verigin, M. I., Breus, T. K., and Gombosi, T. (1979). The interaction of electrons in the optical umbra of venus with the planetary atmosphere—the origin of the nighttime ionosphere. *Journal of Geophysical Research: Space Physics*, 84(A5):2123–2127.

Gu, H., Cui, J., Niu, D.-D., Cao, Y.-T., Wu, X.-S., Li, J., Wu, Z.-P., He, F., and Wei, Y. (2020). Neutral heating efficiency in the dayside martian upper atmosphere. *The Astronomical Journal*, 159(2):39.

Guinan, E. F. and Ribas, I. (2002). Our Changing Sun: The Role of Solar Nuclear Evolution and Magnetic Activity on Earth's Atmosphere and Climate. In Montesinos, B., Gimenez, A., and Guinan, E. F., editors, *The Evolving Sun and its Influence on Planetary Environments*, volume 269 of *Astronomical Society of the Pacific Conference Series*, page 85.

Hanley, K. G., Fowler, C. M., McFadden, J. P., Mitchell, D. L., and Curry, S. (2022). Maven-static observations of ion temperature and initial ion acceleration in the martian ionosphere. *Geophysical Research Letters*, 49(18):e2022GL100182. e2022GL100182 2022GL100182.

Harman, C. (2017). Circumstellar habitable zone — Wikipedia, the free encyclopedia. [Online; accessed 12-November-2022].

Haus, R., Kappel, D., and Arnold, G. (2015). Radiative heating and cooling in the middle and lower atmosphere of venus and responses to atmospheric and spectroscopic parameter variations. *Planetary and Space Science*, 117:262–294.

Heays, A. N., Bosman, A. D., and van Dishoeck, E. F. (2017). Photodissociation and photoionisation of atoms and molecules of astrophysical interest. *A&A*, 602:A105.

Hedin, A. E. (1983). A revised thermospheric model based on mass spectrometer and incoherent scatter data: Msis-83. *Journal of Geophysical Research: Space Physics*, 88.

Hedin, A. E. (1987). Msis-86 thermospheric model. *Journal of Geophysical Research: Space Physics*, 92(A5):4649–4662.

Hedin, A. E. (1991). Extension of the msis thermosphere model into the middle and lower atmosphere. *Journal of Geophysical Research: Space Physics*, 96(A2):1159–1172.

Hedin, A. E., Niemann, H. B., Kasprzak, W. T., and Seiff, A. (1983). Global empirical model of the venus thermosphere. *Journal of Geophysical Research: Space Physics*, 88(A1):73–83.

Hejduk, M. D. and Frigm, R. K. (2015). Collision avoidance short course - part i: Theory.

Hejduk, M. D. and Snow, D. E. (2018). The effect of neutral density estimation errors on satellite conjunction serious event rates. *Space Weather*, 16(7):849–869.

Hensley, K., Withers, P., Girazian, Z., Pätzold, M., Tellmann, S., and Häusler, B. (2020). Dependence of dayside electron densities at venus on solar irradiance. *Journal of Geophysical Research: Space Physics*, 125(2):e2019JA027167. e2019JA027167 10.1029/2019JA027167.

Hilsenrath, J. e. a. (1960). Tables of thermodynamic and transport properties. *Pergamon Press*.

Hollenbach, D., Prasad, S., and Whitten, R. (1985). The thermal structure of the dayside upper atmosphere of venus above 125 km. *Icarus*, 64(2):205–220.

Hoshino, N., Fujiwara, H., Takagi, M., and Kasaba, Y. (2013). Effects of gravity waves on the day-night difference of the general circulation in the venusian lower thermosphere. *Journal of Geophysical Research: Planets*, 118(10):2004–2015.

Hoshino, N., Fujiwara, H., Takagi, M., Takahashi, Y., and Kasaba, Y. (2012). Characteristics of planetary-scale waves simulated by a new venusian mesosphere and thermosphere general circulation model. *Icarus*, 217(2):818–830. Advances in Venus Science.

Huber, M. L., Sykioti, E. A., Assael, M. J., and Perkins, R. A. (2016). Reference correlation of the thermal conductivity of carbon dioxide from the triple point to 1100 k and up to 200 mpa. *Journal of Physical and Chemical Reference Data*, 45(1):013102.

Huestis, D. L., Bougher, S. W., Fox, J. L., Galand, M., Johnson, R. E., I., M. J., and Pickering, J. C. (2008). Cross sections and reaction rates for comparative planetary aeronomy. *Space Sci Rev*, 139(63).

Häusler, B., Pätzold, M., Tyler, G., Simpson, R., Bird, M., Dehant, V., Barriot, J.-P., Eidel, W., Mattei, R., Remus, S., Selle, J., Tellmann, S., and Imamura, T. (2006). Radio science investigations by vera onboard the venus express spacecraft. *Planetary and Space Science*, 54(13):1315–1335. The Planet Venus and the Venus Express Mission.

Jacchia, L. G. (1970). New Static Models of the Thermosphere and Exosphere with Empirical Temperature Profiles. *SAO Special Report*, 313.

Jain, S. K., Bougher, S. W., Deighan, J., Schneider, N. M., González Galindo, F., Stewart, A. I. F., Sharrar, R., Kass, D., Murphy, J., and Pawlowski, D. (2020). Martian thermospheric warming associated with the planet encircling dust event of 2018. *Geophysical Research Letters*, 47(3):e2019GL085302. e2019GL085302 10.1029/2019GL085302.

Jakosky, B., Brain, D., Chaffin, M., Curry, S., Deighan, J., Grebowsky, J., Halekas, J., Leblanc, F., Lillis, R., Luhmann, J., Andersson, L., Andre, N., Andrews, D., Baird, D., Baker, D., Bell, J., Benna, M., Bhattacharyya, D., Bougher, S., Bowers, C., Chamberlin, P., Chaufray, J.-Y., Clarke, J., Collinson, G., Combi, M., Connerney, J., Connour, K., Correira, J., Crabb, K., Crary, F., Cravens, T., Crismani, M., Delory, G., Dewey, R., DiBraccio, G., Dong, C., Dong, Y., Dunn, P., Egan, H., Elrod, M., England, S., Eparvier, F., Ergun, R., Eriksson, A., Esman, T., Espley, J., Evans, S., Fallows, K., Fang, X., Fillingim, M., Flynn, C., Fogle, A., Fowler, C., Fox, J., Fujimoto, M., Garnier, P., Girazian, Z., Groeller, H., Gruesbeck, J., Hamil, O., Hanley, K., Hara, T., Harada, Y., Hermann, J., Holmberg, M., Holsclaw, G., Houston, S., Inui, S., Jain, S., Jolitz, R., Kotova, A., Kuroda, T., Larson, D., Lee, Y., Lee, C., Lefevre, F., Lentz, C., Lo, D., Lugo, R., Ma, Y.-J., Mahaffy, P., Marquette, M., Matsumoto, Y., Mayyasi, M., Mazelle, C., McClintock, W., McFadden, J., Medvedev, A., Mendillo, M., Meziane, K., Milby, Z., Mitchell, D., Modolo, R., Montmessin, F., Nagy, A., Nakagawa, H., Narvaez, C., Olsen, K., Pawlowski, D., Peterson, W., Rahmati, A., Roeten, K., Romanelli, N., Ruhunusiri, S., Russell, C., Sakai, S., Schneider, N., Seki, K., Sharrar, R., Shaver, S., Siskind, D., Slipski, M., Soobiah, Y., Steckiewicz, M., Stevens, M., Stewart, I., Stiepen, A., Stone, S., Tenishev, V., Terada, N., Terada, K., Thiemann, E., Tolson, R., Toth, G., Trovato, J., Vogt, M., Weber, T., Withers, P., Xu, S., Yelle, R., Yiğit, E., and Zurek, R. (2018). Loss of the martian atmosphere to space: Present-day loss rates determined from maven observations and integrated loss through time. *Icarus*, 315:146–157.

Jones Jr., M., Sutton, E. K., Emmert, J. T., Siskind, D. E., and Drob, D. P. (2021). On the effects of mesospheric and lower thermospheric oxygen chemistry on the thermosphere and ionosphere semiannual oscillation. *Journal of Geophysical Research: Space Physics*, 126(3):e2020JA028647. e2020JA028647 2020JA028647.

Kalafatoglu Eyiguler, E. C., Shim, J. S., Kuznetsova, M. M., Kaymaz, Z., Bowman, B. R., Codrescu, M. V., Solomon, S. C., Fuller-Rowell, T. J., Ridley, A. J., Mehta, P. M., and Sutton, E. K. (2019). Quantifying the storm time thermospheric neutral density variations using model and observations. *Space Weather*, 17(2):269–284.

Kalman, R. E. (1960). A New Approach to Linear Filtering and Prediction Problems. *Journal of Basic Engineering*, 82(1):35–45.

Kasting, J. F. (1988). Runaway and moist greenhouse atmospheres and the evolution of earth and venus. *Icarus*, 74(3):472–494.

Keating, G., Bertaux, J., Bougher, S., Dickinson, R., Cravens, T., Nagy, A., Hedin, A., Krasnopolsky, V., Nicholson, J., Paxton, L., and von Zahn, U. (1985). Models of venus neutral upper atmosphere: Structure and composition. *Advances in Space Research*, 5(11):117–171.

Keating, G. M., Tolson, R. H., and Hinson, E. W. (1979). Venus thermosphere and exosphere: First satellite drag measurements of an extraterrestrial atmosphere. *Science*, 203(4382):772–774.

Kliore, A., Moroz, V., and Keating, G. (1985). *The Venus International Reference Atmosphere.*, volume 5.

Kliore, A. J., Luhmann, J. G., and Zhang, M. H. G. (1991). The effect of the solar cycle on the maintenance of the nightside ionosphere of venus. *Journal of Geophysical Research: Space Physics*, 96(A7):11065–11071.

Kliore, A. J., Patel, I. R., Nagy, A. F., Cravens, T. E., and Gombosi, T. I. (1979). Initial observations of the nightside ionosphere of venus from pioneer venus orbiter radio occultations. *Science*, 205(4401):99–102.

Knudsen, W. C. (1987). Frequency functions of venus nightside ion densities. *Journal of Geophysical Research: Space Physics*, 92(A7):7308–7316.

Knudsen, W. C. (1992). *The Venus Ionosphere from in Situ Measurements*, pages 237–263. American Geophysical Union (AGU).

Kockarts, G. and Peetermans, W. (1970). Atomic oxygen infrared emission in the earth's upper atmosphere. *Planetary and Space Science*, 18(2):271–285.

Korablev, O., Bertaux, J. L., Nevejans, D., and Team, S. I. (2003). Compact High-Resolution IR Spectrometer for Atmospheric Studies. *EAEJA*, page 14785.

Krehbiel, J. P., Brace, L. H., Theis, R. F., Cutler, J. R., Pinkus, W. H., and Kaplan, R. B. (1980). Pioneer venus orbiter electron temperature probe. *IEEE Transactions on Geoscience and Remote Sensing*, GE-18(1):49–54.

Kuang, D., Desai, S., Sibthorpe, A., and Pi, X. (2014). Measuring atmospheric density using gps-leo tracking data. *Advances in Space Research*, (53):243–256.

Lambert, J. and Edwards, A. (2019). Energy: The driver of climate. [Online; accessed 12-November-2022].

Lide, D. R., E.-i. C. (1997). Crc handbook of chemistry and physics. *Boca Raton, FL: CRC Press*.

Lillis, R. J., Brain, D. A., Bougher, S. W., Leblanc, F., Luhmann, J. G., Jakosky, B. M., Modolo, R., Fox, J., Deighan, J., Fang, X., Wang, Y. C., Lee, Y., Dong, C., Ma, Y., Cravens, T., Andersson, L., Curry, S. M., Schneider, N., Combi, M., Stewart, I., Clarke, J., Grebowsky, J., Mitchell, D. L., Yelle, R., Nagy, A. F., Baker, D., and Lin, R. P. (2015). Characterizing Atmospheric Escape from Mars Today and Through Time, with MAVEN. *Space Science Reviews*, 195(1-4):357–422.

Limaye, S. S., Lebonnois, S., Mahieux, A., Pätzold, M., Bougher, S., Bruinsma, S., Chamberlain, S., Clancy, R. T., Gérard, J.-C., Gilli, G., Grassi, D., Haus, R., Herrmann, M., Imamura, T., Kohler, E., Krause, P., Migliorini, A., Montmessin, F., Pere, C., Persson, M., Piccialli, A., Rengel, M., Rodin, A., Sandor, B., Sornig, M., Svedhem, H., Tellmann, S., Tanga, P., Vandaele, A. C., Widemann, T., Wilson, C. F., Müller-Wodarg, I., and Zasova, L. (2017). The thermal structure of the venus atmosphere: Intercomparison of venus express and ground based observations of vertical temperature and density profiles. *Icarus*, 294:124–155.

Liu, H.-L., Bardeen, C. G., Foster, B. T., Lauritzen, P., Liu, J., Lu, G., Marsh, D. R., Maute, A., McInerney, J. M., Pedatella, N. M., Qian, L., Richmond, A. D., Roble, R. G., Solomon, S. C., Vitt, F. M., and Wang, W. (2018). Development and validation of the whole atmosphere community climate model with thermosphere and ionosphere extension (waccm-x 2.0). *Journal of Advances in Modeling Earth Systems*, 10(2):381–402.

Luhmann, J. G. (1986). The Solar Wind Interaction with Venus. , 44(3-4):241–306.

López-Valverde, M. A., Edwards, D. P., López-Puertas, M., and Roldán, C. (1998). Non-local thermodynamic equilibrium in general circulation models of the martian atmosphere 1. effects of the local thermodynamic equilibrium approximation on thermal cooling and solar heating. *Journal of Geophysical Research: Planets*, 103(E7):16799–16811.

Machado, P., Luz, D., Widemann, T., Lellouch, E., and Witasse, O. (2012). Mapping zonal winds at venus's cloud tops from ground-based doppler velocimetry. *Icarus*, 221(1):248–261.

Machado, P., Widemann, T., Peralta, J., Gonçalves, R., Donati, J.-F., and Luz, D. (2017). Venus cloud-tracked and doppler velocimetry winds from cfht/espadons and venus express/virtis in april 2014. *Icarus*, 285:8–26.

Mahieux, A., Berkenbosch, S., Clairquin, R., Fussen, D., Mateshvili, N., Neefs, E., Nevejans, D., Ristic, B., Vandaele, A. C., Wilquet, V., Belyaev, D., Fedorova, A., Korablev, O., Villard, E., Montmessin, F., and Bertaux, J.-L. (2008). In-flight performance and calibration of spicav soir onboard venus express. *Applied Optics*, 47(13):2252 – 2265. Cited by: 48.

Mahieux, A., Yelle, R., Yoshida, N., Robert, S., Piccialli, A., Nakagawa, H., Kasaba, Y., Mills, F., and Vandaele, A. (2021). Determination of the venus eddy diffusion profile from co and co2 profiles using soir/venus express observations. *Icarus*, 361:114388.

Malhotra, G. and Ridley, A. (2020). Impacts of Spatially Varying Eddy Diffusion Coefficient in the Lower Thermosphere on the Ionosphere and Thermosphere using GITM. In *AGU Fall Meeting Abstracts*, volume 2020, pages SA001–0014.

Malhotra, G., Ridley, A. J., Marsh, D. R., Wu, C., and Paxton, L. J. (2017). Understanding the Effects of Lower Boundary Conditions and Eddy Diffusion on the Ionosphere-Thermosphere System. In *AGU Fall Meeting Abstracts*, volume 2017, pages SA33A–2593.

Marcos, F. A. (1990). Accuracy of atmospheric drag models at low satellite altitudes. *Advances in Space Research*, 10(3-4):417–422.

Martinez, A., Brecht, A. S., Karyu, H., Lebonnois, S., Bougher, S. W., Kuroda, T., Kasaba, Y., Gilli, G., Navarro, T., and Sagawa, H. (2021). Venusian Upper Mesosphere and Lower Thermosphere GCMs Intercomparison Project. In *LPI Contributions*, volume 2628 of *LPI Contributions*, page 8045.

Martinez, A., Lebonnois, S., Millour, E., Pierron, T., Moisan, E., Gilli, G., and Lefèvre, F. (2023). Exploring the variability of the venusian thermosphere with the ipsl venus gcm. *Icarus*, 389:115272.

Masutti, D., March, G., Ridley, A. J., and Thoemel, J. (2016). Effect of the solar activity variation on the global ionosphere thermosphere model (gitm). *Annales Geophysicae*, 34(9):725–736.

Matsuo, T. and Hsu, C.-T. (2021). *Inference of Hidden States by Coupled Thermosphere-Ionosphere Data Assimilation*, chapter 18, pages 343–363. American Geophysical Union (AGU).

Matsuo, T., Lee, I.-T., and Anderson, J. L. (2013). Thermospheric mass density specification using an ensemble kalman filter. *Journal of Geophysical Research: Space Physics*, 118(3):1339–1350.

Moorthy, A. K., Blandino, J. J., Demetriou, M. A., and Gatsonis, N. A. (2021). Extended lifetime of cubesats in the lower thermosphere with active attitude control. *Journal of Spacecraft and Rockets*, 58(6):1876–1892.

Moroz, V. and Zasova, L. (1997). Vira-2: A review of inputs for updating the venus international reference atmosphere. *Advances in Space Research*, 19(8):1191–1201. Planetary Atmospheres and Ionospheres and Reference Atmospheres.

Morozov, A., Ali, A., D'Amato, A., Ridley, A., Kukreja, S., and Bernstein, D. (2011). Retrospective-cost-based model refinement for system emulation and subsystem identification. *Proceedings of the IEEE Conference on Decision and Control*, pages 2142–2147.

Morselli, A., Armellin, R., Di Lizia, P., and Bernelli-Zazzera, F. (2012). Computing collision probability using differential algebra and advanced monte carlo methods. volume 3.

Navarro, T., Gilli, G., Schubert, G., Lebonnois, S., Lefèvre, F., and Quirino, D. (2021). Venus' upper atmosphere revealed by a gcm: I. structure and variability of the circulation. *Icarus*, 366:114400.

Pachura, D. and Hejduk, M. D. (2016). Conjunction assessment late-notice high-interest event investigation: Space weather aspects. *NASA Technical Reports Server*.

Pang, K. and Hord, C. W. (1973). Mariner 9 ultraviolet spectrometeer experiment: 1971 mars' dust storm. *Icarus*, 18(3):481–488.

Parkinson, C., Bougher, S., Mills, F., Yung, Y., Brecht, A., Shields, D., and Liemohn, M. (2021). Modeling of observations of the oh nightglow in the venusian mesosphere. *Icarus*, 368:114580.

Pavlov, A. V. (2017). Thermal conductivity of the multicomponent neutral atmosphere. *Journal of Geophysical Research: Space Physics*, 122(12):12,476–12,485.

Pawlowski, D. J. and Ridley, A. J. (2009). The effect of the characteristics of solar flares on the thermospheric response. *AGU Fall Meeting Abstracts*, pages SA51A–1213.

Peralta, J., Lee, Y. J., Hueso, R., Clancy, R. T., Sandor, B. J., Sánchez-Lavega, A., Lellouch, E., Rengel, M., Machado, P., Omino, M., Piccialli, A., Imamura, T., Horinouchi, T., Murakami, S., Ogohara, K., Luz, D., and Peach, D. (2017). Venus's winds and temperatures during the messenger's flyby: An approximation to a three-dimensional instantaneous state of the atmosphere. *Geophysical Research Letters*, 44(8):3907–3915.

Petrignani, A., van der Zande, W. J., Cosby, P. C., Hellberg, F., Thomas, R. D., and Larsson, M. (2005). Vibrationally resolved rate coefficients and branching fractions in the dissociative recombination of O2+. *Journal of Chemical Physics*, 122(1):014302–014302.

Philpott, L. C., Johnson, C. L., Winslow, R. M., Anderson, B. J., Korth, H., Purucker, M. E., and Solomon, S. C. (2014). Constraints on the secular variation of Mercury's magnetic field from the combined analysis of MESSENGER and Mariner 10 data. , 41(19):6627–6634.

Picone, J. M., Hedin, A. E., Drob, D. P., and Aikin, A. C. (2002). Nrlmsise-00 empirical model of the atmosphere: Statistical comparisons and scientific issues. *Journal of Geophysical Research: Space Physics*, 107(A12):SIA 15–1–SIA 15–16.

Pilinski, M. D. and Crowley, G. (2015). Seasonal variability in global eddy diffusion and the effect on neutral density. *Journal of Geophysical Research: Space Physics*, 120(4):3097–3117.

Poling, B. E., Prausnitz, J. M., and O'Connell, J. P. (2001). *Properties of Gases and Liquids*. New York: McGraw-Hill Education, 5 edition.

Ponder, B. M., Ridley, A. J., Goel, A., and Bernstein, D. S. (2023). Improving forecasting ability of gitm using data-driven model refinement. *Space Weather*, 21(3):e2022SW003290. e2022SW003290 2022SW003290.

Qian, L., Solomon, S. C., and Kane, T. J. (2009). Seasonal variation of thermospheric density and composition. *Journal of Geophysical Research: Space Physics*, 114(A1).

Reid, R., Prausnitz, J., and Sherwood, T. K. (1977). The properties of gases and liquids. *New York: McGraw-Hill Book Co.*

Rengel, M., Hartogh, P., and Jarchow, C. (2008). Hhsmt observations of the venusian mesospheric temperature, winds, and co abundance around the messenger flyby. *Planetary and Space Science*, 56(13):1688–1695. Advances in Planetary Sciences: AOGS 2007.

Richards, P. G. (2022). Ionospheric photoelectrons: A lateral thinking approach. *Frontiers in Astronomy and Space Sciences*, 9.

Richards, P. G., Fennelly, J. A., and Torr, D. G. (1994). Euvac: A solar euv flux model for aeronomic calculations. *Journal of Geophysical Research: Space Physics*, 99(A5):8981–8992.

Richards, P. G., Woods, T. N., and Peterson, W. K. (2006). Heuvac: A new high resolution solar euv proxy model. *Advances in Space Research*, 37(2):315–322. Thermospheric-Ionospheric-Geospheric(TIGER)Symposium.

Richmond, A. D., Ridley, E. C., and Roble, R. (1992). A thermosphere/ionosphere general circulation model with coupled electrodynamics. *Geophys. Res. Lett.*, 19.

Ridley, A., spacecataz, Meng, X., Öztürk, D. C. S., Ponder, B., and Burleigh, M. (2023). Gitm-code/gitm: v23.01.06.

Ridley, A. J., Deng, Y., and Tóth, G. (2006). The global ionosphere-thermosphere model. *Journal of Atmospheric and Solar-Terrestrial Physics*, 68:839–864.

Roble, R. G., Ridley, E. C., and Dickinson, R. E. (1987). On the global mean structure of the thermosphere. *Journal of Geophysical Research: Space Physics*, 92(A8):8745–8758.

Roeten, K. J., Bougher, S. W., Benna, M., Mahaffy, P. R., Lee, Y., Pawlowski, D., González-Galindo, F., and López-Valverde, M. (2019). Maven/ngims thermospheric neutral wind observations: Interpretation using the m-gitm general circulation model. *Journal of Geophysical Research: Planets*, 124(12):3283–3303.

Roldán, C., López-Valverde, M., López-Puertas, M., and Edwards, D. (2000). Non-lte infrared emissions of co2 in the atmosphere of venus. *Icarus*, 147(1):11–25.

Rosati, R. E., Johnsen, R., and Golde, M. F. (2003). Absolute yields of CO($a'\,^3\Sigma^+$, $d\,^3\Delta_i$,$e\,^3\Sigma^-$)+O from the dissociative recombination of $CO_2{}^+$ ions with electrons. , 119(22):11630–11635.

Saleh, J. H., Hastings, D. E., and Newman, D. J. (2004). Weaving time into system architecture: satellite cost per operational day and optimal design lifetime. *Acta Astronautica*, 54(6):413 – 431.

Santillo, M. A. and Bernstein, D. S. (2010). Adaptive control based on retrospective cost optimization. *Journal of Guidance, Control, and Dynamics*, 33(2):289–304.

Schubert, G., Bougher, S. W., Covey, C. C., Del Genio, A. D., Grossman, A. S., Hollingsworth, J. L., Limaye, S. S., and Young, R. E. (2007). *Venus Atmosphere Dynamics: A Continuing Enigma*, pages 101–120. American Geophysical Union (AGU).

Schubert, G., Covey, C., Genio, A. D., Elson, L. S., Keating, G., Seiff, A., Young, R. E., Apt, J., Counselman III, C. C., Kliore, A. J., Limaye, S. S., Revercomb, H. E., Sromovsky, L. A., Suomi, V. E., Taylor, F., Woo, R., and von Zahn, U. (1980). Structure and circulation of the venus atmosphere. *Journal of Geophysical Research: Space Physics*, 85(A13):8007–8025.

Schunk, R. W. and Nagy, A. F. (2004). *Ionospheres*. Cambridge University Press.

Shaw, D. A., Holland, D. M. P., Hayes, M. A., MacDonald, M. A., Hopkirk, A., and McSweeney, S. M. (1995). A study of the absolute photoabsorption, photoionisation and photodissociation cross sections and the photoionisation quantum efficiency of carbon dioxide from the ionisation threshold to 345 Å. *Chemical Physics*, 198(3):381–396.

Slavin, J. A., Krimigis, S. M., Acuña, M. H., Anderson, B. J., Baker, D. N., Koehn, P. L., Korth, H., Livi, S., Mauk, B. H., Solomon, S. C., and Zurbuchen, T. H. (2007). MESSENGER: Exploring Mercury's Magnetosphere. , 131(1-4):133–160.

Smith III, F. L. and Smith, C. (1972). Numerical evaluation of chapman's grazing incidence integral ch (x,). *Journal of Geophysical Research (1896-1977)*, 77(19):3592–3597.

Spenner, K., Knudsen, W. C., Whitten, R. C., Michelson, P. F., Miller, K. L., and Novak, V. (1981). On the maintenance of the venus nightside ionosphere: Electron precipitation and plasma transport. *Journal of Geophysical Research: Space Physics*, 86(A11):9170–9178.

Spreiter, J. R., Summers, A. L., and Rizzi, A. W. (1970). Solar wind flow past nonmagnetic planets—venus and mars. *Planetary and Space Science*, 18(9):1281–1299.

Stam, J. (2003). Real-time fluid dynamics for games.

Stolzenbach, A., Lefèvre, F., Lebonnois, S., and Määttänen, A. (2023). Three-dimensional modeling of venus photochemistry and clouds. *Icarus*, 395:115447.

Storz, M. F., Bowman, B. R., Branson, M. J. I., Casali, S. J., and Tobiska, W. K. (2005). High accuracy satellite drag model (hasdm). *Advances in Space Research*, 36(12):2497 – 2505. Space Weather.

Sutton, E. K. (2018). A new method of physics-based data assimilation for the quiet and disturbed thermosphere. *Space Weather*, 16(6):736–753.

Taylor, F. and Grinspoon, D. (2009). Climate evolution of Venus. *Journal of Geophysical Research (Planets)*, 114(E11):E00B40.

Taylor, F.W., Svedhem, H., and Head, J. W. (2018). Venus: The atmosphere, climate, surface, interior and near-space environment of an earth-like planet. *Space Science Reviews*, 214.

Taylor Jr., H. A., Brinton, H. C., Bauer, S. J., Hartle, R. E., Cloutier, P. A., and Daniell Jr., R. E. (1980). Global observations of the composition and dynamics of the ionosphere of venus: Implications for the solar wind interaction. *Journal of Geophysical Research: Space Physics*, 85(A13):7765–7777.

Teran, J. (2018). Movie animation: A continuum for frictional contact. *Notices of the American Mathematical Society*, 65:1.

Thayer, J. P., Tobiska, W. K., Pilinski, M. D., and Sutton, E. K. (2021). *Remaining Issues in Upper Atmosphere Satellite Drag*, chapter 5, pages 111–140. American Geophysical Union (AGU).

Theis, R. F. and Brace, L. H. (1993). Solar cycle variations of electron density and temperature in the venusian nightside ionosphere. *Geophysical Research Letters*, 20(23):2719–2722.

Theis, R. F., Brace, L. H., Elphic, R. C., and Mayr, H. G. (1984). New empirical models of the electron temperature and density in the venus ionosphere with application to transterminator flow. *Journal of Geophysical Research: Space Physics*, 89(A3):1477–1488.

Thiemann, E. M. B., Chamberlin, P. C., Eparvier, F. G., Templeman, B., Woods, T. N., Bougher, S. W., and Jakosky, B. M. (2017). The maven euvm model of solar spectral irradiance variability at mars: Algorithms and results. *Journal of Geophysical Research: Space Physics*, 122(3):2748–2767.

Torr, M. R., Torr, D. G., and Richards, P. G. (1980). The solar ultraviolet heating efficiency of the midlatitude thermosphere. , 7(5):373–376.

Vargaftik, N. B., Filippov, L. P., Tarzimanov, A. A., and Totskii, E. E. (1993). *Handbook of Thermal Conductivity of Liquids and Gases*. CRC Press.

von Zahn, U., Fricke, K. H., Hunten, D. M., Krankowsky, D., Mauersberger, K., and Nier, A. O. (1980). The upper atmosphere of venus during morning conditions. *Journal of Geophysical Research: Space Physics*, 85(A13):7829–7840.

Wang, X., Miao, J., Lu, X., Aa, E., Luo, B., Liu, J., Hong, Y., Wang, Y., Ren, T., Zeng, R., Du, C., and Liu, S. (2022). Using temporal relationship of thermospheric density with geomagnetic activity indices and joule heating as calibration for nrlmsise-00 during geomagnetic storms. *Space Weather*, 20(4):e2021SW003017. e2021SW003017 2021SW003017.

Widemann, T., Ghail, R., Wilson, C. F., and Titov, D. V. (2020). EnVision: Europe's Proposed Mission to Venus. In *AGU Fall Meeting Abstracts*, volume 2020, pages P022–02.

Woods, T. N., Eparvier, F. G., Bailey, S. M., Chamberlin, P. C., Lean, J., Rottman, G. J., Solomon, S. C., Tobiska, W. K., and Woodraska, D. L. (2005). Solar euv experiment (see): Mission overview and first results. *Journal of Geophysical Research: Space Physics*, 110(A1).

Woods, T. N., Harder, J. W., Kopp, G., and Snow, M. (2022). Solar-cycle variability results from the solar radiation and climate experiment (sorce) mission. *Solar Physics*, 297(43).

Zhu, J. and Ridley, A. J. (2016). Investigating the performance of simplified neutral-ion collisional heating rate in a global it model. *Journal of Geophysical Research: Space Physics*, 121(1):578–588.

Zhu, Z., Stone, J. M., and Rafikov, R. R. (2013). Low-mass planets in protoplanetary disks with net vertical magnetic fields: The planetary wake and gap opening. *The Astrophysical Journal*, 768(2):143.